Physics of the Dark Universe 27 (2020) 100371

Contents lists available at ScienceDirect

Physics of the Dark Universe

journal homepage: www.elsevier.com/locate/dark

Dark Matter benchmark models for early LHC Run-2 Searches: Report of the ATLAS/CMS Dark Matter Forum

Daniel Abercrombie [1], Nural Akchurin [2], Ece Akilli [3], Juan Alcaraz Maestre [4], Brandon Allen [1], Barbara Alvarez Gonzalez [5,a], Jeremy Andrea [17], Alexandre Arbey [6,7], Georges Azuelos [8], Patrizia Azzi [9], Mihailo Backović [52], Yang Bai [10], Swagato Banerjee [10,b], James Beacham [11,c], Alexander Belyaev [12], Antonio Boveia [11,*,d,e], Amelia Jean Brennan [13], Oliver Buchmueller [14], Matthew R. Buckley [15], Giorgio Busoni [16,f], Michael Buttignol [17], Giacomo Cacciapaglia [25], Regina Caputo [18], Linda Carpenter [11], Nuno Filipe Castro [19], Guillelmo Gomez Ceballos [1], Yangyang Cheng [20,g], John Paul Chou [21], Arely Cortes Gonzalez [22,h], Chris Cowden [2], Francesco D'Eramo [23,i], Annapaola De Cosa [24], Michele De Gruttola [5], Albert De Roeck [5], Andrea De Simone [16], Aldo Deandrea [25], Zeynep Demiragli [1,j], Anthony DiFranzo [26,k], Caterina Doglioni [27,d], Tristan du Pree [5,l], Robin Erbacher [28], Johannes Erdmann [29], Cora Fischer [22], Henning Flaecher [30], Patrick J. Fox [31], Benjamin Fuks [32,m], Marie-Helene Genest [33], Bhawna Gomber [10,n], Andreas Goudelis [34,m], Johanna Gramling [35,o], John Gunion [28], Kristian Hahn [36], Ulrich Haisch [37,p], Roni Harnik [38], Philip C. Harris [5,q], Kerstin Hoepfner [46], Siew Yan Hoh [39], Dylan George Hsu [1], Shih-Chieh Hsu [89], Yutaro Iiyama [1], Valerio Ippolito [40,r], Thomas Jacques [41,s], Xiangyang Ju [10,t], Felix Kahlhoefer [42,u], Alexis Kalogeropoulos [42,v], Laser Seymour Kaplan [10], Lashkar Kashif [10], Valentin V. Khoze [43], Raman Khurana [44,w], Khristian Kotov [11,x], Dmytro Kovalskyi [1], Suchita Kulkarni [45,y], Shuichi Kunori [2,z],

* Corresponding author.
E-mail address: boveia.1@osu.edu (A. Boveia).
a Now at Oviedo U.
b Now at Louisville U.
c Now at Duke U.
d Forum organizer and editor.
e Previously at CERN
f Now at Heidelberg U., Max Planck Inst.
g Now at Cornell U.
h Now at CERN.
i Now at INFN Padua.
j Now at Boston U.
k Now at Rutgers U.
l Now at NIKHEF.
m Now at Paris LPTHE.
n Now at Hyderabad U.
o Now at UC Irvine.
p Now at Munich MPI.
q Now at MIT.
r Now at INFN Rome.
s Now at SISSA Trieste.
t Now at LBL.
u Now at RWTH Aachen.
v Now at Princeton U.
w Now at Delhi U.
x Now at Florida U.
y Editor.
z Now at Maryland U.

https://doi.org/10.1016/j.dark.2019.100371

Viktor Kutzner [46], Hyun Min Lee [47], Sung-Won Lee [2], Seng Pei Liew [48], Tongyan Lin [49,aa], Steven Lowette [50,d], Romain Madar [51], Sarah Malik [14,d], Fabio Maltoni [52], Mario Martinez Perez [22], Olivier Mattelaer [53,ab], Kentarou Mawatari [54,ac], Christopher McCabe [55,ad], Théo Megy [56,ae], Enrico Morgante [41,af], Stephen Mrenna [57,d], Chang-Seong Moon [58,ag], Siddharth M. Narayanan [1], Andy Nelson [59], Sérgio F. Novaes [60], Klaas Ole Padeken [61,ah], Priscilla Pani [62,y,af], Michele Papucci [63], Manfred Paulini [64], Christoph Paus [1], Jacopo Pazzini [96], Björn Penning [14,ai], Michael E. Peskin [65], Deborah Pinna [24,j], Massimiliano Procura [66], Shamona F. Qazi [67], Davide Racco [41,aj], Emanuele Re [68,ak], Antonio Riotto [41], Thomas G. Rizzo [69], Rainer Roehrig [70], David Salek [71,y], Arturo Sanchez Pineda [72,h], Subir Sarkar [73,74], Alexander Schmidt [75,al], Steven Randolph Schramm [3], William Shepherd [76,77,am], Gurpreet Singh [78], Livia Soffi [79], Norraphat Srimanobhas [80], Kevin Sung [81,q], Tim M.P. Tait [82], Timothee Theveneaux-Pelzer [83,af], Marc Thomas [84], Mia Tosi [85], Daniele Trocino [86,an], Sonaina Undleeb [2], Alessandro Vichi [7,ao], Fuquan Wang [10], Lian-Tao Wang [87], Ren-Jie Wang [88,ap], Nikola Whallon [89], Steven Worm [90,aq], Mengqing Wu [91,ar], Sau Lan Wu [10], Hongtao Yang [10], Yong Yang [92,as], Shin-Shan Yu [93], Bryan Zaldivar [94,at], Marco Zanetti [96], Zhiqing Zhang [95], Alberto Zucchetta [96,au]

[1] *MIT, USA*
[2] *Texas Tech University, USA*
[3] *Université de Genève, DPNC, Switzerland*
[4] *Centro de Investigaciones Energéticas Medioambientales y Tecnológicas (CIEMAT), Spain*
[5] *CERN, Switzerland*
[6] *Université de Lyon and Centre de Recherche Astrophysique de Lyon, CNRS and Ecole Normale Supérieure de Lyon, France*
[7] *CERN Theory Division, Switzerland*
[8] *University of Montreal and TRIUMF, Canada*
[9] *INFN Padova, Italy*
[10] *University of Wisconsin-Madison, USA*
[11] *Ohio State University, USA*
[12] *Rutherford Appleton Laboratory and University of Southampton, United Kingdom*
[13] *The University of Melbourne, Australia*
[14] *Imperial College London, United Kingdom*
[15] *Department of Physics and Astronomy, Rutgers University, USA*
[16] *SISSA and INFN, Sezione di Trieste, Italy*
[17] *Institut Pluridisciplinaire Hubert Curien/Département Recherches Subatomiques, Université de Strasbourg/CNRS-IN2P3, France*
[18] *Santa Cruz Institute for Particle Physics, Department of Physics and Department of Astronomy and Astrophysics, University of California at Santa Cruz, USA*
[19] *LIP-Minho, Braga, and Departamento de Física e Astronomia, Faculdade de Ciências da Universidade do Porto, Portugal*
[20] *University of Chicago, USA*
[21] *Rutgers University, USA*
[22] *IFAE Barcelona, Spain*
[23] *University of California and LBNL, Berkeley, USA*
[24] *University of Zurich, Switzerland*
[25] *Université de Lyon and Université Lyon 1, CNRS/IN2P3, UMR5822, IPNL, France*
[26] *Department of Physics and Astronomy, University of California, Irvine and Theoretical Physics Department, Fermilab, USA*
[27] *Lund University, Sweden*

[aa] Now at San Diego U.
[ab] Now at Louvain CP3.
[ac] Now at Osaka U.
[ad] Now at King's College London.
[ae] Now at Freiburg U.
[af] Now at DESY.
[ag] Now at Kyungpook Natl. U.
[ah] Now at Vanderbilt U.
[ai] Now at Brandeis U.
[aj] Now at Perimeter.
[ak] Now Annecy LAPTH.
[al] Now at RWTH Aachen U.
[am] Now at Mainz U.
[an] Now at U. Gent.
[ao] Now at LPHE Lausanne.
[ap] Now at Mainz.
[aq] Now at Birmingham U.
[ar] Now at Beijing IHEP.
[as] Now at Shanghai Jiao Tong U.
[at] Now at LAPTh.
[au] Now at Zurich. U.

[28] University of California, Davis, USA
[29] Institut für Experimentelle Physik IV, Technische Universität Dortmund, Germany
[30] H.H. Wills Physics Laboratory, University of Bristol, United Kingdom
[31] Fermilab, USA
[32] Institut Pluridisciplinaire Hubert Curien/Département Recherches Subatomiques, Université de Strasbourg/CNRS-IN2P3, France
[33] LPSC, UniversitÈ Grenoble-Alpes, CNRS/IN2P3, France
[34] Institut für Hochenergiephysik, Österreichische Akademie der Wissenschaften, Austria
[35] Université de Genève, DPNC, Switzerland
[36] Northwestern University, USA
[37] Rudolf Peierls Centre for Theoretical Physics, University of Oxford, United Kingdom
[38] Theoretical Physics Department, Fermilab, USA
[39] National Centre for Particle Physics, Universiti Malaya, Malaysia
[40] Laboratory for Particle Physics and Cosmology, Harvard University, USA
[41] Department of Theoretical Physics, University of Geneva, Switzerland
[42] Deutsches Elektronen-Synchrotron (DESY), Germany
[43] Institute of Particle Physics Phenomenology, Durham University, United Kingdom
[44] National Central University, Taiwan
[45] Institut für Hochenergiephysik, Österreichische Akademie der Wissenschaften, Austria
[46] RWTH Aachen University, III. Physikalisches Institut A, Germany
[47] Department of Physics, Chung-Ang University, Korea
[48] Department of Physics, University of Tokyo, Japan
[49] Kavli Institute for Cosmological Physics, University of Chicago, USA
[50] Vrije Universiteit Brussel - IIHE, Belgium
[51] Laboratoire de Physique Corpusculaire, Clermont-Ferrand, France
[52] Centre for Cosmology, Particle Physics and Phenomenology (CP3), Université catholique de Louvain, Belgium
[53] IPPP Durham, United Kingdom
[54] Theoretische Natuurkunde and IIHE/ELEM, Vrije Universiteit Brussel, and International Solvay Institutes, Belgium
[55] GRAPPA, University of Amsterdam, Netherlands
[56] Laboratoire de Physique Corpusculaire, Clermont-Ferrand, France
[57] FNAL, USA
[58] Universidade Estadual Paulista, Brazil
[59] University of California, Irvine, USA
[60] Universidade Estadual Paulista, Brazil
[61] RWTH Aachen University, III. Physikalisches Institut A, Aachen, Germany
[62] Stockholm University, Sweden
[63] Theoretical Physics Group, Lawrence Berkeley National Laboratory, and Berkeley Center for Theoretical Physics, University of California, Berkeley, USA
[64] Carnegie Mellon University, USA
[65] SLAC, Stanford University, USA
[66] Universität Wien, Austria
[67] National Centre for Physics, Quaid-i-Azam University, Pakistan
[68] Rudolf Peierls Centre for Theoretical Physics, University of Oxford, United Kingdom
[69] SLAC, USA
[70] Max-Planck-Institut fuer Physik, Germany
[71] Nikhef and GRAPPA, Netherlands
[72] INFN Sezione di Napoli, and Dipartimento di Fisica, Università di Napoli, Italy
[73] Rudolf Peierls Centre for Theoretical Physics, University of Oxford, United Kingdom
[74] Niels Bohr Institute, Copenhagen, Denmark
[75] University of Hamburg, Germany
[76] University of California Santa Cruz Department of Physics and Santa Cruz Institute for Particle Physics, USA
[77] Niels Bohr International Academy, University of Copenhagen, Denmark
[78] Chulalongkorn University, Thailand
[79] Cornell University, USA
[80] Chulalongkorn University, Faculty of Science, Department of Physics, Thailand
[81] Northwestern University, USA
[82] Department of Physics and Astronomy, University of California, Irvine, USA
[83] Laboratoire de Physique Corpusculaire, Clermont Université and Université Blaise Pascal and CNRS/IN2P3, Clermont-Ferrand, France
[84] Southampton University, United Kingdom
[85] University of Padova and INFN, Italy
[86] Northeastern University, Boston, USA
[87] Enrico Fermi Institute and Department of Physics and Kavli Institute for Cosmological Physics, University of Chicago, USA
[88] Department of Physics, Northeastern University, USA
[89] Physics, University of Washington, Seattle, USA
[90] Particle Physics Department, Rutherford Appleton Laboratory, United Kingdom
[91] Laboratoire de Physique Subatomique et de Cosmologie, Université Grenoble-Alpes, CNRS/IN2P3, France
[92] Universität Zurich, Switzerland
[93] National Central University, Taiwan
[94] Université Libre de Bruxelles, Belgium
[95] Laboratoire de l'Accélérateur Linéaire, University Paris-Sud 11 et IN2P3/CNRS, France
[96] Università di Padova, Italy

ARTICLE INFO

ABSTRACT

This document is the final report of the ATLAS-CMS Dark Matter Forum, a forum organized by the ATLAS and CMS collaborations with the participation of experts on theories of Dark Matter, to select a minimal basis set of dark matter simplified models that should support the design of the early LHC Run-2 searches. A prioritized, compact set of benchmark models is proposed, accompanied by studies

Article history:
Received 10 July 2019
Accepted 19 August 2019

Keywords:
Dark Matter
Simplified models
EFT
LHC

of the parameter space of these models and a repository of generator implementations. This report also addresses how to apply the Effective Field Theory formalism for collider searches and present the results of such interpretations.

1. Introduction

Dark matter (DM)[1] has not yet been observed in particle physics experiments, and there is not yet any evidence for non-gravitational interactions between DM and the Standard Model (SM) particles. If such interactions exist, particles of DM could be produced at the LHC. Since DM particles themselves do not produce signals in the LHC detectors, one way to observe them is when they are produced in association with a visible SM particle X($=g, q, \gamma, Z, W$, or h). Such reactions, which are observed at colliders as particles or jets recoiling against an invisible state, are called "mono-X" or $\not{E}_T$+X reactions (see e.g Refs. [1–5]), where $\not{E}_T$ is the missing transverse momentum observable in the detector.

Early Tevatron and LHC Run-1 searches for $\not{E}_T$+X signatures at CDF [6], ATLAS [7–14] and CMS [15–21], employed a basis of contact interaction operators in effective field theories (EFTs) [22,23] to calculate the possible signals. These EFTs assume that production of DM takes place through a contact interaction involving a quark–antiquark pair, or two gluons, and two DM particles. In this case, the missing energy distribution of the signal is determined by the nature and the mass of the DM particles and the Lorentz structure of the interaction. Only the overall production rate is a free parameter to be constrained or measured. Provided that the contact interaction approximation holds, these EFTs provide a straightforward way to compare the results from different collider searches with non-collider searches for DM.

The EFT describes the case when the mediator of the interaction between SM and DM particles are very heavy; if this is not the case, models that explicitly include these mediators are needed [5,22,24,24–28]. Some "simplified models" [29–31] of DM production were constructed, including particles and interactions beyond the SM. These models can be used consistently at LHC energies, and provide an extension to the EFT approach. Many proposals for such models have emerged (see, for example Refs. [32–48]). At the LHC, the kinematics of mono-X reactions occurring via a TeV-scale mediator can differ substantially from the prediction of the contact interaction. The mediator may also produce qualitatively different signals, such as decays back into the SM particles. Thus, appropriate simplified models are an important component of the design, optimization, and interpretation of DM searches at ATLAS and CMS. This has already been recognized in the CDF, ATLAS and CMS searches quoted above, where both EFT and selected simplified model results are presented.

1.1. The ATLAS/CMS dark matter forum

To understand what signal models should be considered for the upcoming LHC Run-2, groups of experimenters from both ATLAS and CMS collaborations have held separate meetings with small groups of theorists, and discussed further at the DM@LHC workshop [39,40,49]. These discussions identified overlapping sets of simplified models as possible benchmarks for early LHC Run-2 searches. Following the DM@LHC workshop, ATLAS and CMS organized a forum, called the *ATLAS-CMS Dark Matter Forum*, to form a consensus on the use of these simplified models and EFTs for early Run-2 searches with the participation of experts on theories of DM. This is the final report of the ATLAS-CMS Dark Matter Forum.

One of the guiding principles of this report is to channel the efforts of the ATLAS and CMS collaborations towards a minimal basis of dark matter models that should influence the design of the early Run-2 searches. At the same time, a thorough survey of realistic collider signals of DM is a crucial input to the overall design of the search program.

The goal of this report is such a survey, though confined within some broad assumptions and focused on benchmarks for kinematically-distinct signals which are most urgently needed. As far as time and resources have allowed, the assumptions have been carefully motivated by theoretical consensus and comparisons of simulations. But, to achieve such a consensus in only a few months before the start of Run-2, it was important to restrict the scope and timescale to the following:

1. The forum should propose a prioritized, compact set of benchmark simplified models that should be agreed upon by both collaborations for Run-2 searches. The values for the scan on the parameters of the models for which experimental results are provided should be specified, to facilitate theory reinterpretation beyond the necessary model-independent limits that should be provided by all LHC DM searches.
2. The forum should recommend the use of the state of the art calculations for these benchmark models. Such a recommendation will aid the standardization the event generator implementation of the simplified models and the harmonization of other common technical details as far as practical for early Run-2 LHC analyses. It would be desirable to have a common choice of leading order (LO) and next-to-leading order (NLO) matrix elements corresponding to the state of the art calculations, parton shower (PS) matching and merging, factorization and renormalization scales for each of the simplified models. This will also lead to a common set of theory uncertainties, which will facilitate the comparison of results between the two collaborations.
3. The forum should discuss how to apply the EFT formalism and present the results of EFT interpretations.
4. The forum should prepare a report summarizing these items, suitable both as a reference for the internal ATLAS and CMS audiences and as an explanation of early Run-2 LHC benchmark models for theory and non-collider readers. This report represents the views of its endorsers, as participants of the forum.

This document constitutes the basis for further recommendations from the LHC Dark Matter Working Group [50–52].

[1] Many theories of physics beyond the Standard Model predict the existence of stable, neutral, weakly-interacting and massive particles that are putative DM candidates. In the following, we refer to such matter as DM, even though the observation of such matter at a collider could only establish that it is neutral, weakly-interactive, massive and stable on the distance-scales of tens of meters.

1.2. Grounding assumptions

We assume that interactions exist between the SM hadrons and the particles that constitute cosmological DM. If this is not the case, then proton collisions will not directly produce DM particles, and DM will not scatter off nuclei in direct detection experiments.

The DM itself is assumed to be a single particle, a Dirac fermion WIMP, stable on collider timescales and non-interacting with the detector. The former assumption is reductionistic. The rich particle content of the SM is circumstantial evidence that the DM sector, which constitutes five times as much of the mass of the universe, may be more complex than a single particle or a single interaction. But, as was often the case in the discoveries of the SM, here only one mediator and one search channel might play a dominant role in the opening stages of an LHC discovery. The latter assumption focuses our work on early LHC searches, where small kinematic differences between models will not matter in a discovery scenario, and with the imminent re-start of the LHC our report relies heavily on a large body of existing theoretical work which assumed Dirac fermionic DM.

Different spins of DM particles will typically give similar results. Exceptions exist: For example, the choice of Majorana fermions forbids some processes that are allowed for Dirac fermions [22]. Aside from these, adjusting the choice of Dirac or Majorana fermions or scalars will produce only minor changes in the kinematic distributions of the visible particle and is expected to have little effect on cut-and-count[2] analysis. Thus the choice of Dirac fermion DM should be sufficient as benchmarks for the upcoming Run-2 searches.

One advantage of collider experiments lies in their ability to study and possibly characterize the mediator. A discovery of an anomalous $\not{E}_T$ signature at the LHC would not uniquely imply discovery of dark matter, while at the same time e.g. discovery of an anomalous and annually-modulated signal in a direct-detection experiment would leave unanswered many questions about the nature of the interaction that could be resolved by the simultaneous discovery of a new mediator particle. Collider, direct, and indirect detection searches provide complementary ways to approach this problem [53], and it is in this spirit that much of our focus is on the mediator.

We systematically explore the basic possibilities for mediators of various possible spins and couplings. All models considered are assumed to produce a signature with pairs of DM particles. Though more varied and interesting possibilities are added to the literature almost daily, these basic building blocks account for much of the physics studied at hadron colliders in the past three decades.

We also assume that Minimal Flavor Violation (MFV) [54–57] applies to the models included in this report. This means that the flavor structure of the couplings between DM and ordinary particles follows the same structure as the SM. This choice is simple, since no additional theory of flavor is required, beyond what is already present in the SM, and it provides a mechanism to ensure that the models do not violate flavor constraints. As a consequence, spin-0 resonances must have couplings to fermions proportional to the SM Higgs couplings. Flavor-safe models can still be constructed beyond the MFV assumption, for example [58], and deserve further study. For a discussion of MFV in the context of the simplified models included in this report, see Ref. [49].

In the parameter scan for the models considered in this report, we make the assumption of a minimal decay width for the particles mediating the interaction between SM and DM. This means that only decays strictly necessary for the self-consistency of the model (e.g. to DM and to quarks) are accounted for in the definition of the mediator width. We forbid any further decays to other invisible particles of the Dark Sector that may increase the width or produce striking, visible signatures. Studies within this report show that, for cut-and-count analyses, the kinematic distributions of many models, and therefore the sensitivity of these searches, do not depend significantly on the mediator width, as long as the width remains smaller than the mass of the particle and that narrow mediators are sufficiently light.

The particle content of the models chosen as benchmarks is limited to one single kind of DM whose self-interactions are not relevant for LHC phenomenology, and to one type of SM/DM interaction at a time. These assumptions only add a limited number of new particles and new interactions to the SM. These simplified models, independently explored by different experimental analyses, can be used as starting points to build more complete theories. Even though this factorized picture does not always lead to full theories and leaves out details that are necessary for the self-consistency of single models (e.g. the mass generation for mediator particles), it is a starting point to prepare a set of distinct but complementary collider searches for DM, as it leads to benchmarks that are easily comparable across channels.

1.3. Choices of benchmarks considered in this report and parameter scans

Contact interaction operators have been outlined as basis set of theoretical building blocks representing possible types of interactions between SM and DM particles in [23]. The approach followed by LHC searches (see e.g. Refs. [7,15] for recent jet+$\not{E}_T$ Run-1 searches with the 8 TeV dataset) so far has been to simulate only a prioritized set of the possible operators with distinct kinematics for the interpretation of the constraints obtained, and provide results that may be reinterpreted in terms of the other operators. This report intends to follow this strategy, firstly focusing on simplified models that allow the exploration of scenarios where the mediating scale is not as large. In the limit of large mediator mass, the simplified models map onto the EFT operators. Secondly, this report considers specific EFT benchmarks whenever neither a simplified model completion nor other simplified models yielding similar kinematic distributions are available and implemented in one of the event generators used by both collaborations. This is the case for dimension-5 or dimension-7 operators with direct DM-electroweak boson couplings.[3] Considering these models as separate experimental benchmarks will allow to target new signal regions and help validate the contact interaction limit of new simplified models developed to complete these specific operators. Results from these EFT benchmarks should include the condition that the momentum transfer does not probe the scale of the interaction; whenever there is no model that allows a direct mapping between these two quantities, various options should be tested to ensure a given fraction of events within the range of applicability of the EFT approach. Experimental searches should in any case deliver results that are independent from the specific benchmark tested, such as fiducial cross-sections that are excluded in a given signal region.

When choosing the points to be scanned in the parameter space of the models, this report does not quantitatively consider

[2] Cut-and-count refers to an analysis that applies a certain event selection and checks the inclusive number of events which pass. This is to be contrasted with a shape analysis, which compares the distribution of events.

[3] An example of a dimension-5 operator for scalar DM is described in Appendix A. Dimension-7 operators of DM coupling to gauge bosons exist in the literature, but they require a larger particle spectrum with respect to the models studied in this report.

constraints that are external to the MET+X analyses. This is the case also for results from LHC experiments searching for mediator decays. The main reason for not doing so in this report is the difficulty of incorporating these constraints in a rigorous quantitative way within the timescale of the Forum. However, even if the parameter scans and the searches are not optimized with those constraints in mind, we intend to make all information available to the community to exploit the unique sensitivity of colliders to all possible DM signatures.

1.4. Structure of this report and dissemination of results

The report provides a brief theoretical summary of the models considered, starting from the set of simplified models and contact interactions put forward in previous discussions and in the literature cited above. Its main body documents the studies done within this Forum to identify a kinematically distinct set of model parameters to be simulated and used as benchmarks for early Run-2 searches. The implementation of these studies according to the state of the art calculations is detailed, including instructions on how to estimate theoretical uncertainties in the generators used for these studies. The presentation of results for EFT benchmarks is also covered.

Section 2 of this report is dedicated to simplified models with radiation of a hard object either from the initial state or from the mediator. These models produce primarily monojet signatures, but should be considered for all $\not{E}_T$+X searches. Section 3 contains studies on the benchmark models for final states specifically containing an electroweak boson ($W/Z/\gamma/H$). In this case, both simplified models leading to mono-boson signatures and contact interaction operators are considered. Details of the state of the art calculations and on the implementation of the simplified models in Monte Carlo generators are provided in Section 4. Section 5 is devoted to the treatment of the presentation of results for the benchmark models from contact interaction operators. Section 6 prescribes how to estimate theoretical uncertainties on the simulation of these models. Section 7 concludes the report.

Further models that could be studied beyond early searches and their implementation are described in Appendix A. For these models, either the implementation could not be fully developed by the time of this report, or some of the grounding assumptions were not fully met. Some of these models have been used in previous ATLAS and CMS analyses and discussed thoroughly within the Forum. They are therefore worth considering for further studies and for Run-2 searches, since they lead to unique $\not{E}_T$+X signatures that are not shared by any other of the models included in this report. Appendix B contains the necessary elements that should be included in the results of experimental searches to allow for further reinterpretation.

It is crucial for the success of the work of this Forum that these studies can be employed as cross-check and reference to the theoretical and experimental community interested in early Run-2 searches. For this reason, model files, parameter cards, and cross-sections for the models considered in these studies are publicly available. The Git repository of the Forum [59] contains the models and parameter files necessary to reproduce the studies within this report.

2. Simplified models for all $\not{E}_T$ +X analyses

In this Chapter we review models that yield X+$\not{E}_T$ signatures, where X is a QCD parton or γ, W, Z or h.

The primary simplified models for Dirac fermion DM studied and recommended by this Forum for early LHC Run-2 searches are detailed in this Chapter, comprising spin-0 and spin-1 mediators.

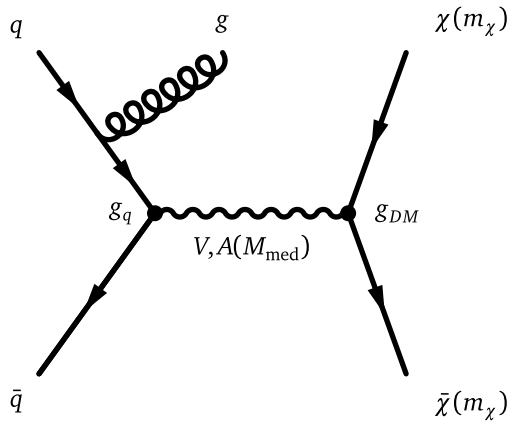

Fig. 1. Representative Feynman diagram showing the pair production of DM particles in association with a parton from the initial state via a vector or axial-vector mediator. The cross section and kinematics depend upon the mediator and DM masses, and the mediator couplings to DM and quarks respectively: (M_{med}, m_χ, g_χ, g_q).

Section 2.1 covers the s-channel exchange of a vector mediator,[4] while we consider both s-channel and t-channel exchange for scalar mediators in Sections 2.2 and 2.3 respectively. Spin-2 mediators are briefly mentioned in Section 2.4. While these models are general and cover a broad set of signatures, the discussion and studies are focused on the monojet final state. Details on final states with electroweak (EW) boson radiation and with heavy flavor quarks from diagrams arising within these models are also discussed in this Chapter.

A summary of the state of the art calculations and implementations for these models is provided in Table 9. Section 4 details the implementation of these models that have been used for the studies in this Chapter and that will be employed for the simulation of early Run-2 benchmark models for LHC DM searches.

2.1. Vector and axial vector mediator, s-channel exchange

A simple extension of the SM is an additional $U(1)$ gauge symmetry, where a DM candidate particle has charges only under this new group. Assuming that some SM particles are also charged under this group, a new gauge boson can mediate interactions between the SM and DM.

We consider the case of a DM particle χ of mass m_χ that is a Dirac fermion and where the production proceeds via the exchange of a spin-1 mediator of mass M_{med} in the s-channel, illustrated in Fig. 1.

We consider two models with vector and axial-vector couplings between the spin-1 mediator Z' and SM and DM fields, with the corresponding interaction Lagrangians:

$$\mathscr{L}_{\text{vector}} = g_q \sum_{q=u,d,s,c,b,t} Z'_\mu \bar{q}\gamma^\mu q + g_\chi Z'_\mu \bar{\chi}\gamma^\mu \chi \tag{1}$$

$$\mathscr{L}_{\text{axial-vector}} = g_q \sum_{q=u,d,s,c,b,t} Z'_\mu \bar{q}\gamma^\mu\gamma^5 q + g_\chi Z'_\mu \bar{\chi}\gamma^\mu\gamma^5 \chi\,. \tag{2}$$

The coupling g_q is assumed to be universal to all quarks. It is also possible to consider other models in which mixed vector and axial-vector couplings are considered, for instance the couplings to the quarks are axial-vector whereas those to DM are vector.

[4] Colored vector mediators can be exchanged in the t-channel, but there are no examples in literature as of this report.

As mentioned in the Introduction, when no additional visible or invisible decays contribute to the width of the mediator, the minimal width is fixed by the choices of couplings g_q and g_χ. The effect of larger widths is discussed in Section 2.5.2. For the vector and axial-vector models, the minimal width is:

$$\Gamma^{V}_{min} = \frac{g_\chi^2 M_{med}}{12\pi}\left(1+\frac{2m_\chi^2}{M_{med}^2}\right)\beta_{DM}\theta(M_{med}-2m_\chi) + \sum_q \frac{3g_q^2 M_{med}}{12\pi}\left(1+\frac{2m_q^2}{M_{med}^2}\right)\beta_q\theta(M_{med}-2m_q), \quad (3)$$

$$\Gamma^{A}_{min} = \frac{g_\chi^2 M_{med}}{12\pi}\beta_{DM}^3\theta(M_{med}-2m_\chi) + \sum_q \frac{3g_q^2 M_{med}}{12\pi}\beta_q^3\theta(M_{med}-2m_q)\,. \quad (4)$$

$\theta(x)$ denotes the Heaviside step function, and $\beta_f = \sqrt{1-\frac{4m_f^2}{M_{med}^2}}$ is the velocity of the fermion f with mass m_f in the mediator rest frame. Note the color factor 3 in the quark terms. Fig. 2 shows the minimal width as a function of mediator mass for both vector and axial-vector mediators assuming the coupling choice $g_q = g_\chi = 1$. With this choice of the couplings, the dominant contribution to the minimal width comes from the quarks, due to the combined quark number and color factor enhancement. We specifically assume that the vector mediator does not couple to leptons. If such a coupling were present, it would have a minor effect in increasing the mediator width, but it would also bring in constraints from measurements of the Drell–Yan process that would unnecessarily restrict the model space.

Therefore, the minimal set of parameters under consideration for these two models is

$$\{\, g_q,\ g_\chi,\ m_\chi,\ M_{med}\} \quad (5)$$

together with the spin structure of their couplings.

A thorough discussion of these models and their parameters can also be found in [60].

These simplified models are known and available in event generators at NLO + PS accuracy, as detailed in Section 4.1.1. Results in this Section have been obtained using the model implementation within the POWHEG generator (v3359) [61], interfaced to Pythia 8 [62] for the parton shower.

In addition, for the vector models considered, initial and final state radiation of a Z' can occur which can appear as a narrow jet if it decays hadronically and may not be distinguishable from a QCD jet, thus accounting for some fraction of the monojet signal. The ISR and FSR of Z' becomes more important at large values of the couplings [63].

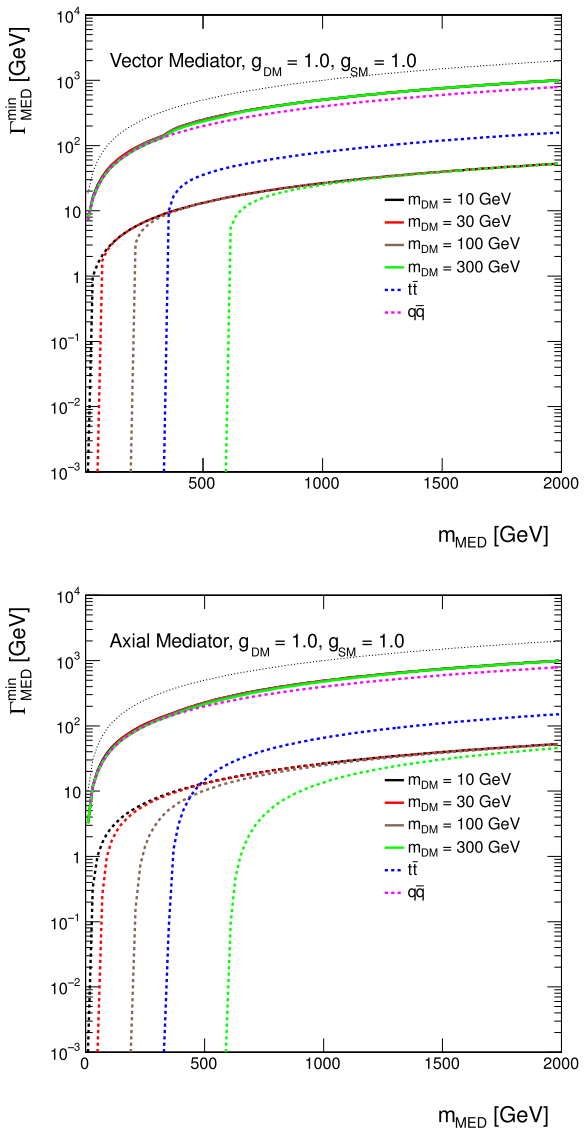

Fig. 2. Minimal width as a function of mediator mass for vector and axial-vector mediator assuming couplings of 1. The total width is shown as solid lines for DM masses of 10 GeV, 30 GeV, 100 GeV and 300 GeV in black, red, brown and green, respectively. The individual contributions from DM are indicated by dotted lines with the same colors. The contribution from all quarks but top is shown as magenta dotted line and the contribution from top quarks only is illustrated by the dotted blue line. The dotted black line shows the extreme case $\Gamma_{min} = M_{med}$. (For interpretation of the references to color in this figure legend, the reader is referred to the web version of this article.)

2.1.1. Parameter scan

In order to determine an optimal choice of the parameter grid for the simulation of early Run-2 benchmark models, dependencies of the kinematic quantities and cross sections on the model parameters have been studied. Only points that are kinematically distinct will be fully simulated, while instructions on how to rescale the results according to models with different cross sections are presented in Section 2.5. The following paragraphs list the main observations from the scans over the parameters that support the final proposal for the benchmark signal grid.

Scan over the couplings. To study the dependence of kinematic distributions on the coupling strength, samples were generated where a pair of $m_\chi = 10$ GeV DM particles is produced on-shell from the mediator of $M_{med} = 1$ TeV. Fig. 3 compares the shapes of the $\not{E}_T$ distribution for the different choices of the coupling strength. This is a generator-level prediction with no kinematic selections or detector simulation. Coupling values in the scan range 0.1–1.45, fixing $g_q = g_\chi$, correspond to a rough estimate of the lower sensitivity of mono-jet analyses and a maximum coupling value such that $\Gamma_{min} < M_{med}$. We observe that the shapes of the $\not{E}_T$ or jet p_T distributions do not depend on the couplings (and consequently the width) in the ranges considered. A large width of the mediator implies a broad integral over the contributing parton distributions, which might not be well approximated by the midpoint of this integral. This study shows that the effect, in the p_T distribution of the observed gluon, is not important.

Based on similar findings for different choices of M_{med} and m_χ, we conclude that the shapes of kinematic distributions are not altered by coupling variations, neither for the on-shell mediator

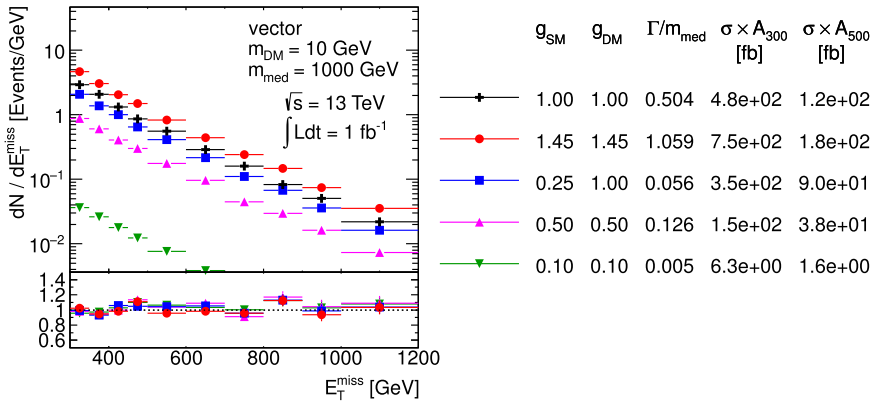

Fig. 3. Scan over couplings. The $\not{E}_T$ distribution is compared for the vector mediator models using the parameters as indicated. Ratios of the normalized distributions with respect to the first one are shown. A_{300} and A_{500} in the table denote the acceptance of the $\not{E}_T > 300$ GeV and $\not{E}_T > 500$ GeV cut, respectively. All figures in this Section have been obtained using the model implementation within the POWHEG generator (v3359) [61], interfaced to Pythia 8 [62] for the parton shower.

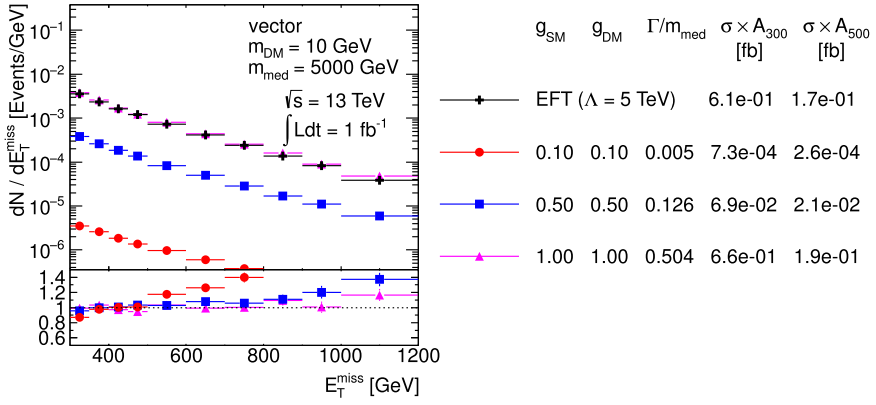

Fig. 4. Comparison of the $\not{E}_T$ distributions from the D5 EFT sample and the vector models with 5 TeV heavy mediator of various widths. Ratios of the normalized distributions with respect to the first one are shown. A_{300} and A_{500} in the table denote the acceptance of the $\not{E}_T > 300$ GeV and $\not{E}_T > 500$ GeV cut, respectively.

case where $M_{\text{med}} > 2m_\chi$, nor for the off-shell case where $M_{\text{med}} < 2m_\chi$. Only the production cross sections change. Differences in kinematic distributions are expected only close to the transition region between on-shell and off-shell mediators.

Special care needs to be taken when coupling strengths are combined with extremely heavy mediators. Fig. 4 suggests a change in the shape of the $\not{E}_T$ distribution for a $M_{\text{med}} = 5$ TeV mediator once $\Gamma_{\text{min}}/M_{\text{med}}$ is of the order of a percent or lower.

Such heavy mediators, although inaccessible with early LHC data, are interesting since they provide a good approximation for benchmark EFT models. The observed difference among the simplified models in the plot arises from the fact that the region of low invariant masses of the DM pair, $m_{\bar{\chi}\chi}$, is suppressed due to narrow Breit–Wigner peak that only probes a narrow window of parton distribution functions. For wider mediators, the low mass region is significantly enhanced by parton distribution functions at low Bjorken x, as illustrated in Fig. 5(a). This explains why the sample with the narrowest mediator in Fig. 4 is heavily suppressed in terms of production cross section and also gives different $\not{E}_T$ shape. Furthermore, Fig. 4 compares the vector model with 5 TeV mediator to the D5 EFT sample and reveals that the simplified models with larger mediator widths (e.g. for couplings of 1 where $\Gamma_{\text{min}}/M_{\text{med}} \sim 0.5$) are the ones resembling the kinematics of contact interactions. This reflects the fact that in an EFT there is no enhancement due to on-shell mediators, leading to a closer resemblance to an off-shell regime where no peak in the $m_{\bar{\chi}\chi}$ distribution is present. In case of narrow width mediators, e.g. $\Gamma_{\text{min}}/M_{\text{med}} \sim 0.05$, even larger mediator masses need to be chosen in order to significantly suppress the peak in the $m_{\bar{\chi}\chi}$ distribution and reproduce the kinematic shapes of an EFT model. Fig. 5(b) verifies that the choice of 10 TeV mediator mass is sufficient to achieve that.

Since kinematic distributions are robust to changes in the specific values of coupling,[5] the choice of $g_q = 0.25$ and $g_\chi = 1$ is reasonable to reduce the parameter space to be scanned. There are no complications associated with small couplings, but, also, the early part of Run 2 will not be sensitive to them. The range of couplings we recommend to generate limit the calculated width of the mediator to be near or below M_{med}.

For direct mediator searches, such as $q\bar{q} \to Z' \to q\bar{q}$, different couplings ($g_q \neq g_\chi$) might also be considered. A scan in g_χ vs. g_q can then be performed for a fixed mediator mass. Such searches may restrict g_q to a greater degree than g_χ.

Scan over m_χ. For a fixed mediator mass M_{med} and couplings, the DM mass falls into three regimes:

On-shell: When $M_{\text{med}} \gg 2m_\chi$, most mediators are on-shell. The hardness of the ISR is set by M_{med}, and the kinematic distributions do not strongly depend on m_χ. This is illustrated in Fig. 6 for an example of $M_{\text{med}} = 1$ TeV, 10 GeV $< m_\chi <$ 300 GeV. The cross section decreases as the m_χ approaches $M_{\text{med}}/2$. A coarse binning along m_χ is sufficient.

[5] This applies as long as heavy narrow mediators are generated without any truncation of low-mass tails at the generator-level.

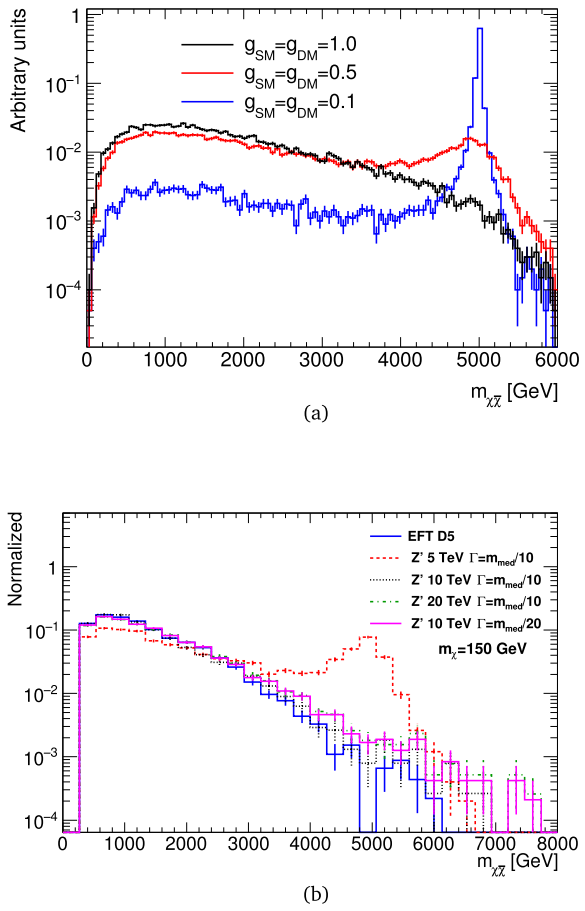

Fig. 5. Invariant mass of the DM pair in the vector mediator samples with $m_\chi = 10$ GeV, $M_{\text{med}} = 5$ TeV and different coupling strengths (a). A similar comparison is shown for the samples with different mediator masses considering $\Gamma_{\text{min}}/M_{\text{med}} = 0.05$ and 0.1 (b). An EFT sample is also displayed in the latter case. The distributions are normalized to unit area.

Threshold: When $M_{\text{med}} \approx 2m_\chi$, the production is resonantly enhanced, and both the cross section and kinematic distributions change more rapidly as a function of the two masses, and finer binning is needed in order to capture the changes.

Off-shell: When $M_{\text{med}} \ll 2m_\chi$, the DM pair is produced by an off-shell mediator. The mediator propagator gives an explicit suppression of $(M_{\text{med}}/Q)^2$ that suppresses hard ISR. The $m_\chi = 1$ TeV case, shown in Figs. 6 and 7 demonstrates that the $\not{E}_T$ spectrum hardens with increasing m_χ, accompanied by the gradual decrease of the cross section. Due to the significant cross section suppression, it is not necessary to fully populate the parameter space. Imminent LHC searches are not expected to be sensitive to these signals.

Scan over the mediator mass. Changing the mediator mass for fixed DM mass and couplings leads to significant differences in cross section and shapes of the kinematic variables for the on-shell regime, as shown in Fig. 8. As expected, higher mediator masses lead to harder $\not{E}_T$ spectra. On the other hand, the $\not{E}_T$ shapes are similar for off-shell mediators. This is illustrated in Fig. 9. Therefore, a coarse binning in M_{med} is sufficient in the off-shell regime.

Spin structure of the couplings. This section compares the kinematic properties of vector, axial-vector and mixed vector/axial-vector models. The samples with pure vector and pure axial-vector couplings are compared for $M_{\text{med}} = 100$ GeV and different DM masses in Fig. 10. No differences in the shape of the $\not{E}_T$ distributions are observed between the samples with coincident masses. In the case of the on-shell mediators, where $2m_\chi \ll M_{\text{med}}$, the cross sections of the pure vector and pure axial-vector models are similar. With increasing DM mass towards the $2m_\chi = M_{\text{med}}$ transition and further into the off-shell regime, the relative difference between the cross sections of the two samples is increasing, with the vector ones having larger cross sections.

Fig. 11 shows the samples generated with pure and mixed couplings for $m_\chi = 100$ GeV and $M_{\text{med}} = 1$ TeV, i.e. where the mediator is on-shell. The mediator width between the pure vector and pure axial-vector couplings differ only by 2% in this case, and <10% agreement between the cross sections is found. The mediator widths for the samples with the same type coupling to quarks agree at better than 1% since the width is dominated by the quark contribution, as expected from Eq. (3). No significant differences between the samples with same type DM coupling are seen, given the statistical precision of the generated samples. This is expected since the mediator is on-shell, and the details of the invisible decay are unimportant in cut-and-count searches.

For the off-shell case, shown in Fig. 12 for $m_\chi = 100$ GeV and $M_{\text{med}} = 100$ GeV, there is approximately a factor 2 difference between the cross-sections of the samples with pure couplings is observed. As in the previous case, the samples with the same type coupling to DM are similar both in terms of cross sections and $\not{E}_T$ shape. Since the contribution to the mediator width from DM is closed in this case, only the quark couplings define the width. Only couplings to light quarks are opened in the case of $M_{\text{med}} = 100$ GeV for which the differences between the partial widths of vector and axial-vector couplings are marginal. This explains the similar minimal widths for all four samples stated in Fig. 12.

In general, the coupling to quarks is not expected to play an important role in the kinematics as it is only needed to produce the mediator which is confirmed by the observations above. Based on this argument and on the observations above, we recommend to consider only the models with pure vector couplings or pure axial-vector couplings for simulation.

Proposed parameter grid. The final step in proposing a parameter grid is to evaluate the sensitivity of Run-2 LHC data with respect to rate and/or kinematics. The parameter scan focuses on two important regions, the light mediator region and the heavy mediator limit to reproduce the EFT limit, and takes into account the projected sensitivities for the mono-jet analysis.

Considering simplified models also allows to discuss constraints from different search channels. In the case of the *s*-channel exchange, the results from the mono-jet final states, where the mediator decays to a DM pair, one can also take into account dijet constraints on the processes where the mediator decays back to the SM particles. The importance of the dijet results depend on the magnitude of the coupling g_q. We recommend to keep the two channels rather independent by choosing $g_q = 0.25$ and $g_\chi = 1$, based on the findings given in Ref. [64]. Furthermore, it is also important to mention this choice leads to $\Gamma_{\text{min}}/M_{\text{med}} \lesssim 0.06$. Note that the usual choice of $g_q = g_\chi = 1$ used in literature leads to $\Gamma_{\text{min}}/M_{\text{med}} \sim 0.5$, questioning the applicability of the narrow width approximation.

The expected upper limit at 95% confidence level on the product of cross section, acceptance and efficiency, $\sigma \times A \times \epsilon$, in the final Run-1 ATLAS mono-jet analysis [7] is 51 fb and 7.2 fb for $\not{E}_T > 300$ GeV and $\not{E}_T > 500$ GeV, respectively. Projected sensitivities for a 14 TeV mono-jet analysis are available from

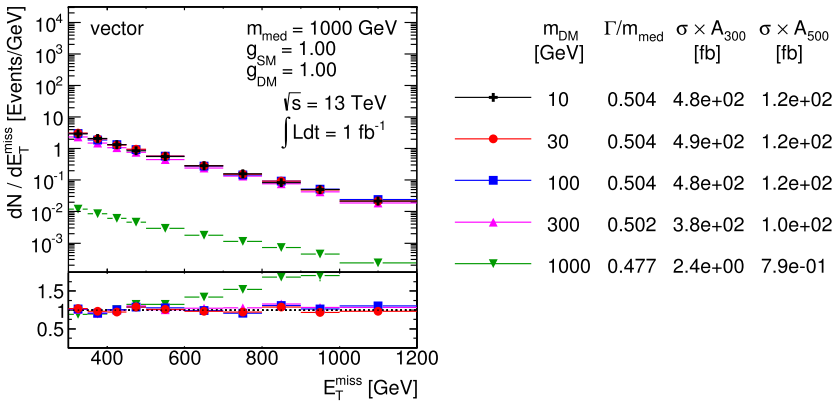

m_{DM} [GeV]	Γ/m_{med}	$\sigma \times A_{300}$ [fb]	$\sigma \times A_{500}$ [fb]
10	0.504	4.8e+02	1.2e+02
30	0.504	4.9e+02	1.2e+02
100	0.504	4.8e+02	1.2e+02
300	0.502	3.8e+02	1.0e+02
1000	0.477	2.4e+00	7.9e-01

Fig. 6. Scan over DM mass. The $\not{E}_T$ distribution is compared for the vector mediator models using the parameters as indicated. Ratios of the normalized distributions with respect to the first one are shown. A_{300} and A_{500} in the table denote the acceptance of the $\not{E}_T > 300$ GeV and $\not{E}_T > 500$ GeV cut, respectively.

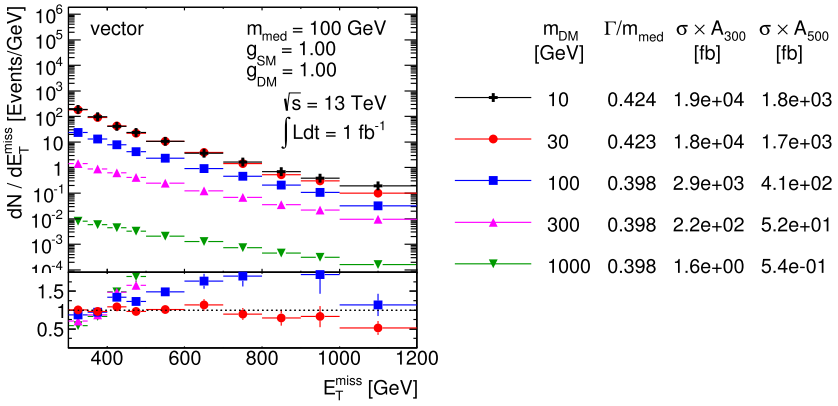

m_{DM} [GeV]	Γ/m_{med}	$\sigma \times A_{300}$ [fb]	$\sigma \times A_{500}$ [fb]
10	0.424	1.9e+04	1.8e+03
30	0.423	1.8e+04	1.7e+03
100	0.398	2.9e+03	4.1e+02
300	0.398	2.2e+02	5.2e+01
1000	0.398	1.6e+00	5.4e-01

Fig. 7. Scan over DM mass. The $\not{E}_T$ distribution is compared for the vector mediator models using the parameters as indicated. Ratios of the normalized distributions with respect to the first one are shown. A_{300} and A_{500} in the table denote the acceptance of the $\not{E}_T > 300$ GeV and $\not{E}_T > 500$ GeV cut, respectively.

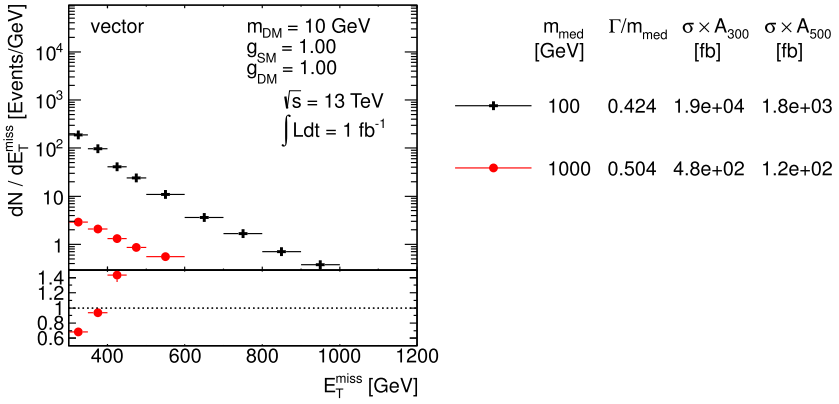

m_{med} [GeV]	Γ/m_{med}	$\sigma \times A_{300}$ [fb]	$\sigma \times A_{500}$ [fb]
100	0.424	1.9e+04	1.8e+03
1000	0.504	4.8e+02	1.2e+02

Fig. 8. Scan over mediator mass. The $\not{E}_T$ distribution is compared for the vector mediator models using the parameters as indicated. Ratios of the normalized distributions with respect to the first one are shown. A_{300} and A_{500} in the table denote the acceptance of the $\not{E}_T > 300$ GeV and $\not{E}_T > 500$ GeV cut, respectively.

ATLAS [14]. These ATLAS studies estimate a factor of two increase in sensitivity with the 2015 data. The generator level cross section times efficiency times acceptance at $\not{E}_T > 500$ GeV for the model with couplings $g_q = 0.25$ and $g_\chi = 1$, a light DM particle of $m_\chi = 10$ GeV and a $M_{med} = 1$ TeV vector mediator is at the order of 100 fb, i.e. the early Run-2 mono-jet analysis is going to be sensitive to heavier mediators than this. The value of $\sigma \times \epsilon \times A$ at $\not{E}_T > 500$ GeV for a 5 TeV vector mediator is at the order of 0.1 fb, therefore this model lies beyond the reach of the LHC in the early Run-2. However, models with high enough mediators are still useful to reproduce the EFT result.

Following these arguments, M_{med} grid points are chosen, roughly equidistant in a logarithmic scale: 10 GeV, 20 GeV, 50 GeV, 100 GeV, 200 GeV, 300 GeV, 500 GeV, 1000 GeV and 2000 GeV. In the threshold regime $M_{med} = 2m_\chi$, the m_χ grid points are taken at approximately $M_{med}/2$, namely: 10 GeV, 50 GeV, 150 GeV, 500 GeV and 1000 GeV. Points on the on-shell diagonal are always chosen to be 5 GeV away from the threshold, to avoid numerical instabilities in the event generation. The detailed studies of the impact of the parameter changes on the cross section and kinematic distributions presented earlier in this section support removing some of the grid points and relying on interpolation. The optimized grids proposed for the vector and

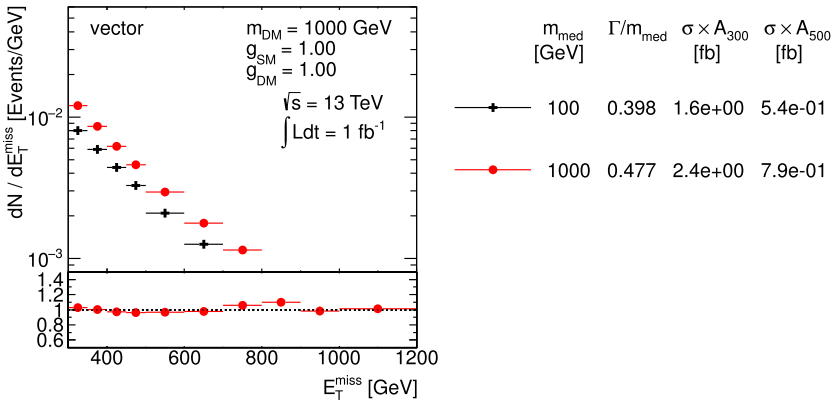

Fig. 9. Scan over mediator mass. The $\not{E}_T$ distribution is compared for the vector mediator models using the parameters as indicated. Ratios of the normalized distributions with respect to the first one are shown. A_{300} and A_{500} in the table denote the acceptance of the $\not{E}_T > 300$ GeV and $\not{E}_T > 500$ GeV cut, respectively.

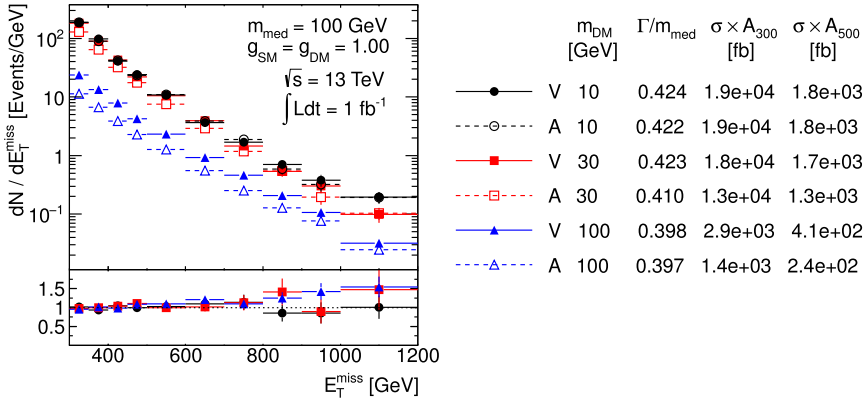

Fig. 10. Comparison of the pure vector and pure axial-vector couplings. The $\not{E}_T$ distribution is shown for the samples generated with $M_{med} = 100$ GeV and different DM masses. Ratios of the normalized distributions are shown for between the samples with coincident masses. A_{300} and A_{500} in the table denote the acceptance of the $\not{E}_T > 300$ GeV and $\not{E}_T > 500$ GeV cut, respectively.

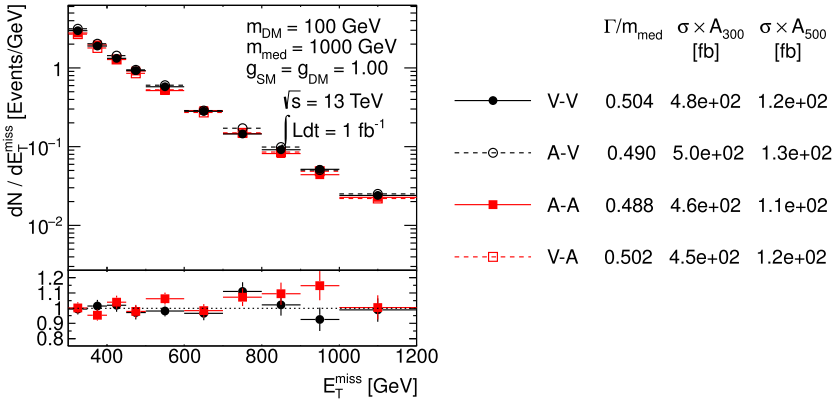

Fig. 11. Comparison of the pure vector, V-V, and pure axial-vector, A-A, couplings with mixed couplings, A-V and V-A where the first (second) letter indicates the SM (dark sector) vertex. The $\not{E}_T$ distribution is shown for the samples generated with $m_\chi = 100$ GeV and $M_{med} = 1$ TeV. Ratios of the normalized distributions are shown for A-V over V-V and for V-A over A-A. A_{300} and A_{500} in the table denote the acceptance of the $\not{E}_T > 300$ GeV and $\not{E}_T > 500$ GeV cut, respectively.

axial-vector mediators are given in Table 1. One point at very high mediator mass (10 TeV) is added for each of the DM masses scanned, to aid the reinterpretation of results in terms of contact interaction operators (EFTs), as discussed in Section 5.2.

Tables 2 and 3 give the Γ_{min}/M_{med} ratio for the parameter grid proposed for vector and axial-vector s-channel models, respectively. The numbers range from $\sim$ 0.02 in the off-shell regime at $2m_\chi > M_{med}$ to $\sim$ 0.06 in the on-shell regime for heavy mediators where all coupling channels contribute.

2.1.2. Additional considerations for $V + \not{E}_T$ signatures

All models detailed in this Section are applicable to signatures where a photon, a W boson, a Z boson or a Higgs boson is radiated from the initial state partons instead of a gluon. The experimental signature is identified as $V+\not{E}_T$ and it has been sought by ATLAS and CMS in Refs. [8–11,16,17]. This signature is also produced by the models described in Section 3.

Monojet searches are generally more sensitive with respect to final states including EW bosons, due to the much larger rates of signal events featuring quark or gluon radiation with respect to

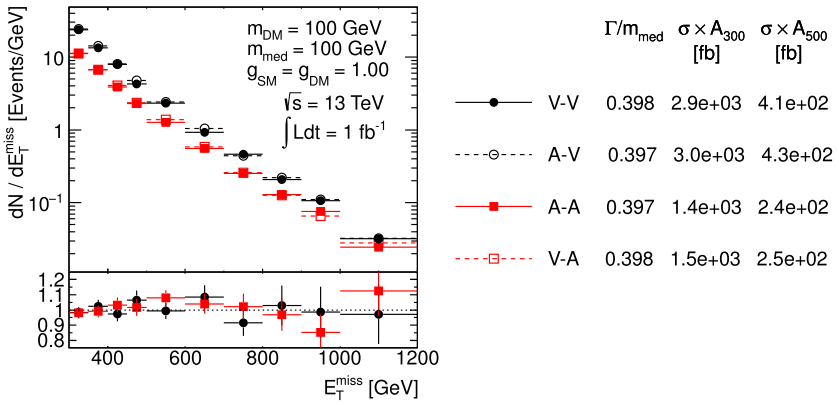

Fig. 12. Comparison of the pure vector, V-V, and pure axial-vector, A-A, couplings with mixed couplings, A-V and V-A where the first (second) letter indicates the SM (dark sector) vertex. The $\not{E}_T$ distribution is shown for the samples generated with $m_\chi = 100$ GeV and $M_{\text{med}} = 100$ GeV. Ratios of the normalized distributions are shown for A-V over V-V and for V-A over A-A. A_{300} and A_{500} in the table denote the acceptance of the $\not{E}_T > 300$ GeV and $\not{E}_T > 500$ GeV cut, respectively. The suppression by β^3 for $m_\chi \sim M_{\text{med}}$ can be seen for the curves representing axial DM coupling.

Table 1
Simplified model benchmarks for *s*-channel simplified models (spin-1 mediators decaying to Dirac DM fermions in the V and A case, taking the minimum width for $g_q = 0.25$ and $g_\chi = 1$).

m_χ / GeV	M_{med} / GeV									
1	10	20	50	100	200	300	500	1000	2000	10 000
10	10	15	50	100						10 000
50	10		50	95	200	300				10 000
150	10				200	295	500	1000		10 000
500	10						500	995	2000	10 000
1000	10							1000	1995	10 000

radiation of bosons [65], in combination with the low branching ratios if leptons from boson decays are required in the final state. The rates for the Higgs boson radiation is too low for these models to be considered a viable benchmark [48]. However, the presence of photons, leptons from W and Z decays, and W or Z bosons decaying hadronically allow backgrounds to be rejected more effectively, making $Z/\gamma/W+\not{E}_T$ searches still worth comparing with searches in the jet+$\not{E}_T$ final state (see e.g. Ref. [66]).

In the case of a spin-1 mediator, an example Feynman diagram for these processes can be constructed by taking Fig. 1 and replacing the gluon with γ, W or Z.

When the initial state radiation is a W boson, Run-1 searches have considered three benchmark cases, varying the relative coupling of the W to u and d quarks. The simplified model with a vector mediator exchanged in the s-channel includes only the simplest of these cases, in which the W coupling to u and d quarks is identical, as required naively by SU(2) gauge invariance. With some more complex model building, other cases are possible. The case in which the u and d couplings have opposite sign is particularly interesting, since this enhances the $W+\not{E}_T$ signal over the jet+ $\not{E}_T$ signal [44,67,68]. An example of a model of this type is discussed in Appendix A.4.

Simulations for the models in this Section have been done at the LO+PS level using MadGraph5_aMC@NLO 2.2.3 interfaced to Pythia 8, and therefore no special runtime configuration is needed for pythia 8. Even though merging samples with different parton multiplicities is possible, this has not been deemed necessary as the visible signal comes from the production of a heavy SM boson whose transverse momentum distribution is sufficiently well described at LO+PS level.

In these $V+\not{E}_T$ models, as in the case of the jet+$\not{E}_T$ models, p_T of the boson or the $\not{E}_T$ does not depend strongly on the width of the mediator. An example of the particle-level analysis acceptance using the generator-level cuts from Ref. [8] for the

Table 2
Minimal width of the vector mediator exchanged in *s*-channel divided by its mass, assuming $g_q = 0.25$ and $g_\chi = 1$. The numbers tabulated under $2m_\chi = M_{\text{med}}$ correspond to the width calculated for $M_{\text{med}} - 5$ GeV.

m_χ / GeV	M_{med} / GeV									
	10	20	50	100	200	300	500	1000	2000	10 000
1	0.049	0.051	0.051	0.051	0.051	0.051	0.056	0.056	0.056	0.056
10	0.022	0.024	0.054	0.052						0.056
50	0.022		0.025	0.025	0.055	0.053				0.056
150	0.022				0.025	0.025	0.061	0.058		0.056
500	0.022						0.029	0.030	0.060	0.057
1000	0.022							0.030	0.030	0.057

Table 3
Minimal width of the axial-vector mediator exchanged in *s*-channel divided by its mass, assuming $g_q = 0.25$ and $g_\chi = 1$. The numbers tabulated under $2m_\chi = M_{\text{med}}$ correspond to the width calculated for $M_{\text{med}} - 5$ GeV.

m_χ / GeV	M_{med} / GeV									
	10	20	50	100	200	300	500	1000	2000	10 000
1	0.045	0.049	0.051	0.051	0.051	0.051	0.053	0.055	0.056	0.056
10	0.020	0.022	0.047	0.050						0.056
50	0.020		0.025	0.025	0.045	0.048				0.056
150	0.020				0.025	0.025	0.044	0.053		0.056
500	0.020						0.027	0.029	0.050	0.056
1000	0.020							0.029	0.030	0.055

Table 4
Analysis acceptance ratios for the photon+$\not{E}_T$ analysis when varying the mediator width, in the case of a vector mediator exchanged in the *s*-channel. The figures shown in this Section have been obtained using a LO UFO model in MadGraph5_aMC@NLO 2.2.3 interfaced to Pythia 8 for the parton shower.

Acceptance ratio: $\Gamma = \Gamma_{\min}$ vs. $\Gamma = M_{\text{med}}/3$				
M_{med}/GeV	m_χ/GeV			
	10	50	200	400
50	0.96	0.99		0.95
100	0.97			
300	1.00	1.02		
600			0.96	
1000	1.01	1.02	1.03	
3000	1.02	1.03		1.01

photon+$\not{E}_T$ analysis, but raising the photon p_T cut to 150 GeV, is shown in Table 4, comparing a width that is set to $\Gamma = M_{med}/3$ to the minimal width (the ratio between the two widths ranges from 1.05 to 1.5 with increasing mediator masses).

Examples of relevant kinematic distributions for selected benchmark points are shown in Fig. 13.

2.2. Scalar and pseudoscalar mediator, s-channel exchange

In this section, we consider a parallel situation to the vector and axial-vector mediators in the previous sections: a real scalar or a pseudoscalar where the associated scalar is decoupled at higher energies.[6] This section is largely based on Refs. [41–43] which contain a thorough discussion of these models.

Assuming MFV, spin-0 resonances behave in a similar fashion as the SM Higgs boson. If the mediators are pure singlets of the SM, their interactions with quarks are not $SU(2)_L$ invariant. To restore this invariance, one could include the mixing of such mediators with the Higgs sector. This leads to extra interactions and a more complex phenomenology with respect to what considered in this Section (for a more complete discussion, see Refs. [42,43]). In the interest of simplicity, we do not study models including those interactions in this report as early Run-2 benchmark models, but we give an example of a model of this kind in Appendix A.6.

Relative to the vector and axial-vector models discussed above, the scalar models are distinguished by the special consequences of the MFV assumption: the very narrow width of the mediator and its extreme sensitivity to which decays are kinematically available, and the loop-induced coupling to gluons. The interaction Lagrangians are

$$\mathscr{L}_\phi = g_\chi \phi \bar{\chi}\chi + \frac{\phi}{\sqrt{2}} \sum_i \left(g_u y_i^u \bar{u}_i u_i + g_d y_i^d \bar{d}_i d_i + g_\ell y_i^\ell \bar{\ell}_i \ell_i \right) , \tag{6}$$

$$\mathscr{L}_a = i g_\chi a \bar{\chi}\gamma_5\chi + \frac{ia}{\sqrt{2}} \sum_i \left(g_u y_i^u \bar{u}_i \gamma_5 u_i + g_d y_i^d \bar{d}_i \gamma_5 d_i + g_\ell y_i^\ell \bar{\ell}_i \gamma_5 \ell_i \right) \tag{7}$$

where ϕ and a are respectively the scalar and pseudoscalar mediators, and the Yukawa couplings y_i^f are normalized to the Higgs vev as $y_i^f = \sqrt{2} m_i^f / v$.

The couplings to fermions are proportional to the SM Higgs couplings, yet one is still allowed to adjust an overall strength of the coupling to charged leptons and the relative couplings of *u*- and *d*-type quarks. As in the preceding sections, for the sake of simplicity and straightforward comparison, we reduce the couplings to the SM fermions to a single universal parameter $g_q \equiv g_u = g_d = g_\ell$. Unlike the vector and axial-vector models, the scalar mediators are allowed to couple to leptons.[7]

The relative discovery and exclusion power of each search can be compared in this framework. However, we again emphasize the importance of searching the full set of allowed channels in case violations of these simplifying assumptions lead to significant modifications of the decay rates that unexpectedly favor different channels than the mix obtained under our assumptions. The coupling g_χ parametrizes the entire dependence on the structure between the mediator and the dark sector.

Given these simplifications, the minimal set of parameters under consideration is

$$\left\{ m_\chi,\ m_{\phi/a} = M_{\text{med}},\ g_\chi,\ g_q \right\} . \tag{8}$$

Fig. 14 shows the one-loop diagrams producing a jet+X signature. The full calculation of the top loop is available at LO for DM pair production in association with one parton.

The minimal mediator width (neglecting the small contributions from quarks other than top in the loop) is given by

$$\begin{aligned} \Gamma_{\phi,a} = & \sum_f N_c \frac{y_f^2 g_q^2 m_{\phi,a}}{16\pi} \left(1 - \frac{4m_f^2}{m_{\phi,a}^2}\right)^{x/2} \\ & + \frac{g_\chi^2 m_{\phi,a}}{8\pi} \left(1 - \frac{4m_\chi^2}{m_{\phi,a}^2}\right)^{x/2} \\ & + \frac{\alpha_s^2 g_q^2 m_{\phi,a}^3}{32\pi^3 v^2} \left| f_{\phi,a}\left(\tfrac{4m_t^2}{m_{\phi,a}^2}\right) \right|^2 \end{aligned} \tag{9}$$

where $x = 3$ for scalars and $x = 1$ for pseudoscalars. The loop integrals, with f as complex functions, are

$$f_\phi(\tau) = \tau \left[1 + (1-\tau) \arctan^2 \left(\frac{1}{\sqrt{\tau - 1}} \right) \right] , \tag{10}$$

$$f_a(\tau) = \tau \arctan^2 \left(\frac{1}{\sqrt{\tau - 1}} \right) \tag{11}$$

where $\tau = 4m_t^2 / m_{\phi,a}^2$.

The minimal widths for scalar and pseudo-scalar mediators with $g_q = g_\chi = 1$ are shown in Fig. 20, illustrating the effect of choosing the SM Higgs-like Yukawa couplings for the SM fermions. For the mediator mass above twice the top quark mass m_t, the minimal width receives the dominant contribution from the top quark. For lighter mediator masses, DM dominates as the couplings to lighter quarks are Yukawa suppressed.

As shown in the diagram of Fig. 14, the lowest order process of these models already involves a one-loop amplitude in QCD, and only LO predictions are currently available. The generator used for the studies for the jet+$\not{E}_T$ signature is POWHEG [43,61,69–71], with Pythia 8 [62] for the parton shower; within this implementation, the scalar and pseudoscalar mediator benchmark models are known at LO+PS accuracy.

2.2.1. Parameter scan

Similarly as in the case of the vector and axial-vector couplings of spin-1 mediators, scans in the parameter space are performed also for the scalar and pseudo-scalar couplings of the spin-0 mediators in order to decide on the optimized parameter grid for the presentation of Run-2 results. Figs. 15–19 show the scans

[6] This assumption does not hold in a UV-complete model where the two components of the complex scalar mediator would be approximately degenerate. The complex scalar case could be studied separately in the case of heavy flavor final states given the sufficiently different kinematics.

[7] This contribution plays no role for most of the parameter space considered. The choice to allow lepton couplings follows Refs. [41,42].

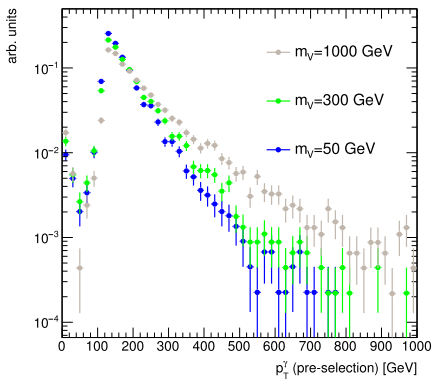

(a) Leading photon transverse momentum distribution for the photon+$\not{E}_T$ final state, for different mediator mass choices, for m_χ =10 GeV.

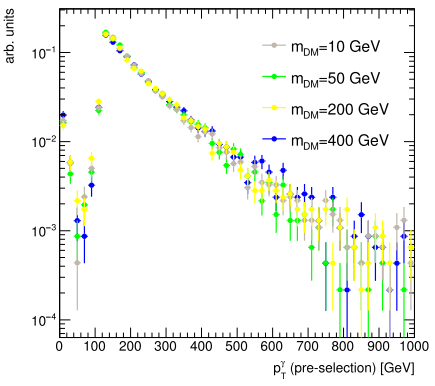

(b) Leading photon transverse momentum distribution for the photon+$\not{E}_T$ final state, for different DM mass choices, with M_{med} =1 TeV.

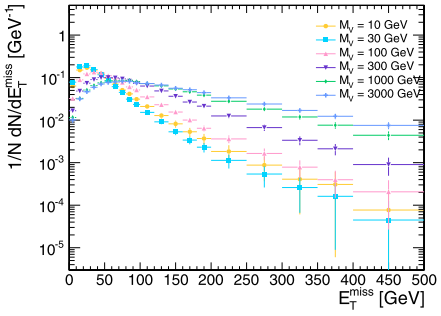

(c) Missing transverse momentum distribution for the leptonic Z+$\not{E}_T$ final state, for different mediator mass choices, for m_χ =15 GeV

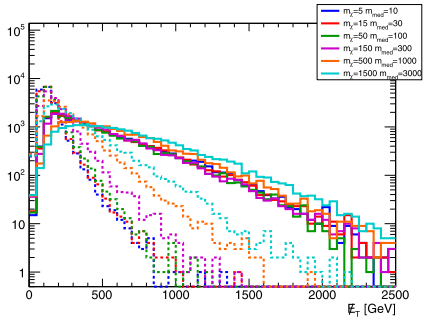

(d) Missing transverse momentum distribution for the hadronic W+$\not{E}_T$ final state.

Fig. 13. Kinematic distributions relevant for searches with W, Z and photons in the final state, for the simplified model with a vector mediator exchanged in the *s*-channel.

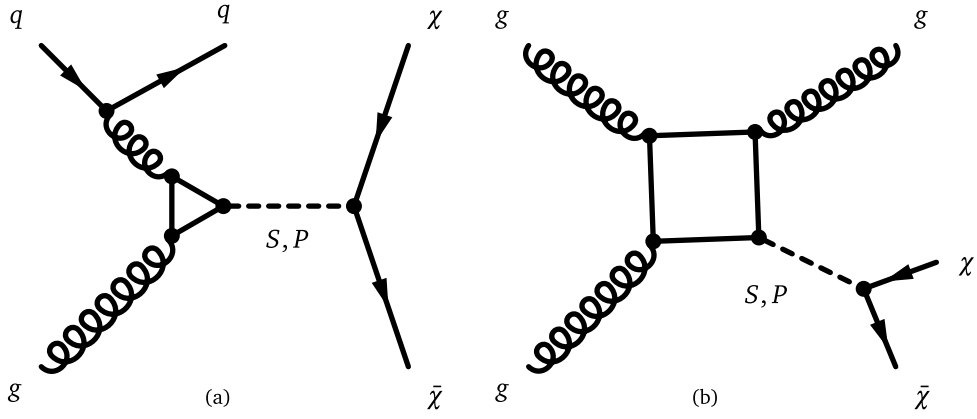

Fig. 14. One-loop diagrams of processes exchanging a scalar (S) or pseudoscalar (P) mediator, leading to a mono-jet signature.

over the couplings, DM mass and mediator mass and the same conclusions apply as in Section 2.1.

A scan over the mediator mass is shown in Fig. 19 where M_{med} = 300 GeV and 500 GeV are chosen to be below and above $2m_t$. The off-shell case is assumed by taking an extreme limit (m_χ = 1 TeV) in order to study solely the effects of the couplings to quarks. No differences in the kinematic distributions are observed and also the cross sections remain similar in this case. No significant changes appear for mediator masses around the $2m_t$ threshold.

It can be seen in Fig. 21 that the kinematics for the scalar and pseudoscalar models coincides when considering the diagrams in Fig. 14. For this reason, we recommend to fully simulate only one of the two models. No preference is given between the two models as they have the same kinematics, although it is worth noting that the pseudo-scalar model has been used for a DM interpretation of the DAMA signal and of the galactic center

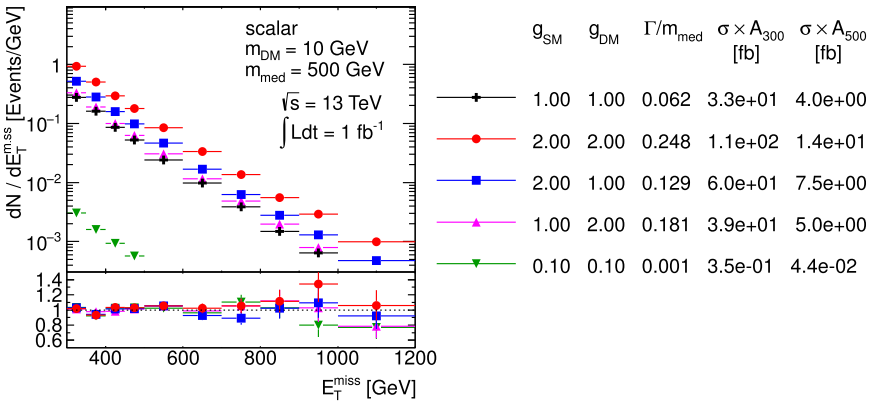

g_{SM}	g_{DM}	Γ/m_{med}	$\sigma \times A_{300}$ [fb]	$\sigma \times A_{500}$ [fb]
1.00	1.00	0.062	3.3e+01	4.0e+00
2.00	2.00	0.248	1.1e+02	1.4e+01
2.00	1.00	0.129	6.0e+01	7.5e+00
1.00	2.00	0.181	3.9e+01	5.0e+00
0.10	0.10	0.001	3.5e-01	4.4e-02

Fig. 15. Scan over couplings. The $\not{E}_T$ distribution is compared for the scalar mediator models using the parameters as indicated. Ratios of the normalized distributions with respect to the first one are shown. A_{300} and A_{500} in the table denote the acceptance of the $\not{E}_T > 300$ GeV and $\not{E}_T > 500$ GeV cut, respectively. Studies in all figures for the jet+$\not{E}_T$ signature is POWHEG, with Pythia 8 for the parton shower.

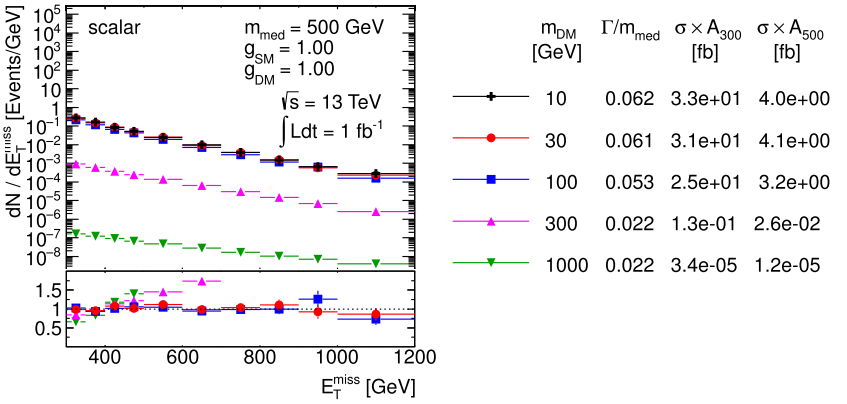

m_{DM} [GeV]	Γ/m_{med}	$\sigma \times A_{300}$ [fb]	$\sigma \times A_{500}$ [fb]
10	0.062	3.3e+01	4.0e+00
30	0.061	3.1e+01	4.1e+00
100	0.053	2.5e+01	3.2e+00
300	0.022	1.3e-01	2.6e-02
1000	0.022	3.4e-05	1.2e-05

Fig. 16. Scan over DM mass. The $\not{E}_T$ distribution is compared for the scalar mediator models using the parameters as indicated. Ratios of the normalized distributions with respect to the first one are shown. A_{300} and A_{500} in the table denote the acceptance of the $\not{E}_T > 300$ GeV and $\not{E}_T > 500$ GeV cut, respectively.

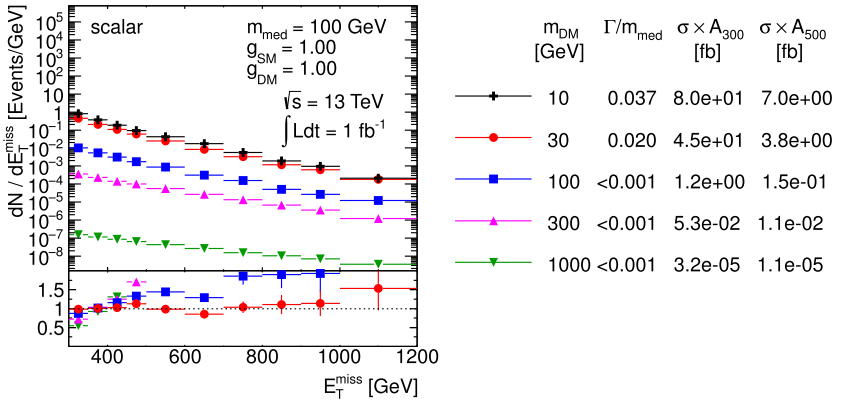

m_{DM} [GeV]	Γ/m_{med}	$\sigma \times A_{300}$ [fb]	$\sigma \times A_{500}$ [fb]
10	0.037	8.0e+01	7.0e+00
30	0.020	4.5e+01	3.8e+00
100	<0.001	1.2e+00	1.5e-01
300	<0.001	5.3e-02	1.1e-02
1000	<0.001	3.2e-05	1.1e-05

Fig. 17. Scan over DM mass. The $\not{E}_T$ distribution is compared for the scalar mediator models using the parameters as indicated. Ratios of the normalized distributions with respect to the first one are shown. A_{300} and A_{500} in the table denote the acceptance of the $\not{E}_T > 300$ GeV and $\not{E}_T > 500$ GeV cut, respectively.

excess [72]. Like in the case of the vector and axial-vector models described in , the differences between the cross sections for the scalar and pseudo-scalar samples with the same m_χ and M_{med} are increasing with the DM mass for fixed mediator mass, with the pseudo-scalar model yielding larger cross sections. There is an increasing difference between the minimal widths close to the $2m_\chi = M_{\text{med}}$ threshold.

Proposed parameter grid. The optimized parameter grid in the M_{med}–m_χ plane for scalar and pseudo-scalar mediators is motivated by similar arguments as in the previous section. Therefore, a similar pattern is followed here, with the exception of taking $g_q = g_\chi = 1$. The choice of $g_q = 0.25$ for the vector and axial-vector models is motivated by suppressing constraints from di-jets, which is not a concern in the scalar and pseudo-scalar mediator case. Here a di-jet signal emerges only at the 2-loop level through diagrams where the mediator is produced via gluon–gluon fusion and decays back into two gluons through a top loop. The strong loop suppression renders such signals unobservable at the LHC. Further constraints on the scalar and pseudo-scalar mediators may emerge from searches in $t\bar{t}$ final states. Studies

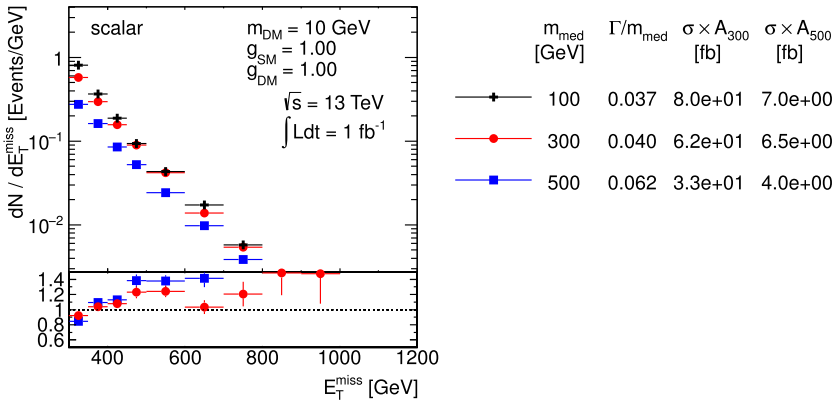

Fig. 18. Scan over mediator mass. The $\not{E}_T$ distribution is compared for the scalar mediator models using the parameters as indicated. Ratios of the normalized distributions with respect to the first one are shown. A_{300} and A_{500} in the table denote the acceptance of the $\not{E}_T > 300$ GeV and $\not{E}_T > 500$ GeV cut, respectively.

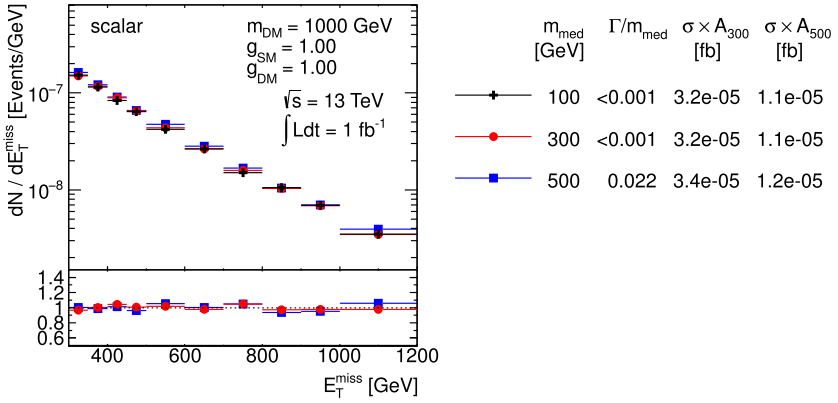

Fig. 19. Scan over mediator mass. The $\not{E}_T$ distribution is compared for the scalar mediator models using the parameters as indicated. Ratios of the normalized distributions with respect to the first one are shown. A_{300} and A_{500} in the table denote the acceptance of the $\not{E}_T > 300$ GeV and $\not{E}_T > 500$ GeV cut, respectively.

of the electroweak effects to $t\bar{t}$ production suggest that one can only expect percent level contributions for $g_q \sim O(1)$ [73]. Therefore, keeping $g_q = g_\chi = 1$ is a reasonable choice in the case of the scalar and pseudo-scalar mediators. Contrary to the vector and axial-vector models, note that couplings of 1 lead to $\Gamma_{min}/M_{med} \lesssim 0.1$, ensuring the narrow width approximation is applicable. Furthermore, the sensitivity to the highest mediator masses has to be re-evaluated. The generator level cross section times the acceptance at $\not{E}_T > 500$ GeV for the model with couplings $g_q = g_\chi = 1$, light DM of $m_\chi = 10$ GeV and a $M_{med} = 500$ GeV scalar mediator is at the order of 10 fb, i.e. just at the edge of the early Run-2 sensitivity. Increasing the mediator mass to 1 TeV pushes the product $\sigma \times A$ down to approximately 0.1 fb, below the LHC sensitivity. Therefore, we choose to remove the 2 TeV mediator mass from the grid and present the final grid with 33 mass points only, as shown in Table 5. One point at very high mediator mass (10 TeV) is added for each of the DM masses scanned, to aid the reinterpretation of results in terms of contact interaction operators (EFTs).

For the parameter grid for scalar and pseudo-scalar mediator s-channel exchange, the Γ_{min}/M_{med} ratio is given in Tables 6 and 7, respectively. In the on-shell regime, the ratio is between 0.04 and 0.1. Very narrow resonances with $\Gamma_{min}/M_{med} < 0.001$ correspond to the mass points where the mediator is off-shell. Note that the loop-induced contribution from gluons is ignored in the width calculation.

2.2.2. Additional considerations for $V + \not{E}_T$ signatures

The discussion of parameters for the model with a color-singlet, spin-0 mediator parallels that in Section 2.

Table 5
Simplified model benchmarks for s-channel simplified models (spin-0 mediators decaying to Dirac DM fermions in the scalar and pseudoscalar case, taking the minimum width for $g_q = 1$ and $g_\chi = 1$).

m_χ (GeV)	M_{med} (GeV)								
1	10	20	50	100	200	300	500	1000	10 000
10	10	15	50	100					10 000
50	10		50	95	200	300			10 000
150	10				200	295	500	1000	10 000
500	10						500	995	10 000
1000	10							1000	10 000

Even though the sensitivity of mono-boson searches to this model is low and it may not be in reach of early LHC searches, this model can be generated for W, Z and photon searches in order to reproduce the kinematics of contact interaction operators that are further described in Section 3.2.1, to aid later reinterpretation.

Other models of DM that couple dominantly to electroweak gauge bosons through either pseudo-scalar or vector mediators can be found in Ref. [74].

2.2.3. Additional considerations for $t\bar{t}$ and $b\bar{b} + \not{E}_T$ signatures

With the MFV assumption, the top and bottom quark can play an important role in the phenomenology. The scalar and pseudoscalar mediator models predict not only the monojet process described in Section 2.2, but also production of Dark Matter in association with top (or bottom) pairs, as illustrated in Fig. 22. Dedicated searches including jets from heavy flavor quarks in the final state can be designed for this signature. Another class of

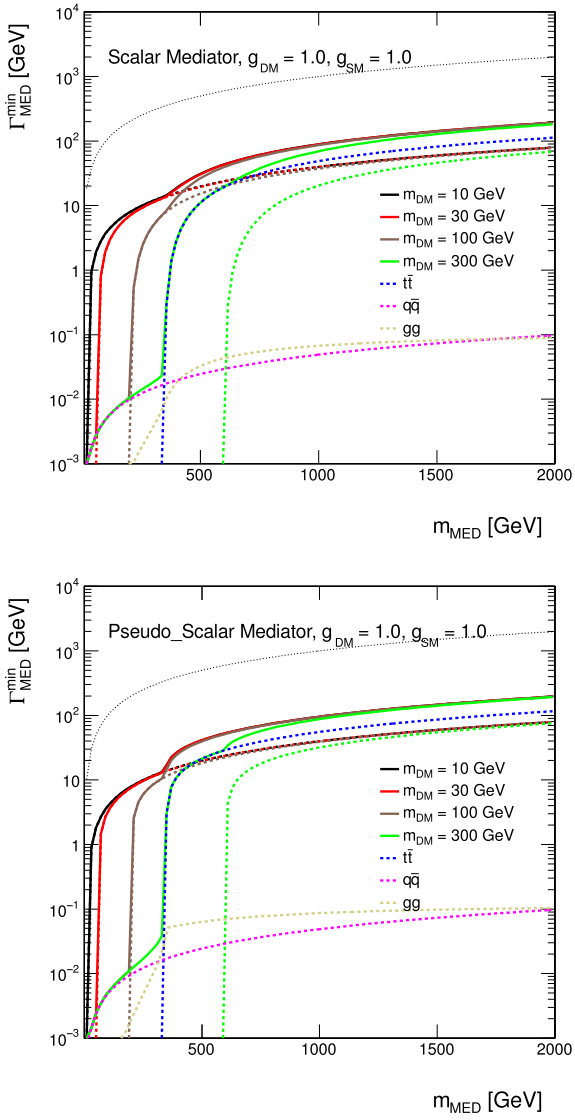

Fig. 20. Minimal width as a function of mediator mass for scalar and pseudo-scalar mediator assuming couplings of 1. The total width is shown as solid lines for DM masses of m_χ = 10 GeV, 30 GeV, 100 GeV and 300 GeV in black, red, brown and green, respectively. The individual contributions from DM are indicated by dotted lines with the same colors. The contribution from all quarks but top is shown as magenta dotted line and the contribution from top quarks only is illustrated by the dotted blue line. The dotted beige line shows the contribution from the coupling to gluons. The dotted black line shows the extreme case $\Gamma_{\rm min} = M_{\rm med}$. (For interpretation of the references to color in this figure legend, the reader is referred to the web version of this article.)

simplified models, which includes a Dark Matter interpretation among many others, and yields a single top quark in the final state, is detailed in Appendix A.1.

In addition to the $t\bar{t}$+DM models illustrated in Fig. 22, some theoretically motivated scenario (e.g. for high $tan\beta$ in 2HDM in the pMSSM) privilege the coupling of spin-0 mediators to down generation quarks. This assumption motivates the study of final states involving b-quarks as a complementary search to the $t\bar{t}$+DM models, to directly probe the b-quark coupling. An example of such a model can be found in Ref. [42] and can be obtained by replacing top quarks with b quarks in Fig. 22. Note that, because of the kinematics features of b quark production relative to heavy t quark production, a $b\bar{b}$+DM final state may only yield one experimentally visible b quark, leading to a mono-b signature in a model that conserves b flavor.

Dedicated implementations of these models for the work of this Forum are available at LO+PS accuracy, even though the state of the art is set to improve on a timescale beyond that for early Run-2 DM searches as detailed in Section 4.1.5. The studies in this Section have been produced using a leading order UFO model within MadGraph5_aMC@NLO 2.2.2 [75–77] using Pythia 8 for the parton shower.

Parameter scan. The parameter scan for the dedicated $t\bar{t}$+$\not{E}_T$ searches has been studied in detail to target the production mechanism of DM associated with heavy flavor quarks, and shares many details of the scan for the scalar model with a gluon radiation. The benchmark points scanning the model parameters have been selected to ensure that the kinematic features of the parameter space are sufficiently represented. Detailed studies were performed to identify points in the m_χ, $m_{\phi,a}$, g_χ, $g_{\rm q}$ (and $\Gamma_{\phi,a}$) parameter space that differ significantly from each other in terms of expected detector acceptance. Because missing transverse momentum is the key observable for searches, the mediator p_T spectra is taken to represent the main kinematics of a model. Another consideration in determining the set of benchmarks is to focus on the parameter space where we expect the searches to be sensitive during the 2015 LHC run. Based on a projected integrated luminosity of 30 fb^{-1} expected for 2015, we disregard model points with a cross section times branching ratio smaller than 0.1 fb, corresponding to a minimum of one expected event assuming a 0.1% efficiency times acceptance.

The kinematics is most dependent on the masses m_χ and $m_{\phi,a}$. Figs. 23 and 24 show typical dependencies for scalar and pseudoscalar couplings respectively. Typically, the mediator p_T spectrum broadens with larger $m_{\phi,a}$. The kinematics are also different between on-shell ($M_{\rm med} > 2m_\chi$) and off-shell ($M_{\rm med} < 2m_\chi$) mediators as discussed in Section 2.2. Furthermore, the kinematic differences in the $\not{E}_T$ spectrum between scalar and pseudoscalar are larger for light mediator masses with respect to heavier mediators. It is therefore important to choose benchmark points covering on-shell and off-shell mediators with sufficient granularity, including the transition region between on-shell and off-shell mediators.

Typically only weak dependencies on couplings are observed (see Fig. 25) where the variation with width of the integral over parton distributions is unimportant. As shown in Section 2.1.1, for couplings $\sim O(1)$ the width is large enough that the p_T of the mediator is determined mainly by the PDF.

At large mediator masses ($\sim$ 1.5 TeV) or very small couplings ($\sim 10^{-2}$), width effects are significant, but these regimes have production cross sections that are too small to be relevant for 30 fb^{-1} and are not studied here. However, with the full Run 2 dataset, such models may be within reach.

Another case where the width can impact the kinematics is when $m_{\phi,a}$ is slightly larger than $2m_\chi$. Here, the width determines the relative contribution between on-shell and off-shell mediators. An example is given in Fig. 26. As the minimal width choice pursued in this document is the most conservative one, this effect can be neglected in order to reduce the number of benchmark points to be generated.

The points for the parameter scan chosen for this model are listed in Table 5, chosen to be harmonized with those for other analyses employing the same scalar model as benchmark. Based on the sensitivity considerations above, DM masses are only simulated up to 500 GeV (but the 5 TeV mediator point is retained) leading to a total of 24 benchmark points. However for these searches we recommend to generate and simulate scalar and pseudoscalar models separately, as the kinematics differs due to the different coupling of the mediator to the final state top quarks in the two cases, as shown in Figs. 23 and 24.

Table 6
Minimal width of the scalar mediator exchanged in s-channel divided by its mass, assuming $g_q = g_\chi = 1$. The loop-induced gluon contribution is ignored. The numbers tabulated under $2m_\chi = M_{med}$ correspond to the width calculated for $M_{med} - 5$ GeV.

m_χ / GeV	M_{med} / GeV								
	10	20	50	100	200	300	500	1000	10 000
1	0.040	0.040	0.040	0.040	0.040	0.040	0.062	0.089	0.099
10	<0.001	<0.001	0.040	0.040					0.099
50	<0.001		<0.001	<0.001	0.040	0.040			0.099
150	<0.001				<0.001	<0.001	0.062	0.089	0.099
500	<0.001						0.022	0.049	0.099
1000	<0.001							0.049	0.099

Table 7
Minimal width of the pseudo-scalar mediator exchanged in s-channel divided by its mass, assuming $g_q = g_\chi = 1$. The loop-induced gluon contribution is ignored. The numbers tabulated under $2m_\chi = M_{med}$ correspond to the width calculated for $M_{med} - 5$ GeV.

m_χ / GeV	M_{med} / GeV								
	10	20	50	100	200	300	500	1000	10 000
1	0.040	0.040	0.040	0.040	0.040	0.040	0.083	0.095	0.099
10	<0.001	<0.001	0.040	0.040					0.099
50	<0.001		<0.001	<0.001	0.040	0.040			0.099
150	<0.001				<0.001	<0.001	0.083	0.095	0.099
500	<0.001						0.043	0.056	0.099
1000	<0.001							0.056	0.099

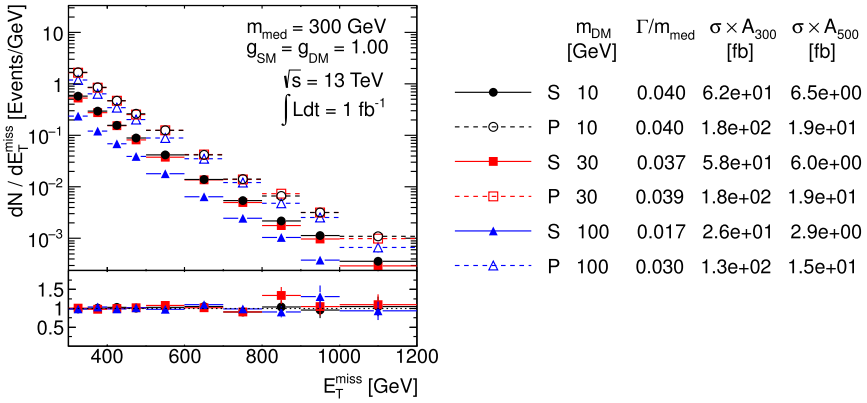

Fig. 21. Comparison of the $\not{E}_T$ distributions for the scalar and pseudoscalar models for different $M_{med} = 300$ GeV and different DM masses. Ratios of the normalized distributions with respect to the first one are shown. A_{300} and A_{500} in the table denote the acceptance of the $\not{E}_T > 300$ GeV and $\not{E}_T > 500$ GeV cut, respectively.

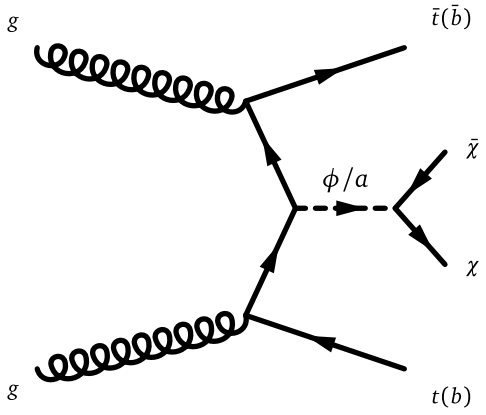

Fig. 22. Representative Feynman diagram showing the pair production of Dark Matter particles in association with $t\bar{t}$ (or $b\bar{b}$).

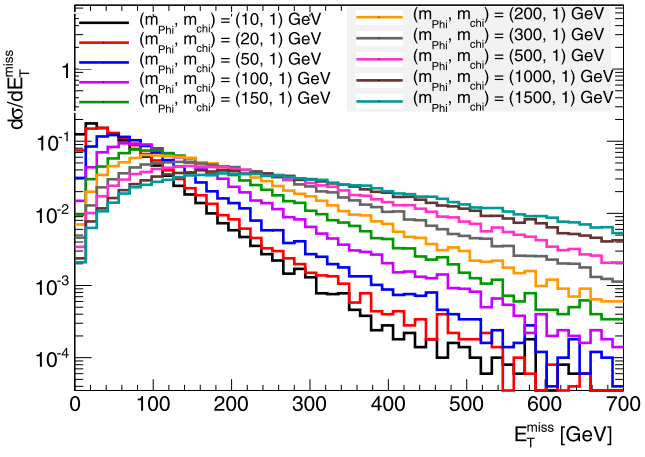

Fig. 23. Example of the dependence of the kinematics on the scalar mediator mass in the $t\bar{t}+\not{E}_T$ signature. The Dark Matter mass is fixed to be $m_\chi = 1$GeV.

Similar studies were performed in the $b\bar{b}$ case. It was found that they show the same weak dependence of the kinematics of the event on the mediator width. The same benchmark parameters of the $t\bar{t}$ case could then be chosen.

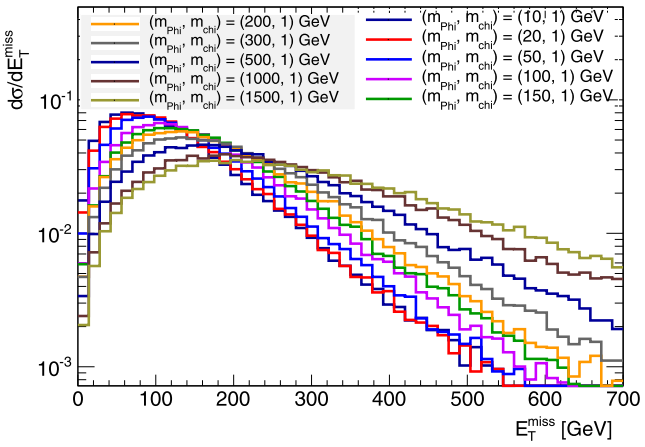

Fig. 24. Example of the dependence of the kinematics on the pseudoscalar mediator mass in the $t\bar{t}+\not{E}_T$. The Dark Matter mass is fixed to be $m_\chi = 1$GeV. All figures concerning the $t\bar{t}+\not{E}_T$ signature have been produced using a leading order model within MadGraph5_aMC@NLO 2.2.2, using Pythia 8 for the parton shower.

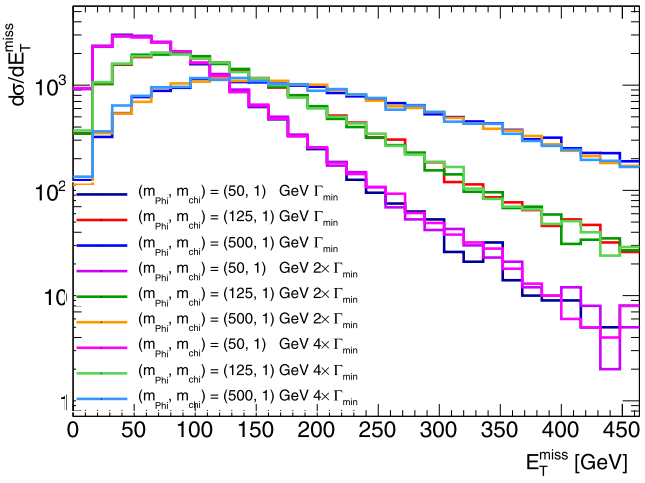

Fig. 25. Study of the dependence of kinematics on the width of a scalar mediator $t\bar{t}+\not{E}_T$. The width is increased up to four times the minimal width for each mediator and Dark Matter mass combination.

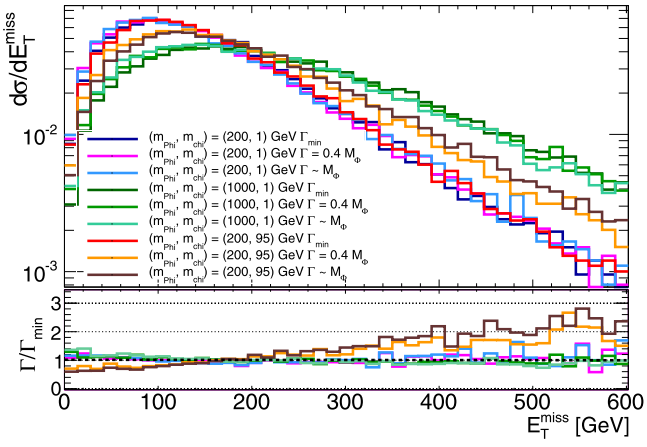

Fig. 26. Dependence of the kinematics on the width of a scalar mediator $t\bar{t}+\not{E}_T$. The width is increased up to the mediator mass. Choices of mediator and Dark Matter masses such that $m_{\phi,a}$ is slightly larger than $2m_\chi$ is the only case that shows a sizeable variation of the kinematics as a function of the width.

2.3. Colored scalar mediator, t-channel exchange

The preceding sections address models with a Dirac fermion coupled to the SM through exchange of a neutral spin-0 or spin-1 particle in an *s*-channel process. A *t*-channel process may couple the SM and DM directly, leading to a different phenomenology. For completeness, we examine a model where χ is a Standard Model (SM) singlet, a Dirac fermion; the mediating particle, labeled ϕ, is a charged scalar color triplet and the SM particle is a quark. Such models have been studied in Refs. [34,36,38,46,78,79]. However, these models have not been studied as extensively as others in this Forum.

Following the example of Ref. [78], the interaction Lagrangian is written as

$$\mathscr{L}_{\rm int} = g \sum_{i=1,2} (\phi_{(i),L}\bar{Q}_{(i),L} + \phi_{(i),u,R}\bar{u}_{(i),R} + \phi_{(i),d,R}\bar{d}_{(i),R})\chi \qquad (12)$$

where $Q_{(i),L}$, $u_{(i),R}$ and $d_{(i),R}$ are the SM quarks of the ith generation and $\phi_{(i),L}$, $\phi_{(i),u,R}$ and $\phi_{(i),d,R}$ are the corresponding mediators, which (unlike the *s*-channel mediators) must be heavier than χ. These mediators have SM gauge representations under $(SU(3), SU(2))_Y$ of $(3,2)_{-1/6}$, $(3,1)_{2/3}$ and $(3,1)_{-1/3}$ respectively. Variations of the model previously studied in the literature include coupling to the left-handed quarks only [79,80], to the $\phi_{(i),u,R}$ [34] or $\phi_{(i),d,R}$ [39,78], or some combination [36,38].

The minimal width of each mediator is expressed, using the example of decay to an up quark, as

$$\Gamma(\phi_{(i)} \to \bar{u}_{(i)}\chi) = \frac{g^2_{(i)}}{16\pi M^3_{\phi_{(i)}}}(M^2_{\phi_{(i)}} - m^2_{u_{(i)}} - m^2_\chi) \times \sqrt{(M^2_{\phi_{(i)}} - (m_{u_{(i)}} + m_\chi)^2)(M^2_{\phi_{(i)}} - (m_{u_{(i)}} - m_\chi)^2)}, \qquad (13)$$

which reduces to

$$\frac{g^2_{(i)} M_{\phi_{(i)}}}{16\pi}\left(1 - \frac{m^2_\chi}{M^2_{\phi_{(i)}}}\right)^2 \qquad (14)$$

in the limit $M_{\phi_{(i)}}, m_\chi \gg m_{u_{(i)}}$.

The generation index i for $\phi_{(i)}$ is linked to the incoming fermion(s), and it runs on all three quark generations due to the MFV assumption. Ref. [78] considers two extreme cases for this model in terms of cross-sections: the case in which all mediator flavors are present, leading to the maximal cross-section, and the case in which only right-handed down-type mediators are present. Neither of the models in this reference include couplings to the third quark generation, leading to a violation of the MFV assumption. In the case of purely down-type right-handed squarks this is still safe from flavor constraints. Furthermore, reintroducing the third generation squarks would lead to models that produce qualitatively similar signals in the mono-jet and SUSY squark searches, the main difference being the production cross-section. At the same time the presence of third generation squarks will lead to further constraints from other searches such as those for mono-bjets, for stops and for sbottoms, as discussed in Section 2.3.2. The studies in this Section are performed using a model with a mediator coupling to all three generation, following Ref. [46]. Further differences between the two models (hypercharge, chirality) only lead to a change in the cross-section. The LO UFO model is interfaced to MadGraph5_aMC@NLO v2.2.3, but it was not possible to go beyond parton-level studies and interface those models to a parton shower in time for the conclusion of this Forum. The state of the art for calculating these models is LO+PS, and the implementation of multi-parton merging has been studied in detail [78,81–83], and further studies should be

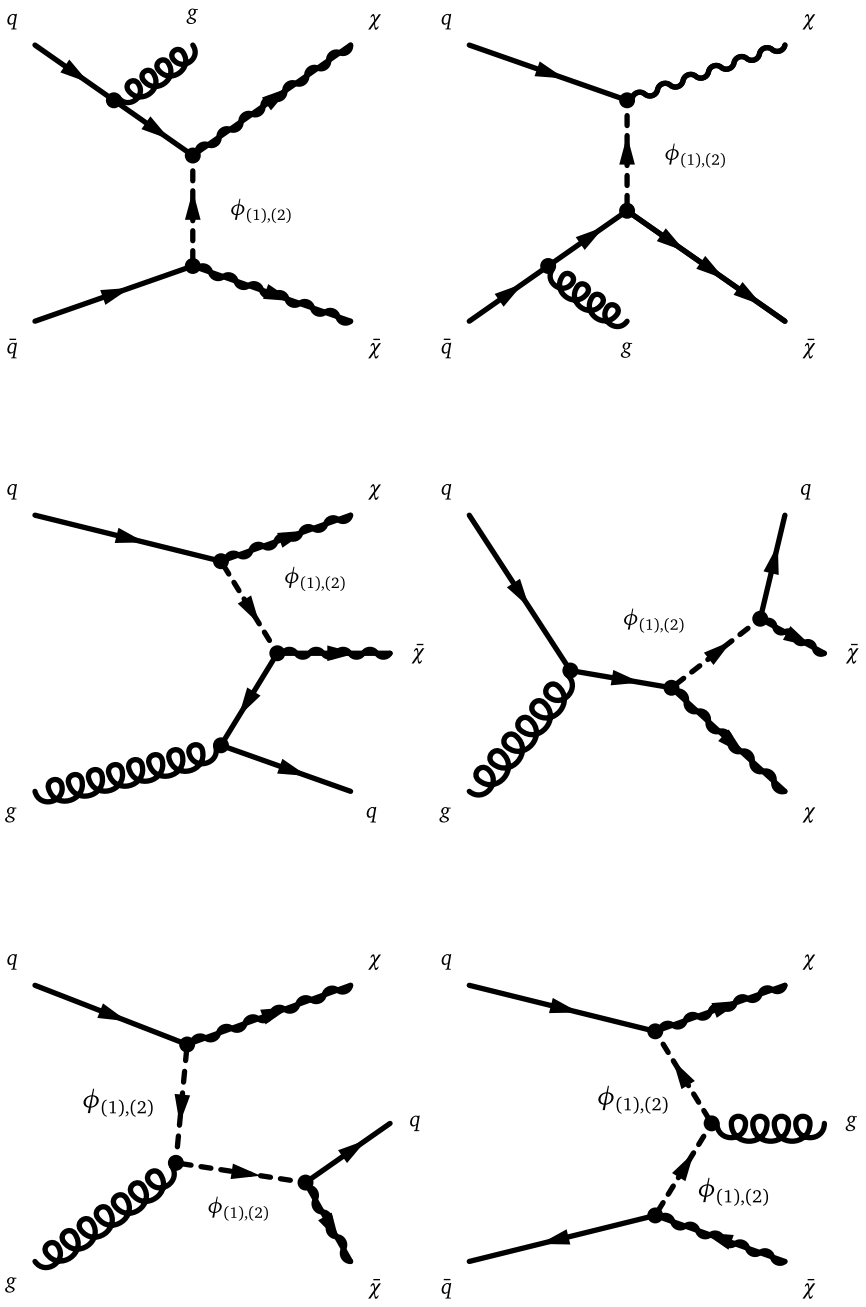

Fig. 27. Leading order mono-jet t-channel processes.
Source: Adapted from [78].

undertaken prior to generating signal samples for early Run-2 LHC searches.

The leading-order processes involved in $\not{E}_T$+jet production are shown in Fig. 27. This model can also give a signal in the $\not{E}_T$ + di-jet channel when, for example, the χ is exchanged in the t-channel and the resulting ϕ pair each decay to a jet + χ. Fig. 28 shows the leading order diagrams. Except for the gg induced process, di-jet production through the third-generation mediator $\phi_{(3),u}$ is not possible, and production through $\phi_{(3),d}$ is suppressed. However, if the coupling g includes a Yukawa coupling proportional to the quark mass, and g is sufficiently large, LHC searches will still be sensitive to this model, as explained in Section 2.3.2.

The diagram involving the t-channel exchange of χ is strongly dependent upon the Dirac fermion assumption. For a Majorana fermion, $q\bar{q}$, $\bar{q}\bar{q}$, and qq production would be possible with the latter having a pronounced enhancement at the LHC.

This model is similar to the simplified model considered in SUSY searches, implemented as the MSSM with only light squarks and a neutralino, except for two distinct points: the χ is a Dirac fermion and the coupling g is not limited to be weak scale ($g \ll 1$). In the MSSM, most of these processes are sub-dominant, even if resonantly enhanced, because the production is proportional to weak couplings. In the more general theories considered here, g is free to take on large values of order 1 or more, and thus diagrams neglected in MSSM simulation can occur at a much higher rate here. While constraints from SUSY jets+$\not{E}_T$ analyses on MSSM models can be recast to apply to the specific model in this report, DM searches should also directly test their sensitivity to the MSSM benchmark models.

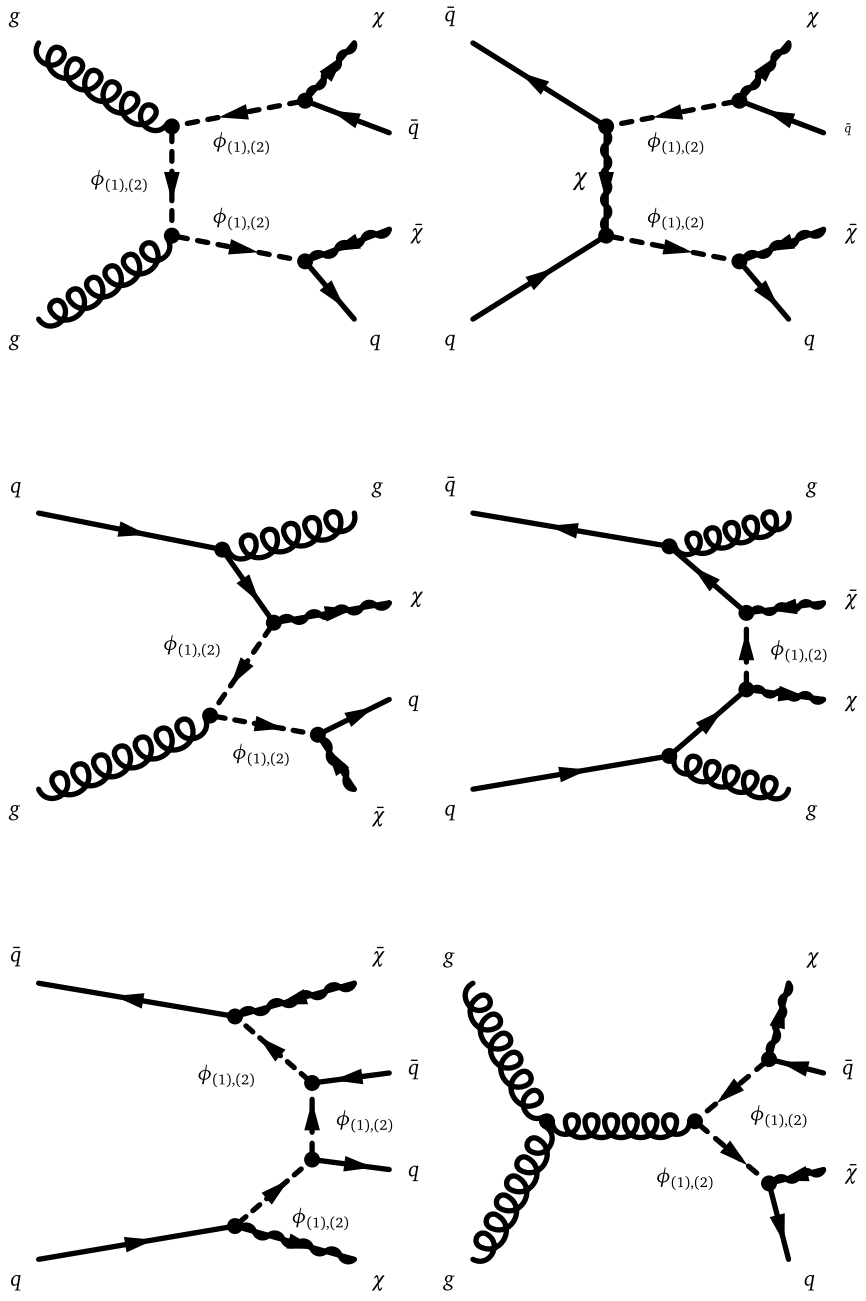

Fig. 28. Leading order two-jet t-channel processes.
Source: Adapted from [78].

The state of the art calculation for these models is LO and they can be interfaced with a parton shower program. The studies in this Section use a LO model implementation within MadGraph5_aMC@NLO v2.2.3, but no parton shower could be employed in the time-frame of the conclusions of this Forum. Further implementation details can be found in Section 4.1.3.

2.3.1. Parameter scan

As for the s-channel models, we adopt the simplifying assumption that the mediator masses and couplings are equal for each flavor and handedness. The free parameters are then

$$\{m_\chi,\ M_\phi,\ g\}. \tag{15}$$

Ref. [78] studies the parameter space and obtains bounds on this model from LHC Run-1 mono-jet and dijets+$\not{E}_T$ data. The Forum did not exhaustively compare the kinematic distributions of the t-channel models as done in the s-channel case. In particular, the absence of a parton shower simulation can affect some of the conclusions on the points and sensitivity chosen. While this means the conclusions on the parameter scan below should be taken with more caution, the model is plausible and distinctive, and it should be included in the design of early Run-2 LHC searches.

As in the s-channel models, scans should be performed over m_χ and M_ϕ. The viable ranges of both parameters nearly coincide with the scan proposed for the s-channel. For the early Run-2 searches, we recommend to generate and fully simulate a subset of the s-channel mono-jet grid that accounts for the on-shell and off-shell regions. In contrast to the s-channel case, the bounds one obtains from $\not{E}_T$+X searches depend strongly on the width of the mediator, as is visible in Figs. 5 and 6 of Ref. [78] and in

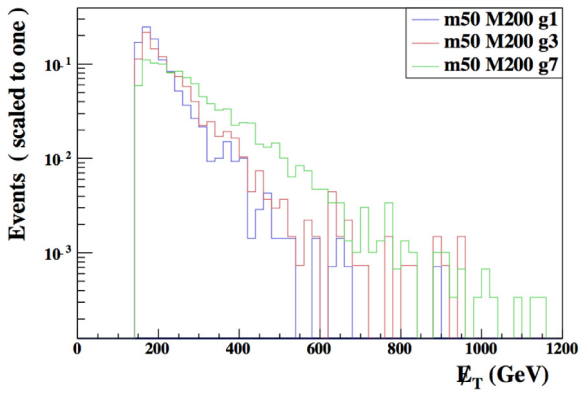

(a) $\not{E}_T$ distribution for a 200 GeV t-channel mediator, when varying the couplings.

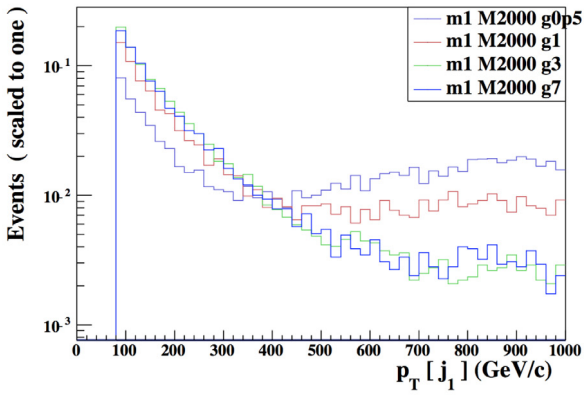

(b) Leading jet p_T distribution for a 2 TeV t-channel mediator with small (g=0.5) to large (g=7) couplings with a DM mass of 1 GeV

Fig. 29. Kinematic distributions normalized to unit area from the t-channel model from Ref. [46], using MadAnalysis [84,86] and simplified analysis cuts on the leading jet $p_T > 150$ GeV and $\eta < 2.8$, $\not{E}_T > 150$ GeV. For these models, a LO UFO model is interfaced to MadGraph5_aMC@NLO v2.2.3, and studies are at parton-level only.

Fig. 29(a), except in the heavy mediator limit ($M_\phi \approx 2$ TeV). This figure has been obtained applying a simplified analysis selection (cuts on the leading jet $p_T > 150$ GeV and $\eta < 2.8$, $\not{E}_T > 150$ GeV.) using MadAnalysis [84,85]. Fig. 29(b) also shows that, if the DM mass is low and the mediator is produced on-shell and its width is narrow, the cross-section is dominated by $qg \rightarrow q\chi\chi$ diagram. The mediator energy is then split evenly between the light DM particles and the quark, leading to a broad enhancement at $M_{\text{med}}/2$.

Points with distinct kinematic distributions for a preliminary scan in $\{ m_\chi, M_\phi, g\}$ are selected taking into account the expected sensitivity of Run-2 searches, and requiring at least 100 events to pass the kinematic cuts outlined for Fig. 29 in 25 fb^{-1} of collected data, and respect $\Gamma/M_{\text{med}} < 1$. They are outlined in Table 8. The conclusions in this table may change when a parton shower is employed together with multiparton matching.

2.3.2. Additional considerations for $V + \not{E}_T$ signatures

The models and parameters with emission of an EW boson generally follow those in Section 2.3. even though different diagrams are involved. A representative Feynman diagram can be constructed by replacing a final-state gluon in Fig. 27 with a γ, W, Z boson, but radiation of electroweak bosons directly from the mediator also leads to a mono-boson signature.

Table 8
Simplified model benchmark points for t-channel simplified model (spin-0 mediators coupling to Dirac DM fermions, taking the minimum width).

m_χ / GeV	M_{med} / GeV							Couplings
1	10	50	100	300				0.1, 1, 3, 7
1					500	1000		0.25, 1, 3, 7
1							2000	1, 3, 7
50		55						0.1, 1, 3, 4π
50			200	300				0.1, 1, 3, 7
500					550			1, 3
500						1000		0.25, 1, 3
500							2000	3
1000						1100		3, 4π
1000							2000	3

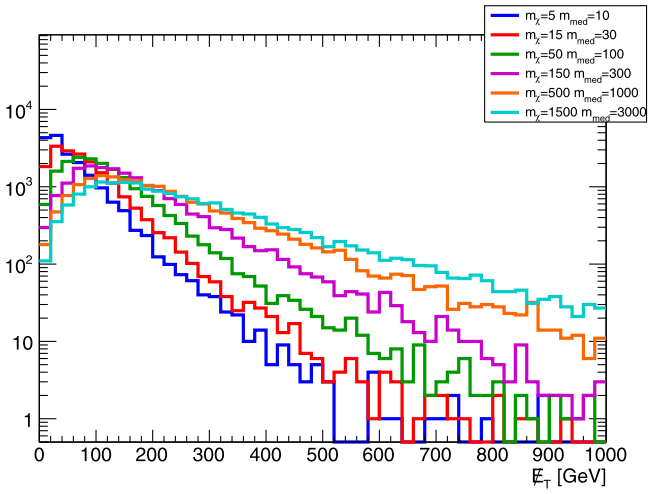

Fig. 30. Missing transverse momentum distribution for the hadronic Z+$\not{E}_T$ final state, for the simplified model with a colored scalar mediator exchanged in the t-channel.

The models considered in Section 2.3 present a relevant difference concerning final states with an electroweak boson. In the model in [46], both right- and left-handed mediators can radiate a Z boson, while only the left-handed mediator in [46] allows for W and Z radiation.

The studies in this Section use the LO+PS UFO model from [46] in MadGraph5_aMC@NLO v2.2.3, using Pythia 8 for the parton shower. Fig. 30 shows the $\not{E}_T$ distribution for the hadronic Z+$\not{E}_T$ final state, with varying DM and mediator mass, before any selection. The acceptance for a series of basic analysis selections ($\not{E}_T$ >350 GeV, leading jet $p_T > 40$ GeV, minimum azimuthal angle between jet and $\not{E}_T > 0.4$) applied at the generator level is shown in Fig. 31.

The discussion of the parameter scan for the t-channel model in the case of signatures including EW bosons parallels that of the monojet case for mediator and DM masses, but no kinematic dependence on the width is observed, so a coupling scan is not needed.

Additional considerations for signatures with $b-$quarks $+ \not{E}_T$. Models of bottom-flavored Dark Matter that are closely related to the t-channel mediated model from this Section have been proposed in Refs. [87,88]. We describe the b-FDM model of Ref. [88], created to explain the Galactic Center (GC) gamma-ray excess observed in data collected by the Fermi-LAT collaboration [89,90]. This model favors couplings to third-generation quarks via Yukawa couplings, therefore respecting the MFV assumption.

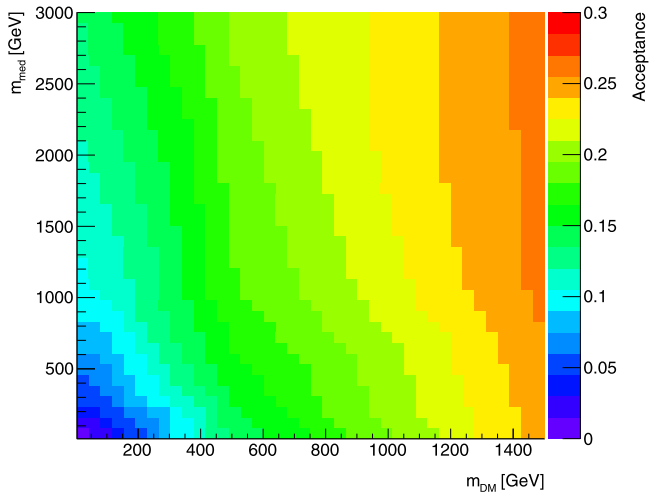

Fig. 31. Acceptance for the hadronic Z+$\not{E}_T$ final state, for the simplified model with a colored scalar mediator exchanged in the t-channel.

The model contains a Dirac fermion transforming as a flavor triplet, exclusively coupling to right-handed down-type quarks. The third component of the triplet χ_b comprises the cosmological DM. Within the MFV framework, the other fermions in the flavor triplet can be made sufficiently heavy and weakly-coupled that they can be neglected in the analysis. A flavor singlet, color triplet scalar field Φ mediates the interactions between the DM and the Standard Model quarks. The model is similar to the MSSM with a light bottom squark and neutralino, and is thus a flavor-specific example of a t-channel model. Similar top-flavored models can exist, as e.g. in Refs. [91,92]. In the case where the top coupling is the main DM coupling, the signal is very similar to a signal from a stop quark, since unlike the other t-channel cases there is no top in the initial state parton distribution functions (PDFs). This is the reason why it was not considered as an additional model. More recent literature shows that other flavor states could also contribute to LHC signals, as shown in Ref. [93], but such models will have to be investigate on a longer timescale with respect to that of this Forum.

The Lagrangian considered is given by

$$-\mathscr{L} \supset g\Phi^* \bar{\chi}_b b_R + \text{h.c.} \tag{16}$$

This model is known at LO+PS accuracy, and the studies in this Section use a LO model implementation within MadGraph5_aMC@NLO v2.2.3 interfaced to Pythia 8 for the parton shower. Further implementation details can be found in Section 4.1.5.

Parameter scan. In this model, the interference of diagrams with QCD production of the mediator (which scale as g_s^2) with diagrams that are proportional to the coupling g in the $b+\not{E}_T$ and $b\bar{b}+\not{E}_T$ final states. In the case of large couplings, this is not conducive to a simple scaling behavior that would allow us to reduce the number of points to be simulated. This can be seen in Fig. 33.

A full study of the parameter scan for this model was not available for this report; thus for early Run-2 searches we recommend scanning a range of possible widths as discussed in a more limited way than for the t-channel mono-jet, spanning from the minimal width to a value approaching the particle limit, e.g. $g = 0.5, 1, 2, 3$. A coupling benchmark such as $g = 1$ should be considered for each mass point since this would be a distinctive feature of this benchmark from SUSY models with sbottom squarks (see Section 2.3 for further discussion).

A scan of Dark Matter and mediator masses should be done in the on-shell region $M_\Phi > m_\chi + m_b$, since the cross-sections in the off-shell region are too small to be probed with early LHC data, spanning from 10 to 500 GeV in m_χ and from 10 to 1300 GeV in M_Φ. Examples of the kinematic distributions produced by this model are shown in Fig. 32.[8]

2.4. Spin-2 mediator

In models with extra dimensions, the Kaluza–Klein excitations of the graviton could also serve as a mediator between the SM and dark sector physics. This kind of model was not studied in the forum and is not included in the recommendations, but models such as Ref. [94,95] may warrant further study on a longer timescale.

2.5. Presentation of results for reinterpretation of s-channel mediator models

The aim of the parameter grid optimization done for the s-channel models in the previous sections is to reduce the parameter space that must be simulated. We then need a procedure for populating the full parameter space by using the simulated grid points. We recommend doing this as follows:

- When the dependences on parameters are known, the cross sections and efficiencies at general points can be calculated from the grid data.
- In other cases, this information can be obtained by interpolation between the grid points. We have chosen the grid points so that the dependence is sufficiently smooth that this will be possible.

The results of the scan over the couplings presented in the previous sections indicate that there are no changes in kinematic distributions for different choices of the coupling strengths. This means that the acceptance remains the same in the whole g_q–g_χ plane and it is sufficient to perform the detector simulation only for one single choice of g_q, g_χ. The resulting truth-level selection acceptance and the detector reconstruction efficiency can then be applied to all remaining grid points in the g_q–g_χ plane where only the generator-level cross section needs to be known. This significantly reduces the computing time as the detector response is by far the most CPU-intensive part of the Monte Carlo sample production. However, the number of generated samples can be reduced even further if a parameterization of the cross section dependence from one grid point to another exists. In this section, we describe the details of a cross section scaling procedure that can be used to reinterpret results for a fixed coupling for s-channel mediator models. The studies in this section employ the POWHEG [43] generator.

The propagator for the s-channel exchange is written in a Breit–Wigner form as $\frac{1}{q^2 - M_{\text{med}}^2 + iM_{\text{med}}\Gamma}$, where q is the momentum transfer calculated from the two partons entering the hard process after the initial state radiation, which is equivalent to the momentum of the DM pair.[9] The size of the momentum transfer with respect to the mediator mass allows us to identify three cases:

[8] Following the grounding assumptions in this report, the normalization to the relic density is considered only in these example plots rather than as a necessary ingredient for the parameter scan of this model.

[9] Using a running width and replacing the denominator of the propagator with $q^2 - M_{\text{med}}^2 + iQ^2\frac{\Gamma}{M_{\text{med}}}$ should be considered in the case of wide mediators [96].

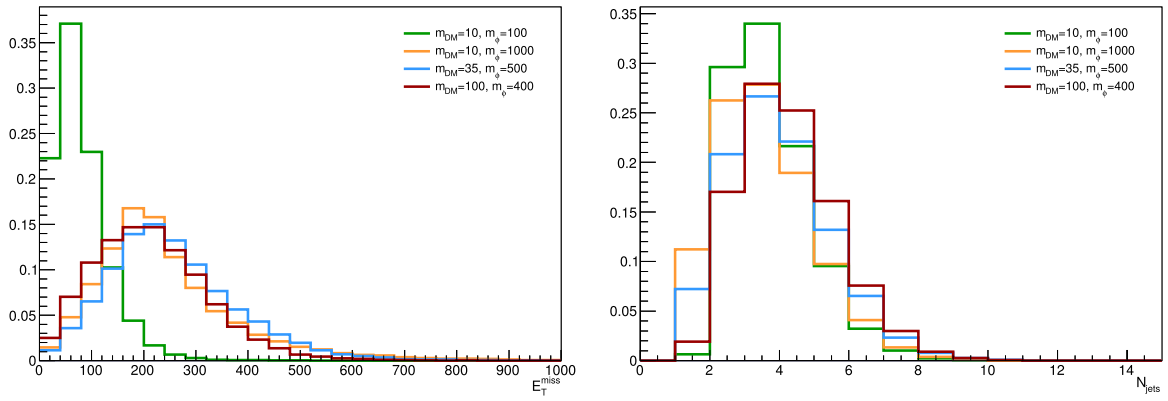

Fig. 32. $\not{E}_T$ (left) and jet multiplicity (right) for various DM and mediator masses and couplings normalized to the relic density observed in the early universe. Studies in this section use a LO UFO model implementation within MadGraph5_aMC@NLO v2.2.3 interfaced to Pythia 8 for the parton shower.

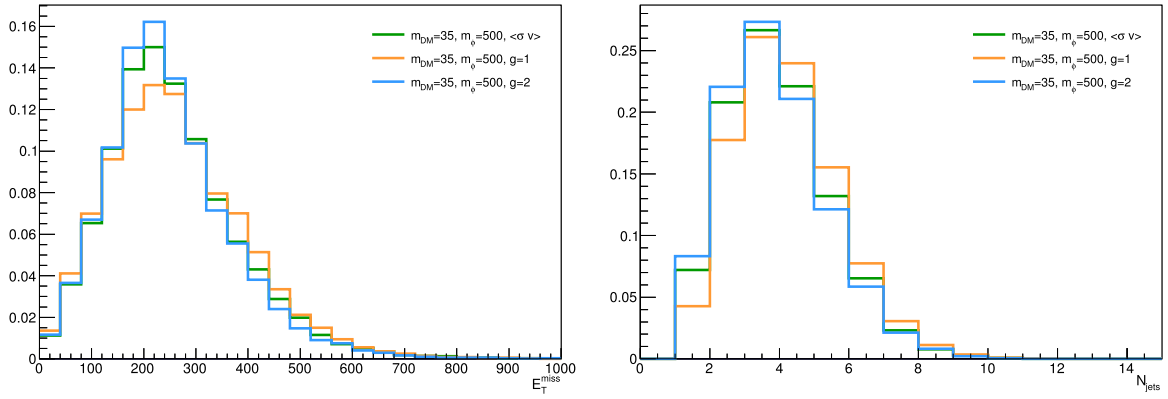

Fig. 33. $\not{E}_T$ (left) and jet multiplicity (right) for $m_\chi = 35$ GeV and $M_\Phi = 500$ GeV for varying couplings of $g = 1, 2$.

- off-shell mediator, when $q^2 \gg M^2_{\text{med}}$ leading to suppressed cross sections,
- on-shell mediator, when $q^2 \sim M^2_{\text{med}}$ leading to enhanced cross sections,
- effective field theory (EFT) limit when $q^2 \ll M^2_{\text{med}}$.

In the case of the off-shell mediator and the EFT limit, the first and second term in the propagator dominate, respectively, which reduces the dependence on the mediator width. Therefore, in these cases one can approximate the cross section as

$$\sigma \propto g_q^2 g_\chi^2. \tag{17}$$

The on-shell regime is the most interesting one as it gives the best chances for a discovery at the LHC given the cross section enhancement. The propagator term with the width cannot be neglected in this case and, in the narrow width approximation which requires $\Gamma \ll M_{\text{med}}$ (this is not necessarily the case in the benchmarks considered in the scans), one can integrate

$$\int \frac{ds}{(s - M^2_{\text{med}})^2 + M^2_{\text{med}}\Gamma^2} = \frac{\pi}{M_{\text{med}}\Gamma} \tag{18}$$

which further implies the cross section scaling

$$\sigma \propto \frac{g_q^2 g_\chi^2}{\Gamma}. \tag{19}$$

The narrow width approximation is important here as it ensures an integration over parton distribution functions (PDFs) can be neglected. In other words, it is assumed the integrand in Eq. (18) is non-zero only for a small region of s, such that the PDFs can be taken to be constant in this range. By simplifying the dependence of the minimal width on the couplings as $\Gamma \sim g_q^2 + g_\chi^2$, one can approximate this scaling rule in the extreme cases as follows

$$\sigma \propto \frac{g_q^2 g_\chi^2}{g_q^2 + g_\chi^2} \xrightarrow{g_q \ll g_\chi} g_q^2 \tag{20}$$

$$\sigma \propto \frac{g_q^2 g_\chi^2}{g_q^2 + g_\chi^2} \xrightarrow{g_q \gg g_\chi} g_\chi^2 \,. \tag{21}$$

However, it is important to keep in mind that this formula omits color and multiplicity factors as well as possible Yukawa suppression, and there is no simple scaling rule for how the cross section changes with the DM mass and the mediator mass, or for mediators with a large width, because PDFs matter in such cases as well. Therefore, the scaling procedure outlined above is expected to work only for fixed masses and fixed mediator width, assuming the narrow width approximation applies.

Fig. 34 shows the minimal width over the mediator mass in the g_q–g_χ plane for vector and scalar mediators for $M_{\text{med}} = 100$ GeV and 1000 GeV, taking $m_\chi = 10$ GeV. The individual colors indicate the lines of constant width, along which the cross section scaling may work for narrow mediators. The limiting case $\Gamma_{\text{min}} = M_{\text{med}}$ defines the upper values of the couplings below which the narrow width approximation can be considered and provides more stringent constraint than the perturbative limit $g_q = g_\chi = 4\pi$. For vector and axial-vector mediators, the minimal width is predominantly defined by g_q due to the number of quark flavors and the color factor. On the contrary, both the SM and DM partial width have comparable contributions in case of scalar and pseudo-scalar mediators if the top quark channel is open ($M_{\text{med}} > 2m_t$). However, mostly g_χ defines the minimal width for $M_{\text{med}} < 2m_t$ due to the Yukawa-suppressed light quark couplings.

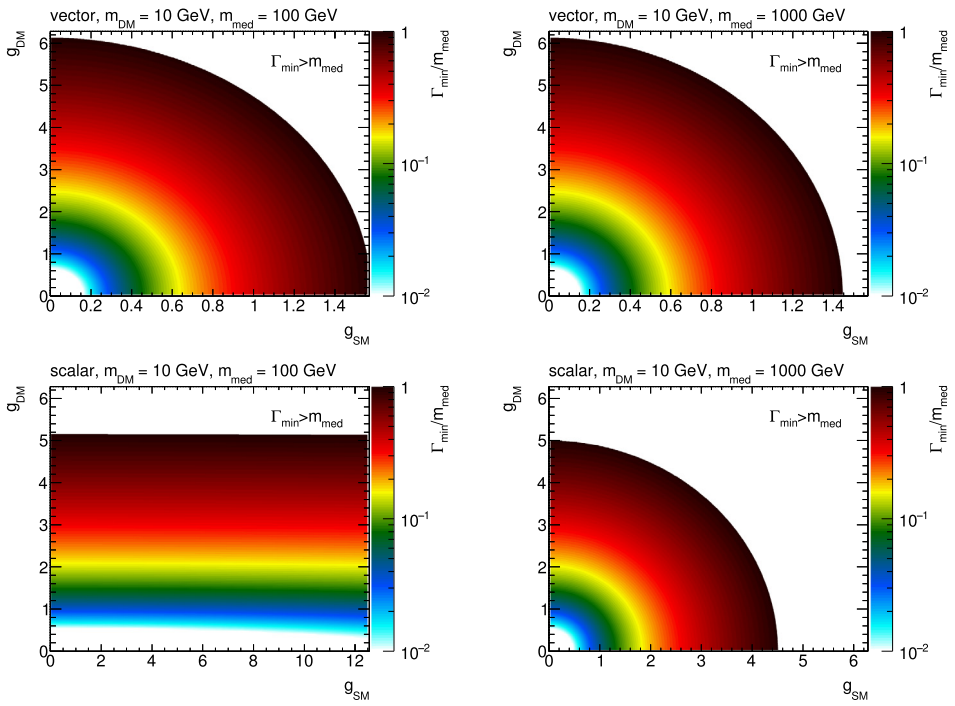

Fig. 34. Minimal width over the mediator mass for vector (top) and scalar (bottom) mediators as a function of the individual couplings g_q and g_χ, assuming $M_{med} = 100$ GeV (left) and $M_{med} = 1$ TeV (right). $m_\chi = 10$ GeV is considered in all cases. Only the cases with $\Gamma_{min} < M_{med}$ are shown.

The performance of the cross section scaling is demonstrated in Fig. 35 where two mass points $M_{med} = 100$ GeV and 1 TeV with $m_\chi = 10$ GeV are chosen and rescaled from the starting point $g_q = g_\chi = 1$ according to Eq. (19) to populate the whole g_q–g_χ plane. This means the width is not kept constant in this test and this is done in purpose in order to point out deviations from the scaling when the width is altered. For each mass point, the rescaled cross section is compared to the generator cross section and the ratio of the two is plotted. For the given choice of the mass points, the scaling seems to work approximately within the precision of $\sim$ 20% in the region where $\Gamma_{min} < M_{med}$. Constant colors indicate the lines along which the cross section scaling works precisely and there is a remarkable resemblance of the patterns shown in the plots of the mediator width. To prove the scaling along the lines of constant width works, one such line is chosen in Fig. 36 for a scalar mediator, defined by $M_{med} = 300$ GeV, $m_\chi = 100$ GeV, $g_q = g_\chi = 1$, and the rescaled and generated cross sections are found to agree within 3%.

2.5.1. Proposed parameter grid for cross-section scaling

We propose to deliver collider results in the g_q–g_χ plane using the following prescription, to ease reinterpretation through cross-section scaling:

- Since the shapes of kinematic quantities do not change for different couplings, use the acceptance and efficiency for the available $m_\chi = 50$ GeV, $M_{med} = 300$ GeV grid point from the M_{med}–m_χ plane for the scalar and pseudo-scalar mediator. In case of the vector and axial-vector mediator, use the grid point $m_\chi = 150$ GeV, $M_{med} = 1$ TeV.
- Generate additional samples in order to get generator cross sections only. For scalar and pseudo-scalar mediator, choose $m_\chi = 50$ GeV, $M_{med} = 300$ GeV with the following values for $g_q = g_\chi$: 0.1, 1, 2, 3. For vector and axial vector mediator, choose $m_\chi = 150$ GeV, $M_{med} = 1$ TeV with the following values for $g_q = g_\chi$: 0.1, 0.25, 0.5, 0.75, 1, 1.25, 1.5. The upper values are defined by the minimal width reaching the mediator mass.
- Rescale the generator cross sections for on-shell resonance production along the lines of constant width in order to populate the whole g_q–g_χ plane in the region $\Gamma_{min} < M_{med}$. The scaling follows from Eq. (19) which for the constant width implies:

$$\sigma' = \sigma \times \frac{g_q'^2 g_\chi'^2}{g_q^2 g_\chi^2} \,. \tag{22}$$

2.5.2. Rescaling to different mediator width

In general it is also important to consider a larger mediator width than Γ_{min} in order to accommodate additional interactions of the mediator with the visible and hidden sector particles [41, 42]. If the narrow width approximation applies, the cross section scaling method described above can be used to reinterpret the results presented for the minimal width, since multiplying the width by factor n is equivalent to changing the coupling strength by factor $\sqrt{n}$, i.e.

$$\sigma(g_q, g_\chi, n\Gamma_{min}(g_q, g_\chi)) \propto \frac{g_q^2 g_\chi^2}{\Gamma_{min}(\sqrt{n}g_q, \sqrt{n}g_\chi)} \,. \tag{23}$$

The cross section for the sample with couplings g_q and g_χ and modified mediator width $\Gamma = n\Gamma_{min}$ can therefore be rescaled from a sample generated with the minimal width corresponding to the couplings scaled by $\sqrt{n}$ as described in the following formula.

$$\sigma(g_q, g_\chi, n\Gamma_{min}(g_q, g_\chi)) = \frac{1}{n^2}\sigma(\sqrt{n}g_q, \sqrt{n}g_\chi, \Gamma_{min}(\sqrt{n}g_q, \sqrt{n}g_\chi)) \tag{24}$$

The advantage of doing this is in the fact that no event selection and detector response needs to be simulated since the changes in couplings do not have an effect on the shapes of kinematic distributions.

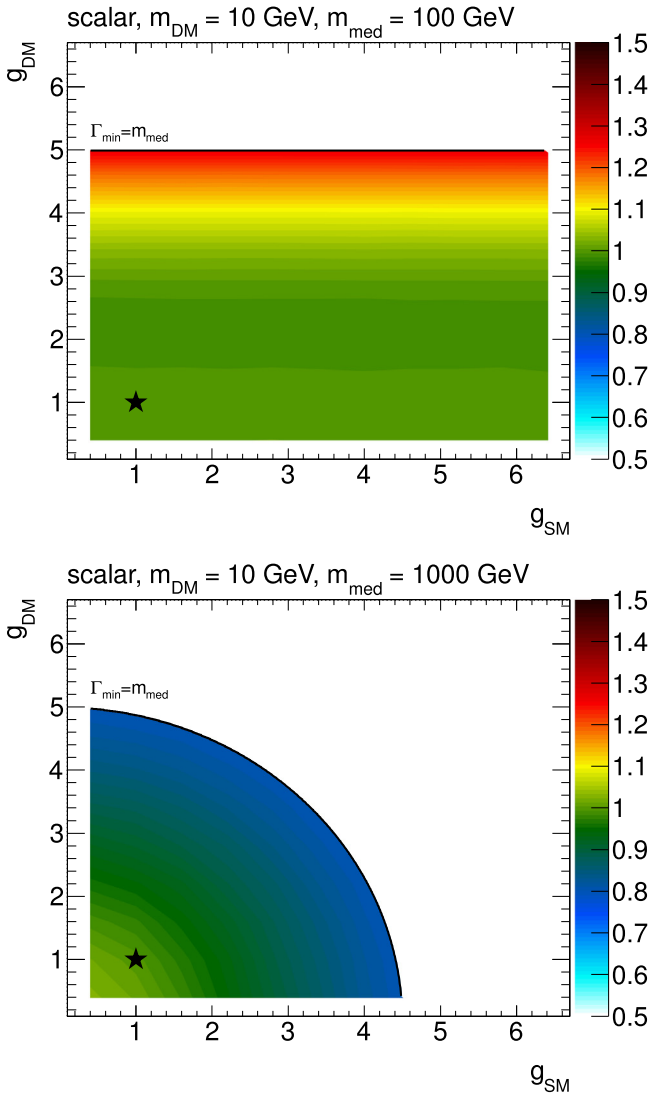

Fig. 35. Ratio of the rescaled and generated cross sections in the g_q–g_χ plane. The point at $g_q = g_\chi = 1$, taken as a reference for the rescaling, is denoted by a star symbol. Scalar model with $M_{med} = 100$ GeV (left) and 1 TeV (right) is plotted for $m_\chi = 10$ GeV. The limiting case $\Gamma_{min} = M_{med}$ is indicated by a black line and no results are shown beyond.

It should be noted again that this procedure is only useful when the narrow width approximation applies. Care must be taken to ensure that is the case. For example, in the vector and axial-vector cases, one quickly breaks this approximation even for small n.

Additional considerations for $t\bar{t}$ and $b\bar{b}+\not{E}_T$ signatures. The cross-section scaling considerations shown in Section 2.5 still apply for the reactions in the scalar and psuedoscalar models with explicit b and t quarks. Here we detail the specific studies done for the $t\bar{t}$ model.

Given that the kinematics are similar for all couplings $g \simeq 1$, we recommend to generate only samples with $g_\chi = g_q = 1$. It follows from this that these benchmark points should be a good approximation for non-unity couplings and for $g_\chi \neq g_q$, provided that the sample is rescaled to the appropriate cross section times branching ratio.

While the simple scaling function

$$\sigma' \times BR' = [\sigma \times BR] \times \left(\frac{g'_q}{g_q}\right)^2 \times \left(\frac{g'_\chi}{g_\chi}\right)^2 \times \frac{\Gamma}{\Gamma'} \quad (25)$$

is sufficient for a limited range of coupling values (see Fig. 37 for example), this scaling is only approximate (up to 20%) and relies on the narrow width approximation, ignoring PDFs effects.

3. Specific models for signatures with EW bosons

In this Section, we consider specific models with a photon, a W boson, a Z boson or a Higgs boson in the final state ($V+\not{E}_T$ signature), accompanied by DM particles that either couple directly to the boson or are mediated by a new particle. The common feature of those models is that they provide different kinematic distributions with respect to the models described in Section 2.

The models considered in this Section can be divided into two categories:

V-specific simplified models These models postulate direct couplings of new mediators to bosons, e.g. they couple the Higgs boson to a new vector or to a new scalar [48,97].

Models involving a SM singlet operator including a boson pair that couples to DM through a contact interaction Shown on the right-hand side of Fig. 38, these models allow for a contact interaction vertex that directly couples the boson to DM [45,97–99]. The models of this type included in this report are devoted to simplified models since UV completions for most of these operators proceed through loops and are not available to date. These models provide a benchmark to motivate signal regions that are unique to searches with EW final states and would otherwise not be studied. However, we recommend to use these models as placeholders and emphasize model-independent results especially in signal regions tailored to these models. Wherever results are interpreted in terms of these operators, a truncation procedure to ensure the validity of the EFT should be employed, as detailed in Section 5.

The following Sections describe the models within these categories, the chosen parameters for each of the benchmark models and the studies towards the choices of the parameters to be scanned.

3.1. Specific simplified models including EW bosons, tailored to Higgs+MET searches

Three benchmark simplified models [48,97] are recommended for Higgs+$\not{E}_T$ searches:

- A model where a vector mediator (Z'_B) is exchanged in the s-channel, radiates a Higgs boson, and decays into two DM particles (Fig. 39(a)). As in Section 2.1, we conservatively omit couplings of the Z'_B to leptons.
- A model where a scalar mediator S is emitted from the Higgs boson and decays to a pair of DM particles (Fig. 40).
- A model where a vector Z' is produced resonantly and decays into a Higgs boson plus an intermediate heavy pseudoscalar particle A^0, in turn decaying into two DM particles (Fig. 39(b)).

These models are kinematically distinct from one another, as shown in the comparison of the $\not{E}_T$ spectra in Fig. 41 for high and low masses of the pseudoscalar mediator. Fig. 41(a) shows the $\not{E}_T$ distribution for models with high mediator masses ($m_S = 1$ TeV, $m_{Z'} = 1$ TeV, $m_{A^0} = 1$ TeV) and DM mass of either 50 (Z'_B and

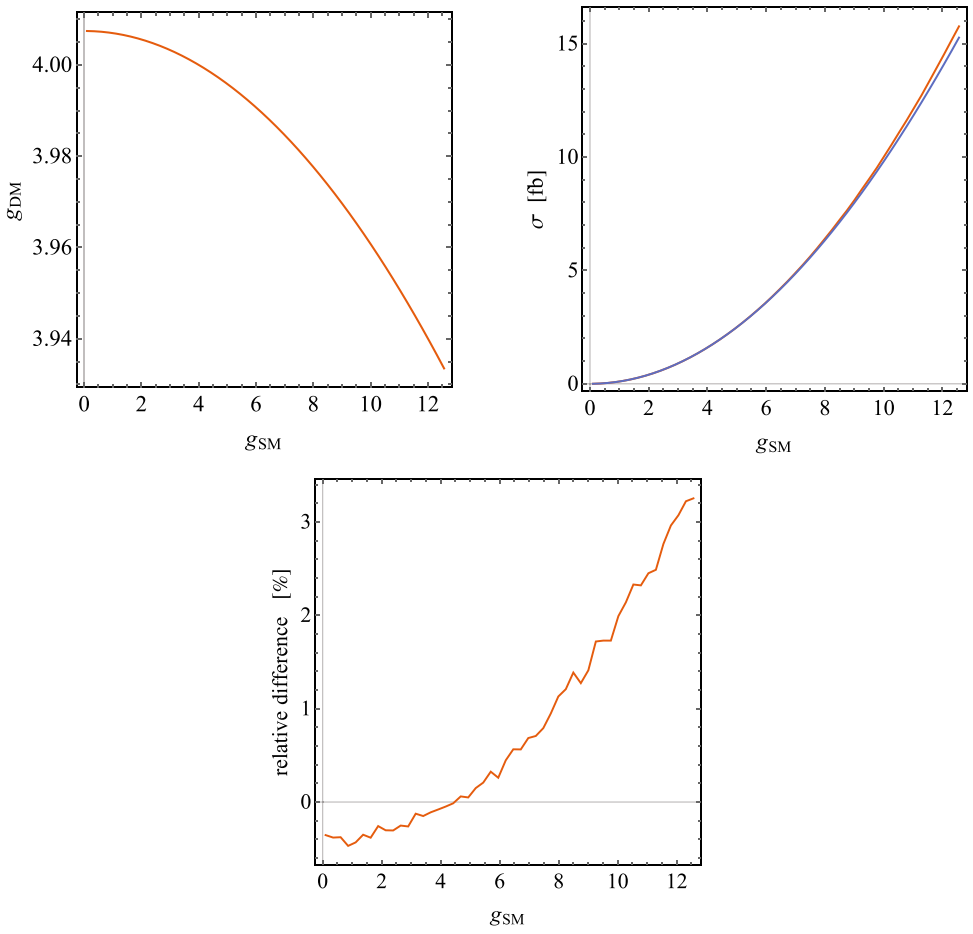

Fig. 36. Scaling along the lines of constant width. The line of constant width for $M_{\text{med}} = 300$ GeV and $m_\chi = 100$ GeV, intercepting $g_q = g_\chi = 4$ is shown on left. The generated and rescaled cross sections are compared in the middle, the corresponding ratio is shown on right.

A^0 models) or 65 GeV (scalar mediator model). Fig. 41(b) shows the $\not{E}_T$ distribution for models with low pseudoscalar mediator masses ($m_{Z'_B} = 100$ GeV, $m_{Z'} = 1$ TeV, $m_{A^0} = 100$ GeV) and DM mass of 1 TeV for all models.

Predictions for this class of models have been so far considered at LO+ Parton Shower (PS), even though they could be extended to NLO+PS in the near future. The studies in this Section have been performed using a model within MadGraph5_aMC@NLO v5.1.5.12, interfaced to Pythia 6 for the parton shower. The implementation details for these models are discussed in Section 4.2.1.

3.1.1. $\not{E}_T$ +Higgs from a baryonic Z'

The model shown in Fig. 39(a) postulates a new gauge boson Z' corresponding to a new $U(1)_B$ baryon number symmetry. The stable baryonic states included in this model are the DM candidate particles. The mass of the Z' boson is acquired through a baryonic Higgs h_B, which mixes with the SM Higgs boson.

The interactions between the Z', the quarks and the DM are described by the following Lagrangian:

$$\mathscr{L} = g_q \bar{q}\gamma^\mu q Z'_\mu + g_\chi \bar{\chi}\gamma^\mu \chi Z'_\mu. \tag{26}$$

The quark couplings g_q are fixed to be equal to one third of the gauge coupling g_B, while the DM coupling to the Z' are proportional to the baryon number and to the gauge coupling ($g_\chi = Bg_B$). No leptonic couplings of the Z' are allowed, thus evading dilepton constraints. After incorporating the mixing of the baryonic and SM Higgs bosons, this model is described by the following Lagrangian term at energies below $m_{Z'}$[10]:

$$\mathscr{L}_{\text{eff}} = -\frac{g_q g_\chi}{m^2_{Z'}} \bar{q}\gamma^\mu q \bar{\chi}\gamma_\mu \chi \left(1 + \frac{g_{hZ'Z'}}{m^2_{Z'}} h\right), \tag{27}$$

The first term of this equation is the standard DMV model in the large $M_{Z'}$ limit. This term can lead to a monojet signature, which can be also used to constrain this model. The second term describes the interaction between the Z' and the SM Higgs boson, via the coupling $g_{hZ'Z'} = \frac{m_{Z'} 2 \sin\theta}{v_B}$, where $\sin\theta$ is the mixing angle between the SM Higgs and the baryonic Higgs h_B, and v_B is the Baryonic Higgs vacuum expectation value.

In its most general form, this model can contribute to mono-Z signals due to the Z' mixing with the Z or photon. Note that EWSB and $U(1)_B$ breaking do not lead to this mixing at tree-level. Instead, kinetic mixing occurs between the $U(1)_Y$ and $U(1)_B$ gauge bosons due to the gauge invariant term $F^{\mu\nu}_Y F_{B\mu\nu}$. This mixing is a free parameter which we assume to be small in order to focus on the mono-Higgs signature. Mixing may also occur due to radiative corrections, however we choose to ignore this here as it is model dependent.

The predictions of the model depend upon the two additional parameters beyond an s-channel simplified model, namely the mixing angle between baryonic Higgs h_B and the SM-like Higgs boson $\sin\theta$ and the coupling of the mediator to SM-like Higgs

[10] The operator in Eq. (27) is an effective one, to highlight the two main terms. The full dimension-4 simplified model is used in the model for event generation.

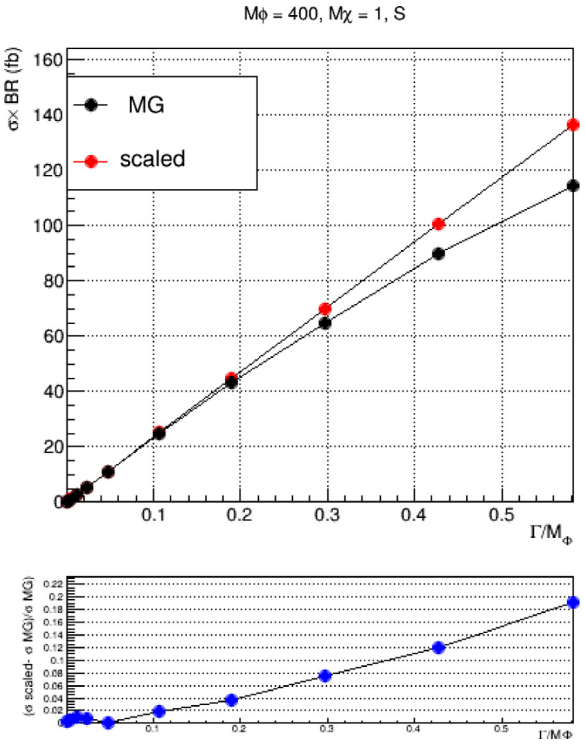

Fig. 37. An example comparing a simple cross section scaling versus the computation from the MadGraph5_aMC@NLO generator, for a scalar $t\bar{t}$+$\not{E}_T$ model with $m_\phi = 400$ GeV, $m_\chi = 1$ GeV and all couplings set to unity. In this example, the scaling relationship holds for Γ_ϕ/m_ϕ below 0.2, beyond which finite width effects become important and the simple scaling breaks down.

boson, $g_{hZ'Z'}$. Thus, a full model is specified by:

$$\left\{M_{\text{med}},\ m_\chi,\ g_\chi,\ g_{\text{q}},\ \sin\theta,\ g_{hZ'Z'}\right\}. \tag{28}$$

Parameter scan. The width of the Z' mediator is calculated using all possible decays to SM particles (quarks) and to pairs of DM particles if kinematically allowed as in the DMV model.

The dependence of the missing transverse momentum ($\not{E}_T$) on the model parameters is studied by varying the parameters one at a time. The variation of parameters other than M_{med} and m_χ does not result in significant variations of the $\not{E}_T$ spectrum, as shown in Fig. 42. Fig. 43 shows that for an on-shell mediator, varying m_χ with the other parameters fixed does not affect the $\not{E}_T$ distribution, while the distribution broadens significantly in the case of an off-shell mediator. For this reason, the same grid in M_{med}, m_χ as for the vector mediator of the jet+$\not{E}_T$ search (Table 1)

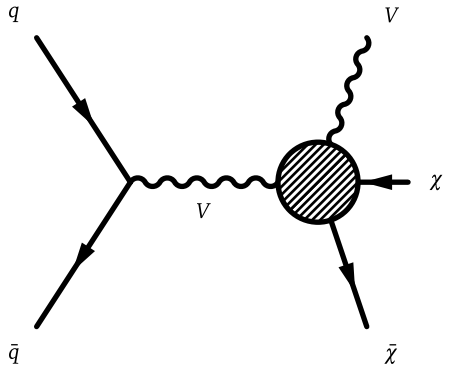

Fig. 38. Sketch of benchmark models including a contact interaction for V+MET searches.
Source: Adapted from [100].

is chosen as a starting point. The coupling $g_{hZ'Z'}$, along with g_{q} and g_χ, are subject to perturbativity bounds:

$$g_{\text{q}}, g_\chi < 4\pi,$$

and

$$g_{hZ'Z'} < \sqrt{4\pi}\, m_{Z'} \sin\theta.$$

The value $g_{hZ'Z'}/m_{Z'} = 1$ is chosen as a benchmark value for the generation of Monte Carlo samples since it maximizes the cross section (as shown in the following paragraph) without violating the bounds. The mediator-DM coupling g_χ is fixed to 1, and the mediator-quark g_q coupling is fixed to 1/3. The kinematic distributions do not change as a function of these parameters, so results for other values of $g_{hZ'Z'}/m_{Z'}$, g_χ and g_{q} can be obtained through rescaling by the appropriate cross sections.

Figs. 44 and 45 show the kinematic distributions for the two leading jets in the $H \to \bar{b}b$ decay channel, for two values of the mediator mass and varying the DM mass.

Experimentalists should perform further studies, beyond those studies performed for the forum, to estimate the reach of the analysis with respect to all points in the grid and therefore decide on a smaller set of grid points to be generated.

3.1.2. $\not{E}_T$ +Higgs from a scalar mediator

A real scalar singlet S coupling to DM can be introduced as a portal between SM and the dark sector through the Higgs field. The most general scalar potential is detailed in Ref. [101], including terms that break $\mathbb{Z}_2$. The $\mathbb{Z}_2$ symmetry, which causes the new scalar to also be a DM candidate, is not covered in this report, but follows Ref. [48] introducing an additional coupling to

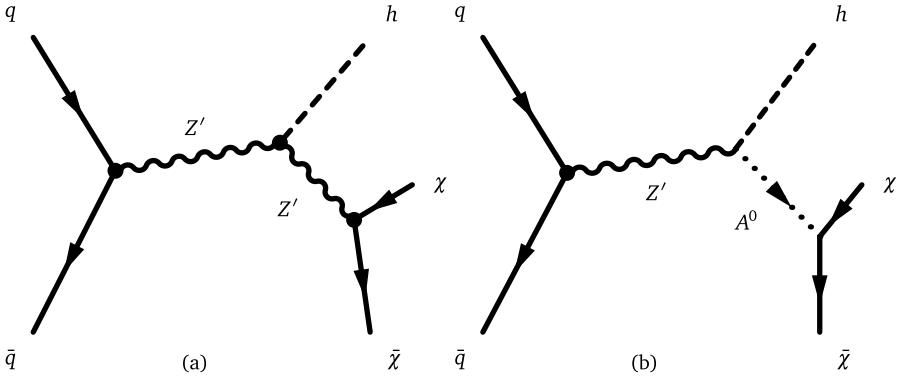

Fig. 39. Examples of Feynman diagrams leading to Higgs+$\not{E}_T$ events: (a) a model with a vector mediator (Z') coupling with DM and with the Higgs boson h, and (b) a 2HDM model with a new invisibly decaying pseudoscalar A^0 from the decay of an on-shell resonance Z' giving rise to a Higgs+$\not{E}_T$ signature .

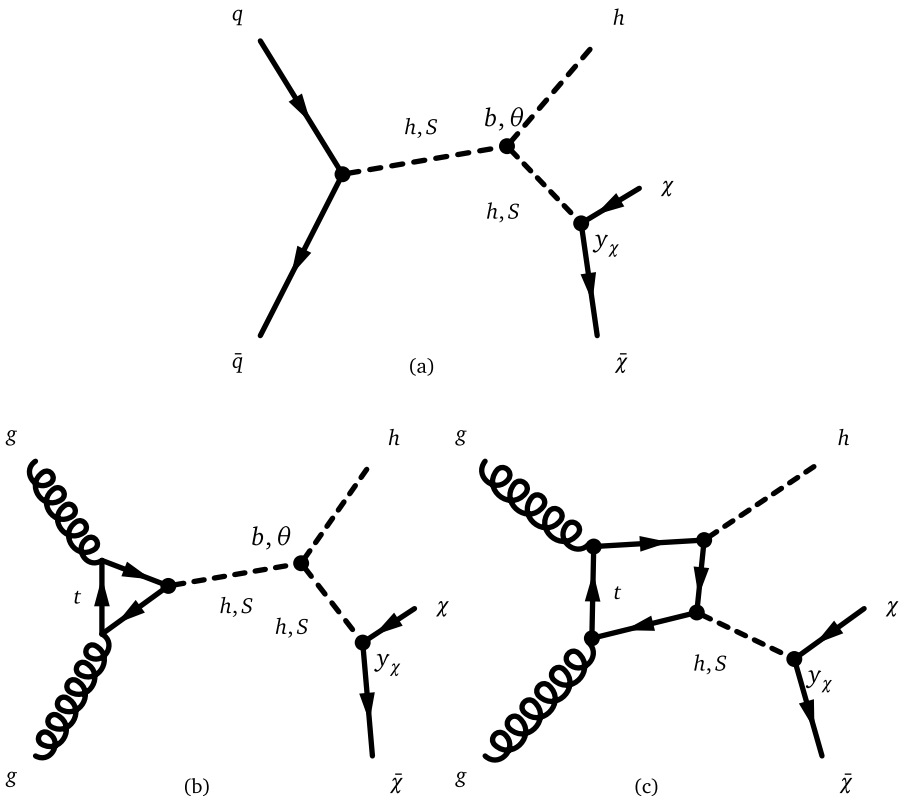

Fig. 40. Examples of Feynman diagrams leading to Higgs+$\not{E}_T$ events for a model with a scalar mediator (S) coupling with DM and with the Higgs boson h.

DM that breaks $\mathbb{Z}_2$ and leads to a new invisible decay of S. For this reason, no symmetry is broken and no new interactions arise, so there is no dependence on the vacuum expectation value of S: a shift in the field leads to a redefinition of the model couplings. The new scalar S mixes with the SM Higgs boson, and couples to DM through a Yukawa term y_χ. The relevant terms in the scalar potential are:

$$V \supset a|H|^2 S + b|H|^2 S^2 + \lambda_h |H|^4$$
$$\longrightarrow \tfrac{1}{2} a(h+v)^2 S + \tfrac{1}{2} b(h+v)^2 S^2 + \frac{\lambda_h}{4}(h+v)^4, \quad (29)$$

where a, b are new physics couplings and λ_h is the Higgs quartic coupling.

The additional Lagrangian terms for this model are:

$$\mathscr{L} \supset -y_\chi \bar{\chi}\chi(\cos\theta\, S - \sin\theta\, h) - \frac{m_q}{v}\bar{q}q(\cos\theta\, h + \sin\theta\, S) \quad (30)$$

where θ is the mixing angle between the Higgs boson and the new scalar.

Mono-Higgs signals in this second model arise through processes shown in Fig. 40 (a,b), or through the radiation of a Higgs boson from the t quark in the production loop, in Fig. 40(c). The first two processes depend on the h^2S and hS^2 cubic terms in Eq. (29). At leading order in $\sin\theta$, these terms are:

$$V_{\text{cubic}} \approx \frac{\sin\theta}{v}(2m_h^2 + m_S^2)h^2 S + b\, v\, h\, S^2 + \cdots, \quad (31)$$

with a and λ_h expressed in terms of $\sin\theta$ and m_h^2, respectively. At leading order of $\sin\theta$, the h^2S term is fixed once the mass eigenvalues m_h, m_S and mixing angle are specified. The $h\,S^2$ term is not fixed and remains a free parameter of the model, depending on the new physics coupling b.

This model also has mono-X signatures through h/S mixing. This model is related to the scalar model discussed in Section 2.2 in the case of $m_S \gg m_h$ or $m_h \gg m_S$ and M_{med} equal to the lighter of the two masses, albeit with different mono-Higgs signatures due to the hS^2 vertex.

Parameter scan. The model is described by five parameters:

1. the Yukawa coupling of heavy scalar to dark matter, g_χ (also referred to as y_χ)
2. the mixing angle between heavy scalar and SM-like Higgs boson, $\sin\theta$;
3. the new physics coupling, b;
4. mass of heavy scalar, m_S, also termed M_{med};
5. mass of DM. m_χ;

The mixing angle is constrained from current Higgs data to satisfy $\cos\theta = 1$ within 10% and therefore $\sin\theta \lesssim 0.4$. This provides a starting point for the parameter scan in this model: we recommend to set $\sin\theta = 0.3$.

Fig. 47 shows that the kinematics does not depend on the value of this angle, and results for different values can be obtained via rescaling the results for this mixing angle according to the relevant cross-section. It can also be observed from Figs. 46 and 48 that the kinematics of this model follows that of the equivalent jet+$\not{E}_T$ model: only small changes are observed in the on-shell region, while the relevant distributions diverge when the mediator is off-shell. For this reason, the same grid in M_{med}, m_χ as for the scalar mediator of the jet+$\not{E}_T$ search (Table 5) is chosen as a starting point. The Yukawa coupling to DM y_{DM} is set to 1, the new physics coupling between scalar and SM Higgs $b = 3$. Results for other values can be obtained via a rescaling of the results for these parameters.

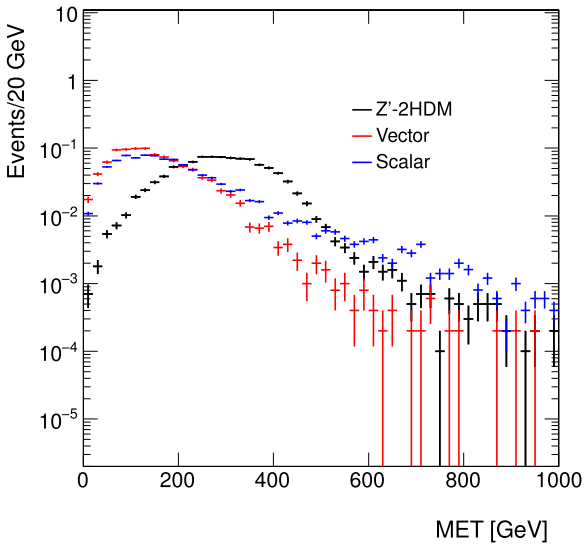

(a) High mediator mass

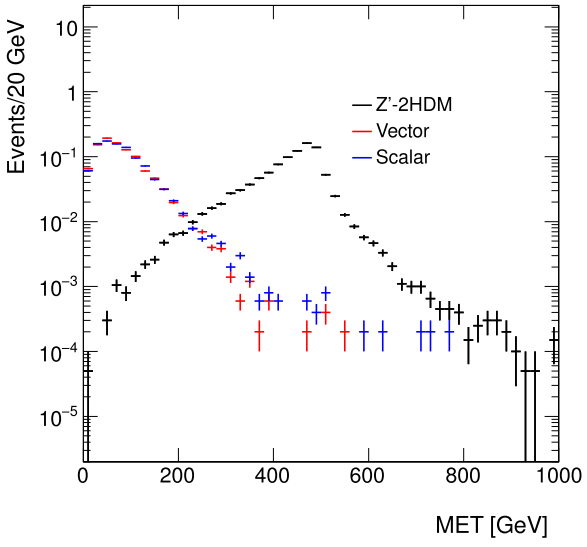

(b) Low mediator mass

Fig. 41. Comparison of the missing transverse momentum distributions at generator level in different simplified models leading to a Higgs+$\not{E}_T$ signature. The model parameter settings are detailed in the text. The figures in this Section have been obtained using LO UFO models within MadGraph5_aMC@NLO v2.2.3, interfaced to Pythia 8 for the parton shower.

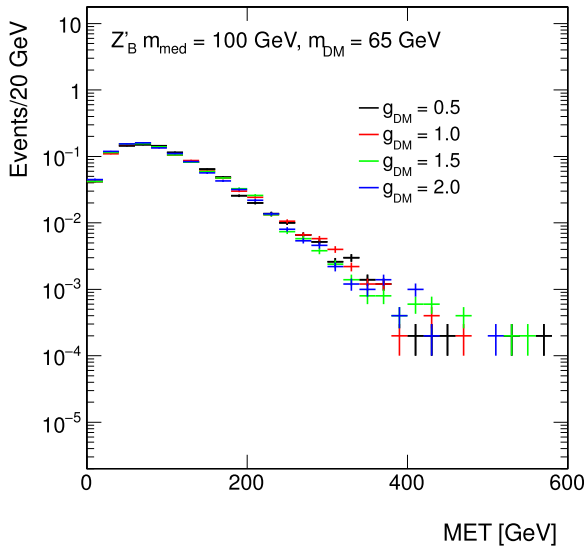

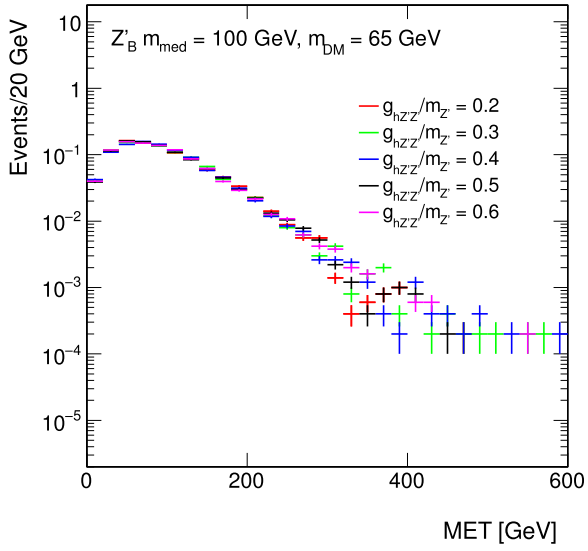

Fig. 42. Missing transverse momentum distributions at generator level in the vector mediator scenario for different values of: the mediator-DM coupling g_χ (left), and the coupling between the mediator and the SM-like Higgs boson, scaled by the mediator mass, $g_{hZ'Z'}/m_{Z'}$ (right).

Figs. 49 and 50 show the kinematic distributions for the two leading jets in the $H \to \bar{b}b$ decay channel, for two values of the mediator mass and varying the DM mass.

3.1.3. Higgs+$\not{E}_T$ signal from 2HDM model with a Z' and a new pseudoscalar

In this simplified model [97], a new Z' resonance decays to a Higgs boson h plus a heavy pseudoscalar state A^0 in the 2HDM framework, which in turn decays to a DM pair. This model is represented in the diagram in Fig. 39(b).

The motivation for coupling the DM to the pseudoscalar is that DM coupling to a Higgs or Z' boson is generically constrained by other signal channels and direct detection. A reason to consider this model is that it has different kinematics due to the on-shell Z' production, where for heavy Z' masses the $\not{E}_T$ and p_T spectra are much harder. This model can satisfy electroweak precision tests and constraints from dijet resonance searches, and still give a potentially observable Higgs+$\not{E}_T$ signal.

The model comprises of two doublets, where Φ_u couples to up-type quarks and Φ_d couples to down-type quarks and leptons:

$$-\mathscr{L} \supset y_u Q \tilde{\Phi}_u \bar{u} + y_d Q \Phi_d \bar{d} + y_e L \Phi_d \bar{e} + \text{h.c.} \tag{32}$$

After electroweak symmetry breaking, the Higgs doublets attain vacuum expectation values v_u and v_d, and in unitary gauge the doublets are parameterized as

$$\Phi_d = \frac{1}{\sqrt{2}} \begin{pmatrix} -\sin\beta\ H^+ \\ v_d - \sin\alpha\ h + \cos\alpha\ H - i \sin\beta\ A^0 \end{pmatrix} \quad ,$$
$$\Phi_u = \frac{1}{\sqrt{2}} \begin{pmatrix} \cos\beta\ H^+ \\ v_u + \cos\alpha\ h + \sin\alpha\ H + i \cos\beta\ A^0 \end{pmatrix} \tag{33}$$

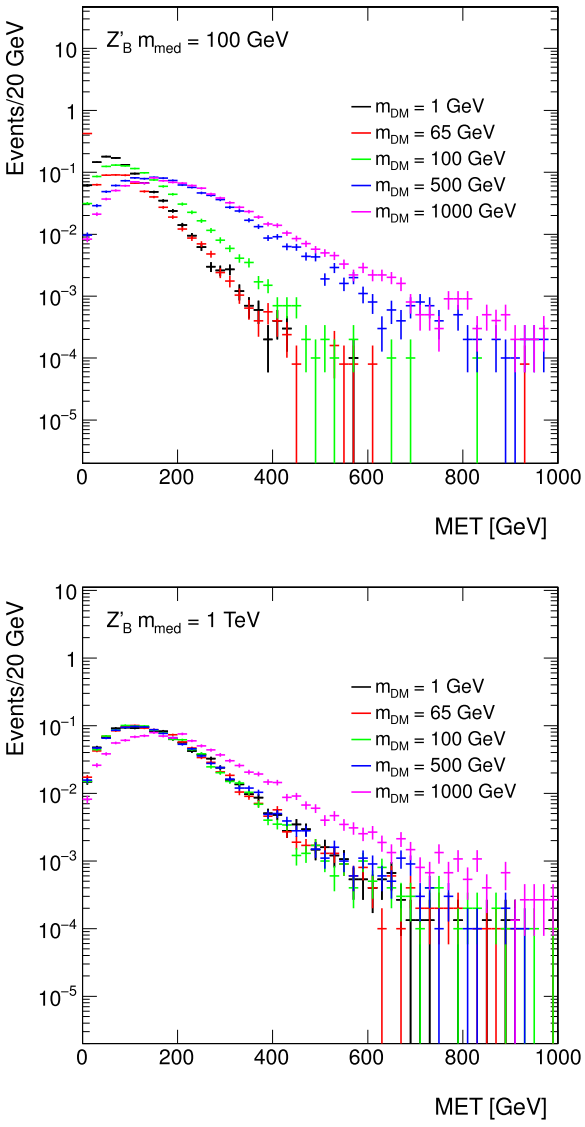

Fig. 43. Missing transverse momentum distributions at generator level in the vector mediator scenario: for different values of the DM mass m_χ and a mediator mass of M_{med}= 100 GeV (left) and M_{med}= 1 TeV (right).

where h, H are neutral CP-even scalars, $H^\pm$ is a charged scalar, and A^0 is a neutral CP-odd scalar. In this framework, $\tan\beta \equiv v_u/v_d$, and α is the mixing angle that diagonalizes the $h-H$ mass squared matrix. This model also contains an additional scalar singlet ϕ that leads to spontaneous symmetry breaking. We take $\alpha = \beta - \pi/2$, in the alignment limit where h has SM-like couplings to fermions and gauge bosons as per Ref. [102], and $\tan\beta \geq 0.3$ as implied from the perturbativity of the top Yukawa coupling. The Higgs vacuum expectation values lead to $Z-Z'$ mass mixing, with a small mixing parameter given by

$$\epsilon \equiv \frac{1}{M_{Z'}^2 - M_Z^2}\frac{g g_z}{2\cos\theta_w}(z_d v_d^2 + z_u v_u^2) = \frac{(M_Z^0)^2}{M_{Z'}^2 - M_Z^2}\frac{2 g_z \cos\theta_w}{g} z_u \sin^2\beta, \quad (34)$$

where z_i are the Z' charges of the two Higgs doublets, and g and g_z related to the mass-squared values in absence of mixing $(M_Z^0)^2 = g^2(v_d^2 + v_u^2)/(4\cos^2\theta_w)$ and $(M_{Z'}^0)^2 = g_z^2(z_d^2 v_d^2 + z_u^2 v_u^2 + z_\Phi^2 v_\Phi^2)$.

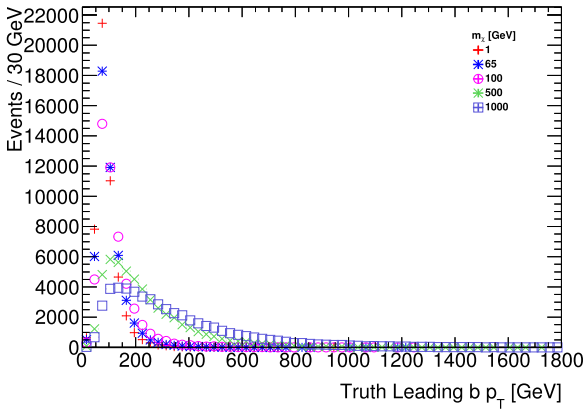

(a) Leading b—jet transverse momentum

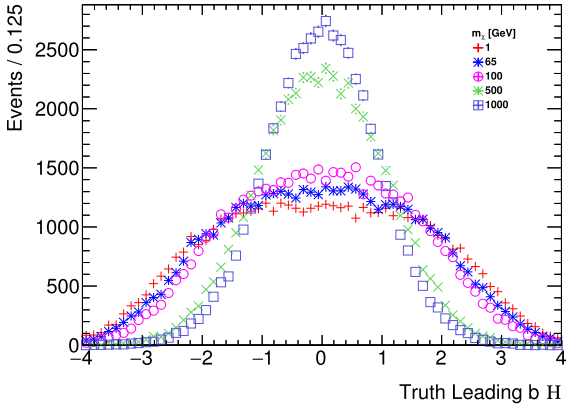

(b) Leading b—jet pseudorapidity

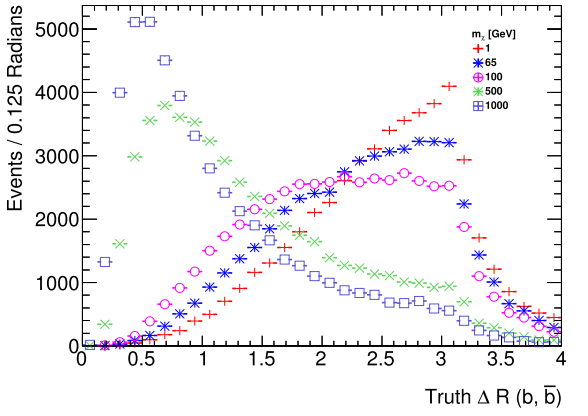

(c) Angular distance between the two leading b—jets

Fig. 44. Comparison of the kinematic distributions for the two leading b—jets (from the Higgs decay) in the vector Z' simplified model, when fixing the Z' mass to 100 GeV and varying the DM mass.

The production cross section for this model scales as $(g_z)^2$, as the decay width for this process to leading order in ϵ (Eq. (34)) is

$$\Gamma_{Z'\to hA^0} = (g_z \sin\beta\cos\beta)^2 \frac{|p|}{24\pi}\frac{|p|^2}{M_{Z'}^2}. \quad (35)$$

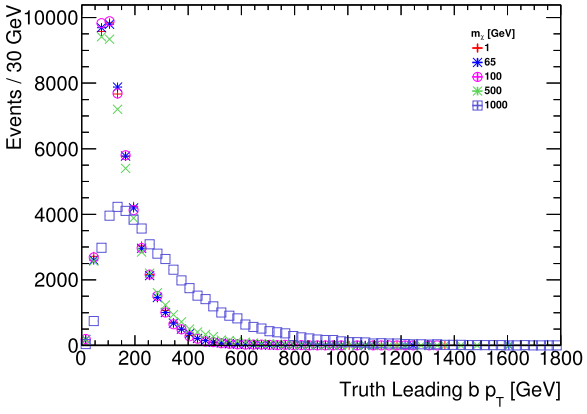

(a) Leading b—jet transverse momentum

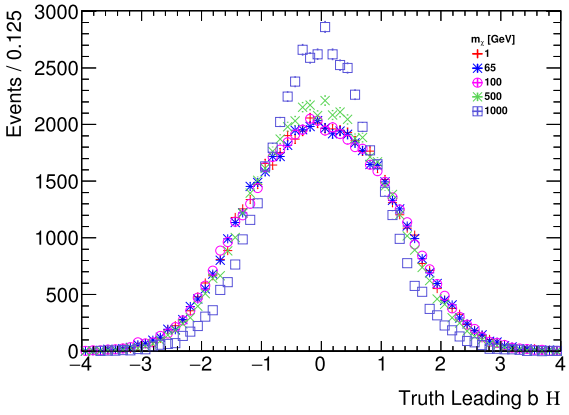

(b) Leading b—jet pseudorapidity

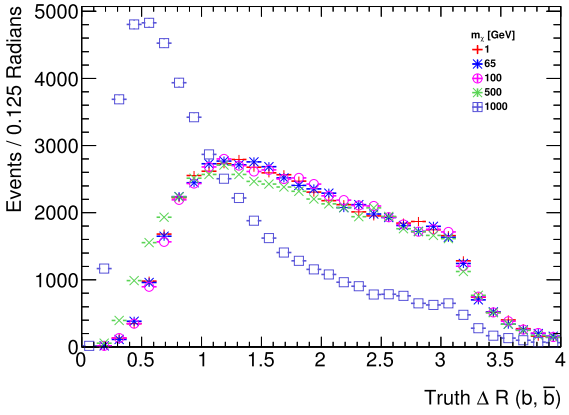

(c) Angular separation of the two leading b-jets

Fig. 45. Comparison of the kinematic distributions for the two leading jets from the Higgs decay in the vector Z' simplified model, when fixing the Z' mass to 1000 GeV and varying the DM mass.

where the center of mass momentum for the decay products is

$$|p| = \frac{1}{2M_{Z'}}\sqrt{(M_{Z'}^2 - (m_h + m_{A^0})^2)(M_{Z'}^2 - (m_h - m_{A^0})^2)}. \quad (36)$$

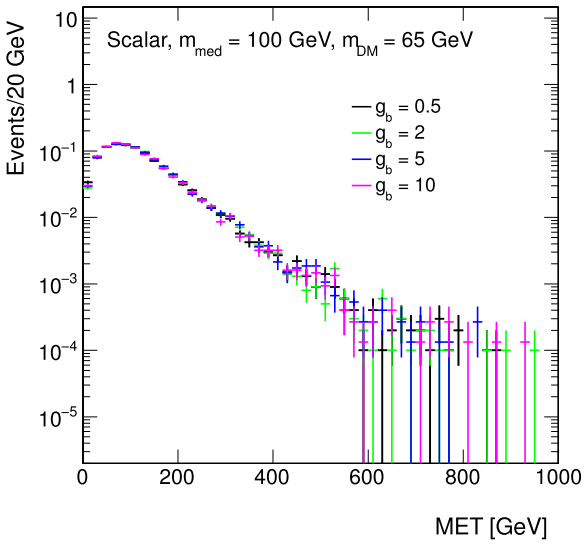

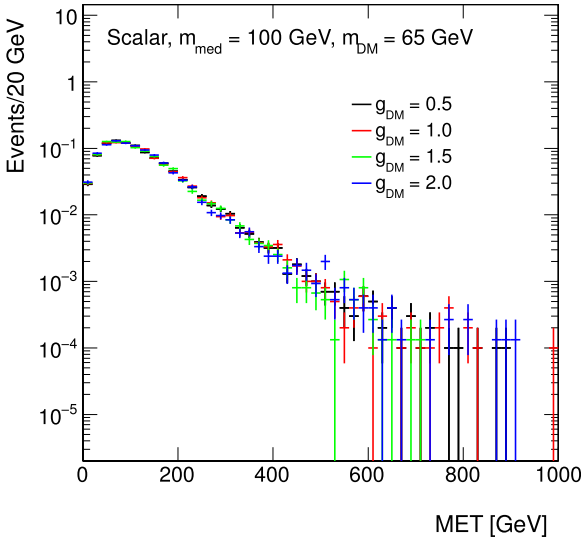

Fig. 46. Missing transverse momentum distributions at generator level in the scalar mediator scenario, for different values of: the new physics coupling g_b (left), and the mediator-DM coupling g_χ (right).

The Z' can also decay to Zh, leading to the same signature if the Z decays invisibly. The partial width for this decay is:

$$\Gamma_{Z'\to hZ} = (g_z \sin\beta^2)^2 \frac{|p|}{24\pi}\left(\frac{|p|^2}{M_{Z'}^2} + 3\frac{M_Z^2}{M_{Z'}^2}\right). \quad (37)$$

We recommend to generate these two decays separately and combine them at a later stage.

Parameter scan. The model is described by five parameters:

- the pseudoscalar mass M_{A^0},
- the DM mass m_χ,
- the Z' mass, $M_{Z'}$,
- $\tan\beta(\equiv v_u/v_d)$,
- the Z' coupling strength g_z.

To study the signal production and kinematic dependencies on these parameters, we produced signal samples varying each of the five parameters through MadGraph5_aMC@NLO for the matrix element, Pythia 8 for the parton shower, and DELPHES [103] for a parameterized detector-level simulation.

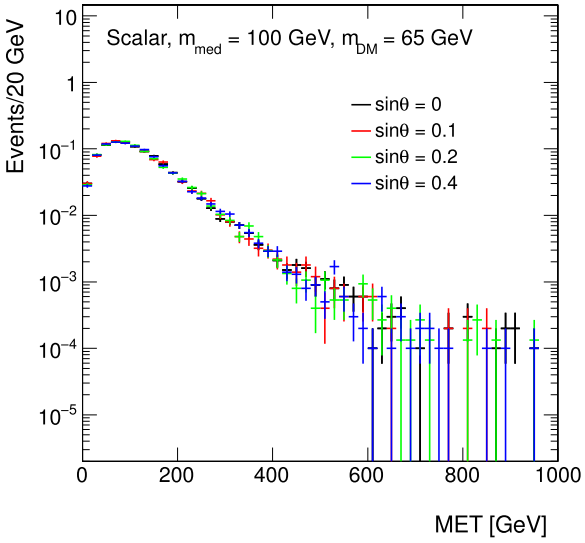

Fig. 47. Missing transverse momentum distributions at generator level in the scalar mediator scenario: for different values of the mixing angle $\sin\theta$.

As seen in Fig. 51, variations of $\tan\beta$ does not lead to any kinematic difference and the production cross section simply scales as a function of $\tan\beta$. Hence we recommend to fix $\tan\beta$ to unity in the signal generation.

Similarly, variations of g_z do not lead to any kinematic changes. The value of g_z for a given $M_{Z'}$ and $\tan\beta$ can be set according to the maximum value allowed by electroweak global fits and dijet constraints, as described in [97]. Since this parameter does not influence the kinematics, we leave it up to individual analyses to decide whether they generate benchmark points only according to these external constraints.

Since the DM pair are produced as a result of the decay of A^0, there are minimal kinematic changes when varying m_χ as long as $m_\chi < M_{A^0}/2$ so that A^0 production is on-shell, as shown in Figs. 52 and 53 (before detector simulation).

We recommend to produce signal events for a fixed $g_z = 0.8$, $\tan\beta = 1$ and $m_\chi = 100$ GeV. For these values, we scan the 2-D parameter space of $M_{Z'}, M_{A^0}$ with $M_{Z'} = 600, 800, 1000, 1200, 1400$ GeV, and $M_{A^0} = 300, 400, 500, 600, 700, 800$ GeV with $M_{A^0} < M_{Z'} - m_h$, for a total of 24 points. The choice of scan is justified by the sensitivity study in [97]: the expected LHC sensitivity for Run-2 is up to $M_{Z'} \sim 1.5$ TeV. For the parameter scan, the DM mass is fixed to 100 GeV. For two $M_{Z'}, M_{A^0}$ value sets, we vary the DM mass to obtain sample cross section for rescaling results. All LO cross sections for the various parameter scan points are reported on HEPData. The parameter scan excludes the off-shell region, as the cross-sections are suppressed and the LHC would not have any sensitivity to these benchmark points in early data.

The kinematic distributions with varying $M_{Z'}$ for fixed M_{A^0} are shown in Fig. 54, while the dependency on M_{A^0} is shown in Fig. 55.

This model also allows for an additional source of Higgs plus $\not{E}_T$ signal with a similar kinematics (Fig. 56, shown with detector simulation samples) to the signal process from the decay of $Z' \to hZ$, where the Z decays invisibly. The partial decay width for the Z' is:

$$\Gamma_{Z'\to hZ} = (g_z \cos\alpha \sin\beta)^2 \frac{|p|}{24\pi}\left(\frac{|p|^2}{M_{Z'}^2} + 3\frac{M_Z^2}{M_{Z'}^2}\right). \quad (38)$$

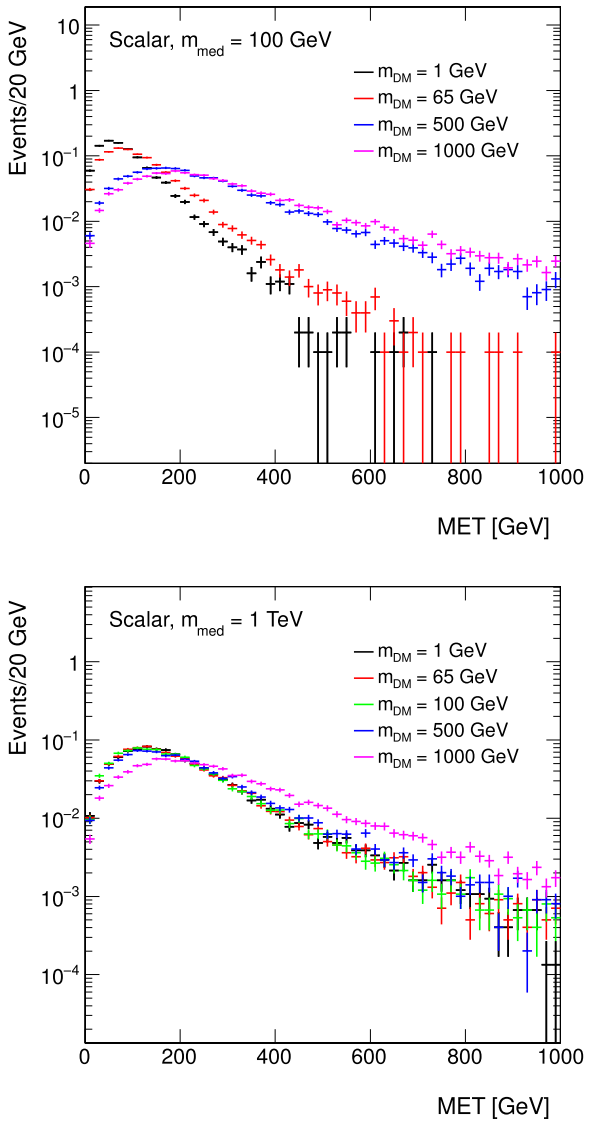

Fig. 48. Missing transverse momentum distributions at generator level in the scalar mediator scenario: for different values of the DM mass m_χ and a mediator mass of $M_{\text{med}} = 100$ GeV (left) and $M_{\text{med}} = 1$ TeV (right).

The values for the Z' masses scanned for those samples should follow those of the previous samples, namely values of $M_{Z'} = 600, 800, 1000, 1200, 1400$ GeV. This signal process has no M_A dependence.

3.2. EFT models with direct DM-boson couplings

The EFT operators considered in this section do not have an implementation of a simplified model completion for Dirac fermion Dark Matter available to date. They provide kinematic distributions that are unique to mono-boson signatures, and that in most cases are not reproduced by an equivalent simplified model.[11]

A complete list of effective operators with direct DM/boson couplings for Dirac DM, up to dimension 7, can be found in [45, 98,99]. Higher dimensional operators, up to dimension 8, leading

[11] Wherever this is the case, for practical reasons one can only generation a simplified model result in the limiting EFT case, as the results can be rescaled and reinterpreted.

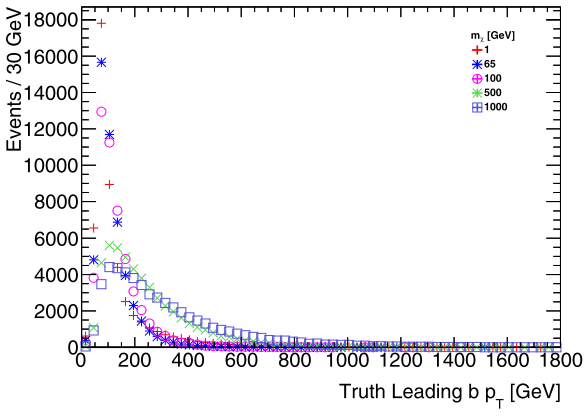

(a) Leading b—jet transverse momentum

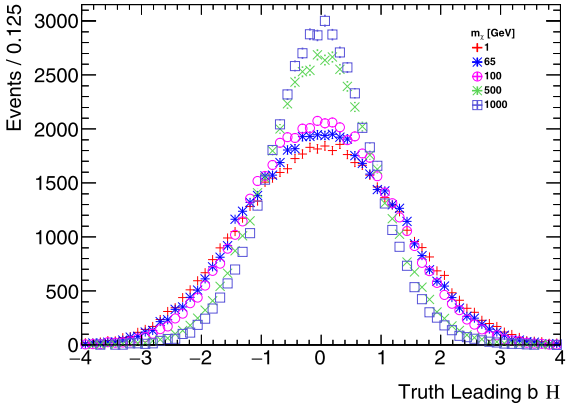

(b) Leading b—jet pseudorapidity

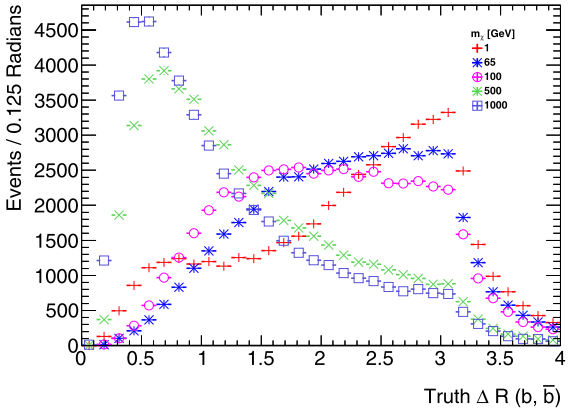

(c) Angular distance between the two leading b—jets

Fig. 49. Comparison of the kinematic distributions for the two leading jets from the Higgs decay in the scalar simplified model, when fixing the new scalar mass to 100 GeV and varying the DM mass.

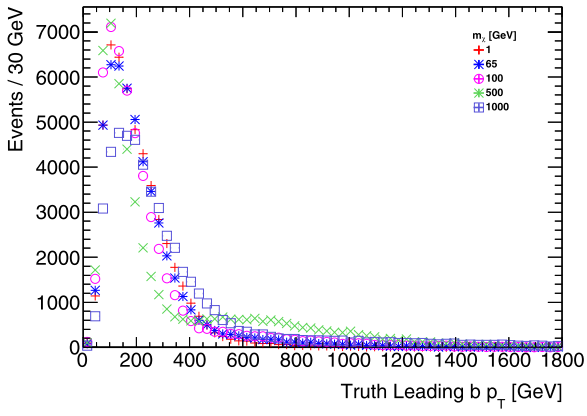

(a) Leading b—jet transverse momentum

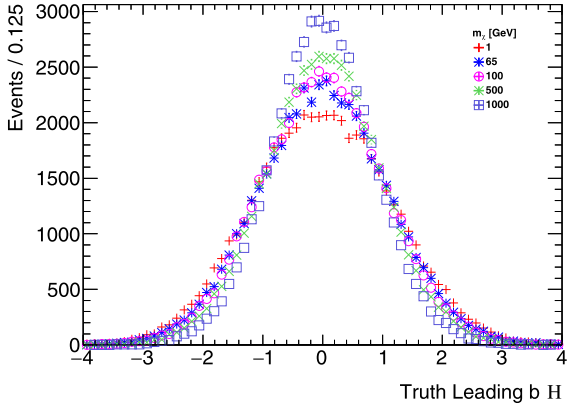

(b) Leading b—jet pseudorapidity

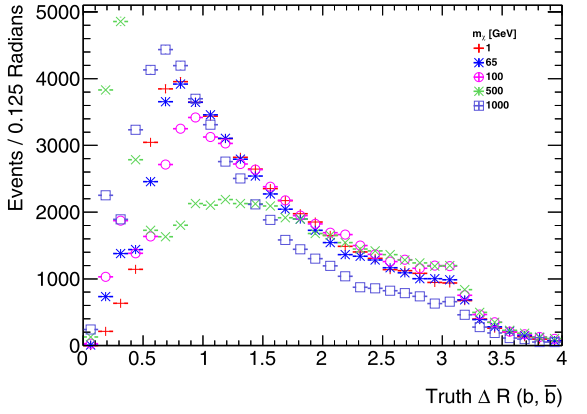

(c) Angular distance between the two leading b—jets

Fig. 50. Comparison of the kinematic distributions for the two leading jets from the Higgs decay in the scalar simplified model, when fixing the new scalar mass to 1000 GeV and varying the DM mass.

to Higgs+$\not{E}_T$ signatures, are mentioned in [45,97]. The first part of this Section outlines the main characteristics for a limited number of these models that could be considered in early Run-2 searches. However, the EFT approximation made for these operators can be problematic, see Ref. [97] for discussion. For this reason, model-independent results as in Appendix B should be privileged over considering these operators as realistic benchmarks.

However, the Forum discussion highlighted that the EFT approach allows more model-independence when reinterpreting results, and that it is worth still considering interpretation of the

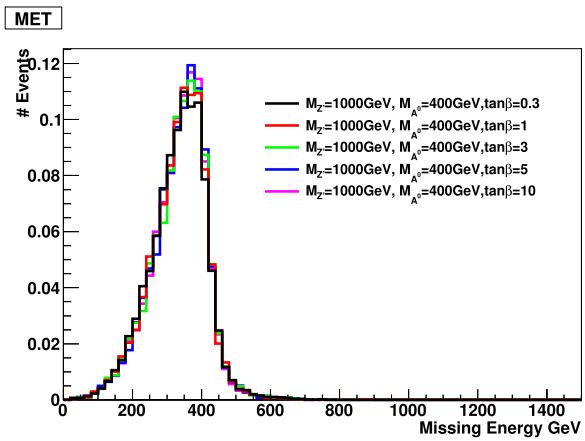

(a) $\not{E}_T$ distribution

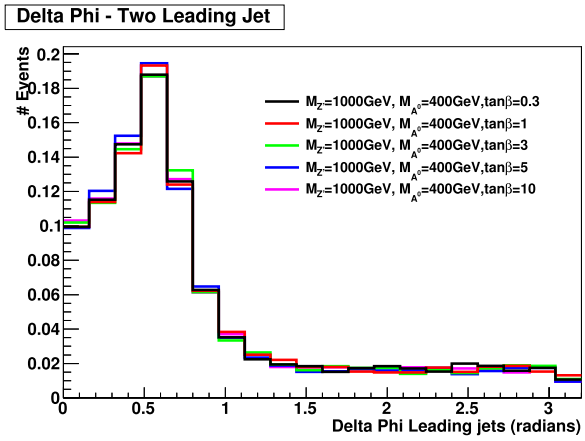

(b) $\Delta\phi$ distance between the two $b-$ jets

Fig. 51. Kinematic distributions of the signal process varying $\tan\beta$, in the case of a Higgs boson decaying into two b quarks, after parameterized detector simulation: no kinematic dependence is observed on the mixing angle.

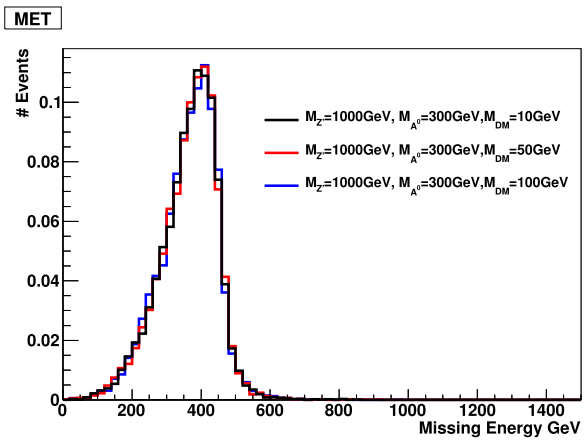

(a) $\not{E}_T$ distribution

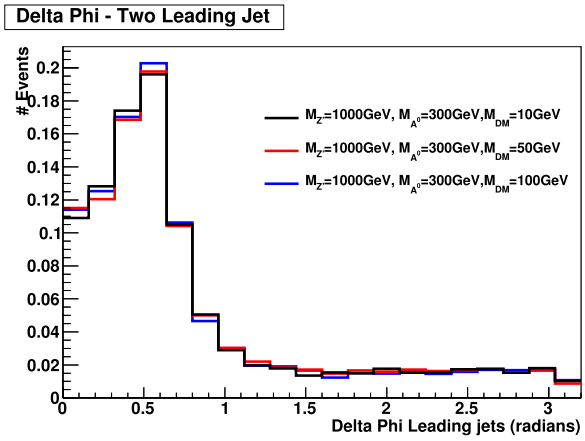

(b) $\Delta\phi$ distance between the two $b-$ jets

Fig. 52. Kinematic distributions of the signal process varying m_χ: minimal kinematic dependency on m_χ as expected when A^0 is produced on-shell. Plots shown for $M_{Z'} = 1000$ GeV, $M_{A^0} = 300$ GeV.

results available in terms of these operators. Furthermore, once simplified models are available for those operators, EFT results can be used as a limiting case for consistency checks. We devote the end of this Section to a discussion on the presentation of results from this model, including an assessment of their reliability using a conservative procedure that is only dependent on EFT parameters.

The studies in this Section have been performed using a UFO model within MadGraph5_aMC@NLO v2.2.3, interfaced to Pythia 8 for the parton shower. The implementation of these models is discussed further in Section 4.2.2.

3.2.1. Dimension 5 operators

The lowest dimension benchmark operators we consider are effective dimension 5, such as the one depicted in Fig. 57.

Following the notation of [45], models from this category have a Lagrangian that, after electroweak symmetry breaking, includes terms such as:

$$\frac{m_W^2}{\Lambda_5^3}\,\bar{\chi}\chi\,W^{+\mu}W^-_\mu + \frac{m_Z^2}{2\Lambda_5^3}\,\bar{\chi}\chi\,Z^\mu Z_\mu\,, \tag{39}$$

where m_Z and m_W are the masses of the Z and W boson, W^μ and Z^μ are the fields of the gauge bosons, χ denotes the Dark Matter fields and Λ_5 is the effective field theory scale. Note that these operators are of true dimension 7, but reduce to effective dimension 5 once the Higgs vacuum expectation values, contained in the W and Z mass terms, are inserted. As such, one expects that these operators would naturally arise in UV complete models where Dark Matter interacts via a Higgs portal where heavy mediators couple to the Higgs or other fields in an extended Higgs sector. In such models the full theory may be expected to contain additional operators with Higgs-Dark Matter couplings [104]. The above operator also induces signatures with $\not{E}_T$ in conjunction with Z and W bosons at tree level, as shown in Fig. 38, while at loop level it induces couplings to photon pairs and $Z\gamma$ through W loops. In these models, a clear relation exists between final states with photons, EW bosons and Higgs boson.

As shown in Fig. 58, the kinematics of this model can be approximated by that of a simplified model including a high-mass scalar mediator exchanged in the s-channel described in Section 2.2.2. For this reason, the list of benchmark models with direct boson-DM couplings for photon, Z and W only includes dimension 7 operators: if the scalar model with initial state radiation of an EW boson is already generated, then its results can be rescaled.

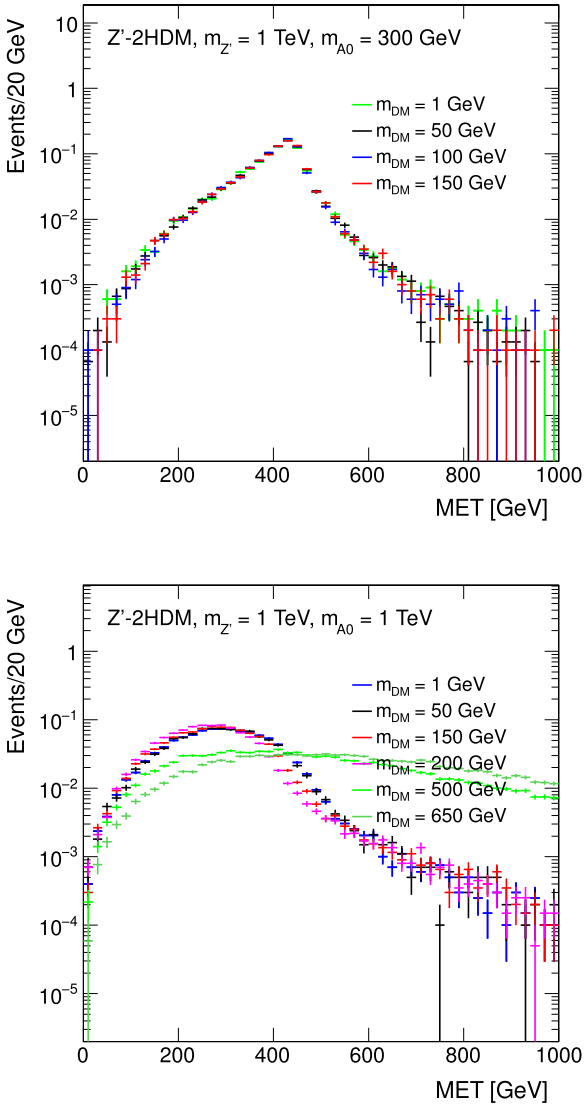

Fig. 53. Missing transverse momentum distributions at generator level in the Z' +2HDM scenario for different values of the DM mass m_χ, with $m_{Z'} = 1$ TeV and $m_{A^0} = 300$ GeV (left) and $m_{A^0} = 1$ TeV (right).

The Higgs+$\not{E}_T$ analysis, however, will not consider the scalar simplified model as benchmark, due to the very low sensitivity in early LHC analyses, and will instead use this dimension 5 operator.

Parameter scan. The two parameters of this model are the scale of new physics λ and the DM particle mass. SM-DM coupling and new physics scale are related by $g_\chi = (246\ \text{GeV})/\lambda$.

The initial value of the new physics scale λ chosen for the sample generation is 3 TeV. This is a convention and does not affect the signal kinematics: the cross-section of the samples can be rescaled when deriving the constraints on this scale. However, more care should be given when rescaling Higgs+$\not{E}_T$ operators of higher dimensions, as different diagrams have a different λ dependence.

The DM mass values for the benchmark points to be simulated are chosen to span a sufficient range leading to different kinematics, that is within the LHC sensitivity for early searches and that is consistent across the various signatures and EFT operators.

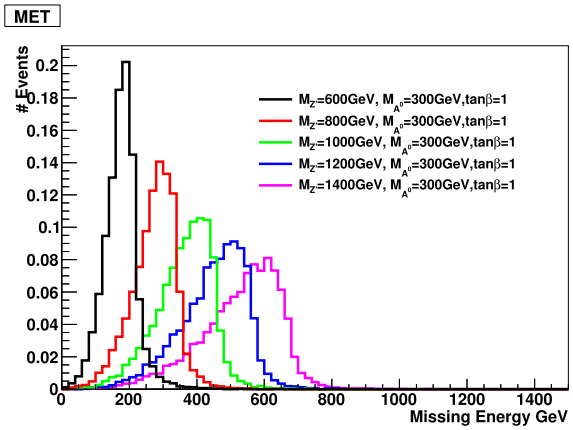

(a) $\not{E}_T$ distribution

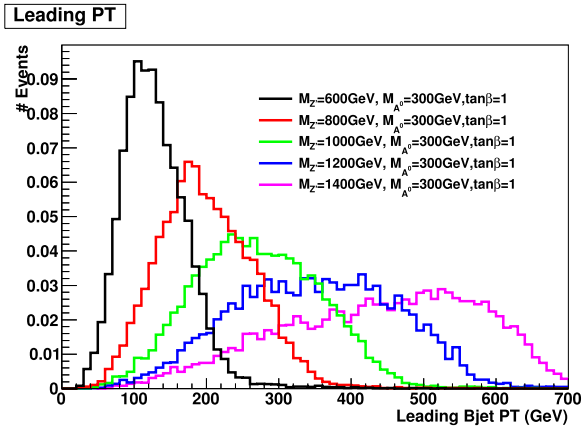

(b) Leading $b-$jet p_T distribution

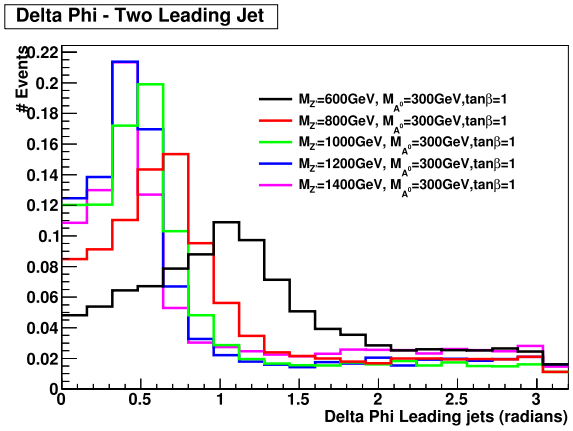

(c) $\Delta\phi$ distance between the two $b-$ jets

Fig. 54. Kinematic distributions of the signal process varying $M_{Z'}$, for $m_\chi = 100$ GeV, $M_{A^0} = 300$ GeV.

We therefore start the mass scan at $m_\chi = 1$ GeV, where collider experiments are complementary to direct and indirect detection and choose the last point corresponding to a DM mass of 1.3 TeV. We recommend a scan in the following mass points:

$m_\chi = 1, 10, 50, 100, 200, 400, 800, 1300$ GeV.

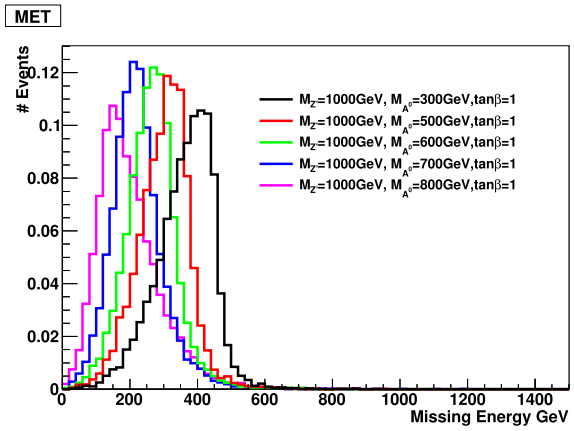

(a) $\not{E}_T$ distribution

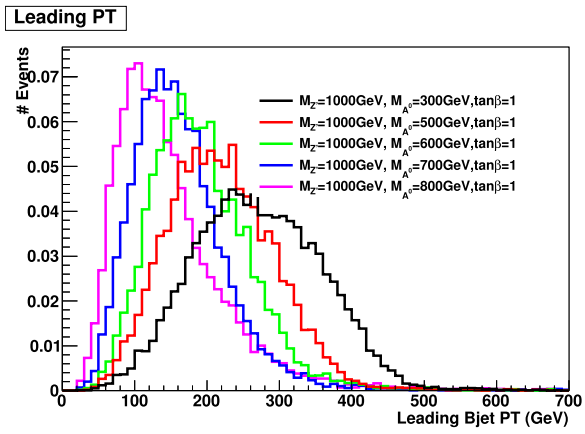

(b) Leading $b-$jet p_T distribution

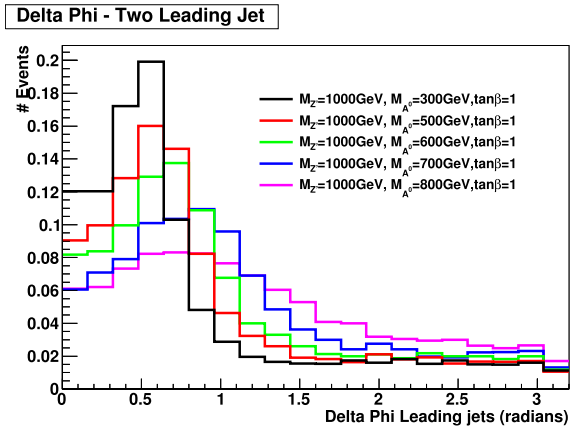

(c) $\Delta\phi$ distance between the two $b-$ jets

Fig. 55. Kinematic distributions of the signal process varying M_{A^0}, for $m_\chi = 100$ GeV, $M_{Z'} = 1000$ GeV.

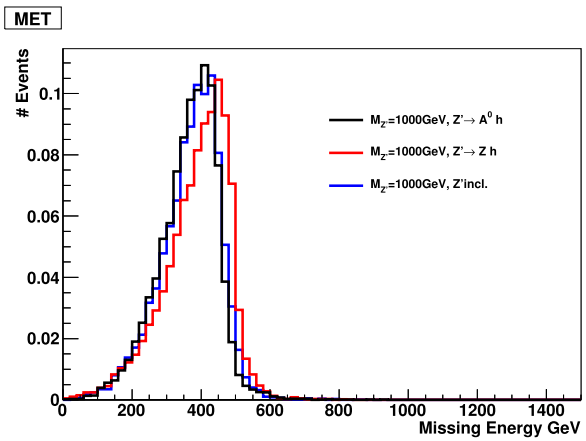

(a) $\not{E}_T$ distribution

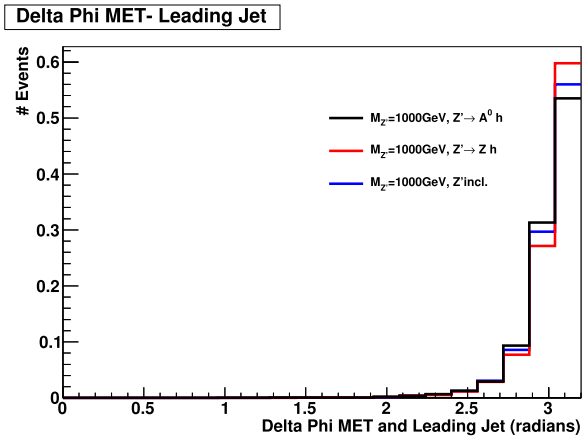

(b) Leading $b-$jet p_T distribution

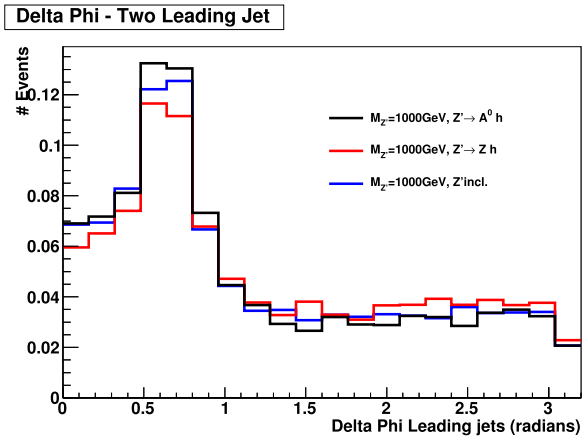

(c) $\Delta\phi$ distance between the two $b-$ jets

Fig. 56. Kinematic distributions of $Z' \to A^0 h$ exclusive production, $Z' \to Zh$ exclusive production and Z' inclusive production for $M_{Z'} = 1000$ GeV and $M_{A^0} = 300$ GeV.

A set of kinematic distributions from the Higgs+$\not{E}_T$ signature where the Higgs decays into two $b-$quarks is shown in Fig. 59, for points similar to those of the grid scan proposed.

3.2.2. Dimension 7 operators

The dimension-7 benchmark models contain the $SU(2)_L \times U(1)_Y$ gauge-invariant couplings between DM fields and the kinetic terms of the EW bosons. The CP-conserving scalar couplings

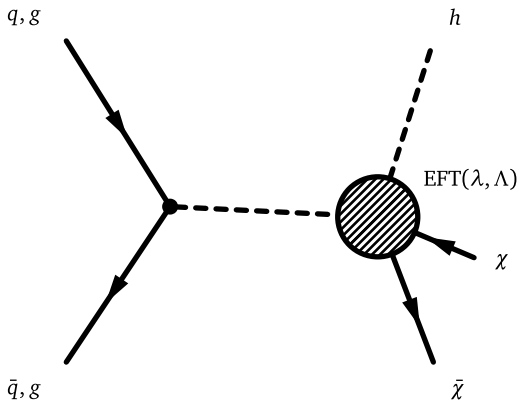

Fig. 57. Diagram for EFT operators giving rise to a Higgs+$\not{E}_T$ signature.

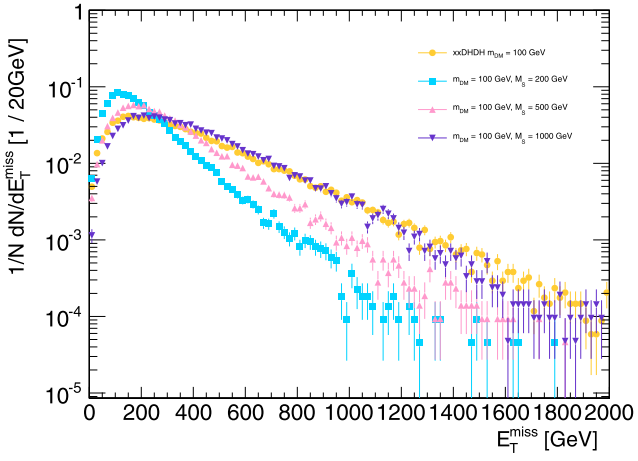

Fig. 58. Comparison of the missing transverse momentum for the simplified model where a scalar mediator is exchanged in the *s*-channel and the model including a dimension-5 scalar contact operator, in the leptonic Z+$\not{E}_T$ final state. All figures in this Section have been performed using a UFO model within MadGraph5_aMC@NLO v2.2.3, interfaced to Pythia 8 for the parton shower.

of this type can be written as

$$\frac{c_1}{\Lambda_S^3}\,\bar{\chi}\chi\,B_{\mu\nu}B^{\mu\nu} + \frac{c_2}{\Lambda_S^3}\,\bar{\chi}\chi\,W^i_{\mu\nu}W^{i,\mu\nu}\,. \tag{40}$$

Here $B_{\mu\nu} = \partial_\mu B_\nu - \partial_\nu B_\mu$ and $W^i_{\mu\nu} = \partial_\mu W^i_\nu - \partial_\nu W^i_\mu + g_2\epsilon^{ijk}W^j_\mu W^k_\mu$ are the $U(1)_Y$ and $SU(2)_L$ field strength tensor, respectively, and g_2 denotes the weak coupling constant. In the case of the pseudoscalar couplings, one has instead

$$\frac{c_1}{\Lambda_P^3}\,\bar{\chi}\gamma_5\chi\,B_{\mu\nu}\tilde{B}^{\mu\nu} + \frac{c_2}{\Lambda_P^3}\,\bar{\chi}\gamma_5\chi\,W^i_{\mu\nu}\tilde{W}^{i,\mu\nu}\,, \tag{41}$$

where $\tilde{B}_{\mu\nu} = 1/2\,\epsilon_{\mu\nu\lambda\rho}B^{\lambda\rho}$ and $\tilde{W}^i_{\mu\nu} = 1/2\,\epsilon_{\mu\nu\lambda\rho}W^{i,\lambda\rho}$ are the dual field strength tensors. In addition to the CP-conserving interactions (40) and (41), there are also four CP-violating couplings that are obtained from the above operators by the replacement $\bar{\chi}\chi \leftrightarrow \bar{\chi}\gamma_5\chi$.

The effective interactions introduced in (40) and (41) appear in models of Rayleigh DM [105]. Ultraviolet completions where the operators are generated through loops of states charged under $U(1)_Y$ and/or $SU(2)_L$ have been proposed in [106] and their LHC signatures have been studied in [107]. If these new charged particles are light, the high-p_T gauge bosons that participate in the $\not{E}_T$ processes considered here are able to resolve the substructure of the loops. This generically suppresses the cross sections compared to the EFT predictions [108], and thus will weaken the bounds on the interaction strengths of DM and the EW gauge bosons to some extent. Furthermore, the light charged mediators may be produced on-shell in *pp* collisions, rendering direct LHC searches potentially more restrictive than $\not{E}_T$ searches. Making the above statements precise would require further studies beyond the timescale of this forum.

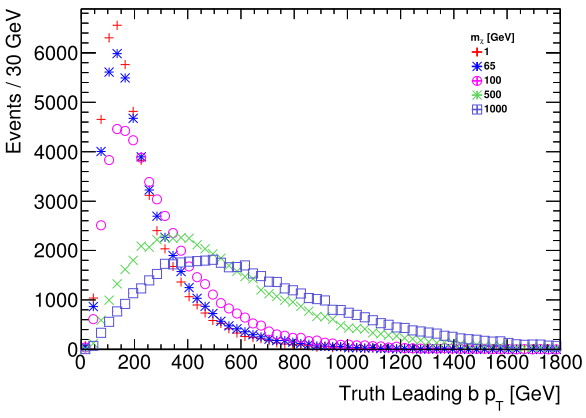

(a) Leading b—jet transverse momentum

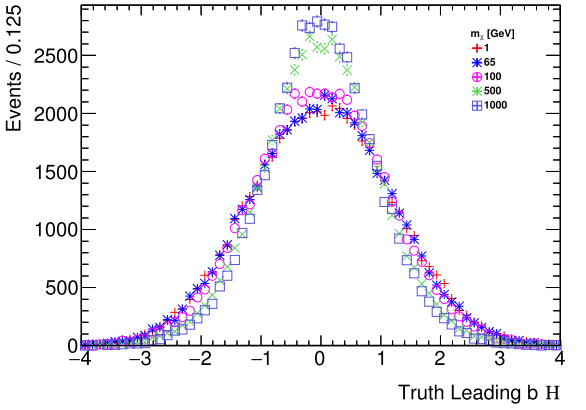

(b) Leading b—jet pseudorapidity

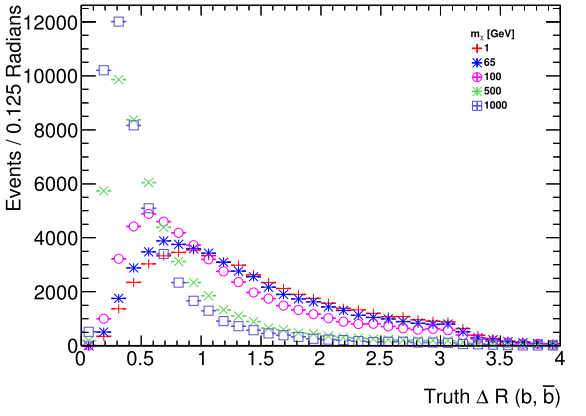

(c) Angular distance between the two leading b—jets

Fig. 59. Comparison of the kinematic distributions for the two leading b— jets (from the Higgs decay) in the model with direct interactions between the Higgs boson and the DM particle, when varying the DM mass.

Since for $\Lambda_S = \Lambda_P$ the effective interactions (40) and (41) predict essentially the same value of the mono-photon, mono-Z and mono-W cross section [45,99], we consider below only the former couplings. We emphasize however that measurements of the jet–jet azimuthal angle difference in $\not{E}_T$ +2j events may be used to disentangle whether DM couples more strongly to the combination $B_{\mu\nu}B^{\mu\nu}$ ($W^i_{\mu\nu}W^{i,\mu\nu}$) or the product $B_{\mu\nu}\tilde{B}^{\mu\nu}$ ($W^i_{\mu\nu}\tilde{W}^{i,\mu\nu}$) of field strength tensors [98,99].

After EW symmetry breaking the interactions (40) induce direct couplings between pairs of DM particles and gauge bosons. The corresponding Feynman rule reads:

$$\frac{4i}{\Lambda_S^3}\, g_{V_1V_2}\left(p_1^{\mu_2}p_2^{\mu_1} - g^{\mu_1\mu_2}\, p_1\cdot p_2\right), \tag{42}$$

where p_i (μ_i) denotes the momentum (Lorentz index) of the vector field V_i and for simplicity the spinors associated with the DM fields have been dropped. The couplings $g_{V_iV_j}$ take the form:

$$\begin{aligned} g_{\gamma\gamma} &= c_w^2 c_1 + s_w^2 c_2\,,\\ g_{\gamma Z} &= -s_w c_w\left(c_1 - c_2\right),\\ g_{ZZ} &= s_w^2 c_1 + c_w^2 c_2\,,\\ g_{WW} &= c_2\,, \end{aligned} \tag{43}$$

with s_w (c_w) the sine (cosine) of the weak mixing angle. Note that our coefficients c_1 and c_2 are identical to the coefficients C_B and C_W used in [99], while they are related via $k_1 = {c_w}^2 c_1$ and $k_2 = {s_w}^2 c_2$ to the coefficients k_1 and k_2 introduced in [45].

The coefficients c_1 and c_2 appearing in (43) determine the relative importance of each of the $\not{E}_T$ channels and their correlations. For example, one observes that:

- Only c_2 enters the coupling between DM and W bosons, meaning that only models with $c_2 \neq 0$ predict a mono-W signal;
- If $c_1 = c_2$ the mono-photon (mono-Z) signal does not receive contributions from diagrams involving Z (photon) exchange;
- Since numerically $c_w^2/s_w^2 \simeq 3.3$ the mono-photon channel is particularly sensitive to c_1.

Parameter scan. As stated above and shown in Ref. [100], the kinematic distributions for dimension-7 scalar and pseudoscalar operators only shows small differences. This has been verified from a generator-level study: the signal acceptance after a simplified analysis selection ($\not{E}_T$ >350 GeV, leading jet p_T > 40 GeV, minimum azimuthal difference between either of the two jets and the $\not{E}_T$ direction > 0.4) is roughly 70% for both models, independent from the coefficients c_1 and c_2. We therefore only suggest to generate one of the two models.

The differences in kinematics for the various signatures are negligible when changing the coefficients c_1 and c_2, since these coefficient factorize in the matrix element. Only the case $c_1 = c_2 = 1$ is generated as benchmark; other cases are left for reinterpretation as they will only need a rescaling of the cross-sections (see Fig. 60).

3.2.3. Higher dimensional operators

Many higher dimensional operators can induce signals of photons or $W/Z/H$ bosons in the final state. A complete list can be found in Refs. [47,48,97] and references therein.

Although with lower priority with respect to the operators above, a representative dimension-8 operators can be chosen as benchmark, with the form:

$$\frac{1}{\Lambda^4}\bar{\chi}\gamma^\mu\chi B_{\mu\nu}H^\dagger D^\nu H.$$

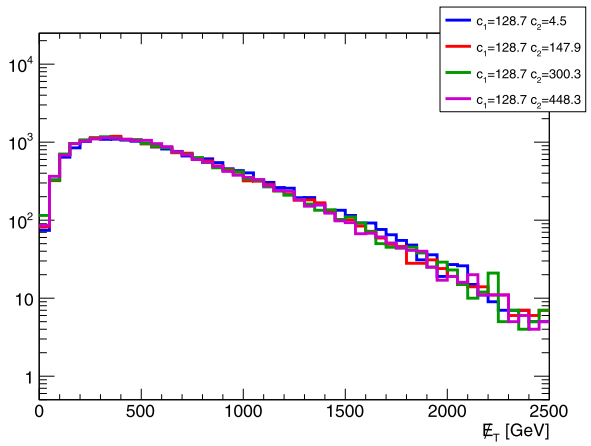

Fig. 60. $\not{E}_T$ distribution for the dimension-7 model with a hadronically decaying Z in the final state, for the scalar and pseudoscalar operators representing direct interactions between DM and bosons. The values of the coefficients in the legend are multiplied by 100.

In this case, the new physics scale is Λ is related to the coupling of the DM as $y_\chi = \frac{1}{\Lambda^4}$. An advantage of this operator is that it includes all signatures with EW bosons, allowing to assess the relative sensitivity of the various channels with the same model. The kinematics for this operator is different with respect to other operators, leading to a harder $\not{E}_T$ spectrum, as illustrated by comparing the leading $b-$jet distribution for the dimension 5 operator to the dimension 8 operator (see Fig. 61).

3.2.4. Validity of EW contact operators and possible completions

It is important to remember that the operators described in this section may present problems in terms of the validity of the contact interaction approach for the energy scales reached at the LHC.

As outlined in [97], designing very high $\not{E}_T$ search signal regions that are exclusively motivated by the hard $\not{E}_T$ spectra of the dimension 7 and 8 operators will mean that the momentum transfer in the selected events is larger. This in turn means that processes at that energy scale (mediators, particles exchanged in loops) are accessible, and a simple contact interaction will not be able to correctly describe the kinematics of these signals.

Contact interaction operators like the ones in this section remain useful tools for comparison of the sensitivity of different search channels, and for reinterpretation of other models under the correct assumptions. To date, while UV-complete models are known, their phenomenology has not been studied in full detail as their completion involves loops.[12]

However, this may be the focus of future theoretical exploration, as discussed in Ref. [99]. An example of a complete model for scalar DM corresponding to the dimension-5 operator is provided in the Appendix A. Providing results for the pure EFT limit of these models will prove useful to cross-check the implementation of future.

Given these considerations, we recommend to present results for these models as follows:

[12] An example case for the need of loop completions is a simplified model with an additional scalar exchanged at tree level. The scalar couples to WW and ZZ in a gauge-invariant way, Integrating out the mediator does not lead to the Lorentz structure of a dimension-7 operator, so it is not possible to generate dimension-7 operators that satisfy gauge and Lorentz invariance at the same time. A model with a spin-1 mediator cannot be considered as an candidate for completion either, since dimension-7 operators only have scalar or pseudoscalar couplings.

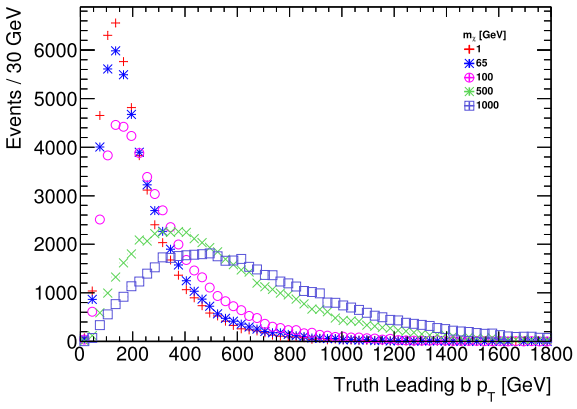

(a) Dimension 5 operator

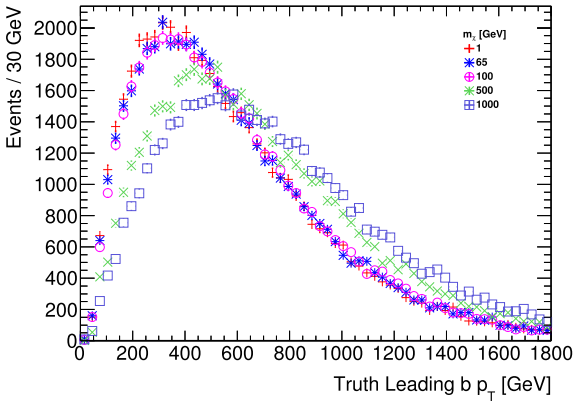

(b) Dimension 7 operator

Fig. 61. Comparison of the transverse momentum for the leading $b-$ jet from the Higgs decay for a dimension 5 and dimension 7 operator with direct boson-DM couplings.

- Deliver fiducial limits on the cross section of any new physics events, without any model assumption, according to the guidelines in Appendix B.
- Assess the percentage of events that pass a condition of validity for the EFT approximation that does not depend on a specific completion, and present results removing of the invalid events using the procedure in Section 5 alongside the raw EFT results.

4. Implementation of models

4.1. Implementation of s-channel and t-channel models for $\not{E}_T$ +X analyses

In the studies to date, a number of different Monte Carlo tools have been used to simulate DM signals. In this Chapter, we make recommendations on the accuracy at which simulations should be performed for different final states. We also provide explicit examples of codes and implementations (including specific settings) that have been used to obtain the results in this report. We stress that these recommendations are based on the current status of publicly available codes and users should always check whether new results at a better accuracy have appeared in the meantime. We recommend to update the corresponding analyses directly using the new releases and/or codes respectively, and in case this would not be possible, to at least take into account the new information in the analysis (e.g., via a MC comparison with the latest predictions, or by effectively using global/local K-factors). For all models included in this report, Pythia 8 has been used to provide the parton shower simulation. Nevertheless, we note that showering matrix element events with Herwig [109–112] should be considered as an equally valid alternative.

4.1.1. Implementation of s-channel models for mono-jet signature

These models include those discussed in Sections 2.1 and 2.2. In monojet analyses, i.e. when final states are selected with a few jets and $\not{E}_T$, observables and in particular the $\not{E}_T$ spectrum depend upon the accuracy of the simulation of QCD radiation. For the vector and axial vector models, the current state of the art is NLO+PS. It is particularly simple to obtain simulations for these processes at NLO+PS and even for merged samples at NLO accuracy, starting from SM implementations. We therefore recommend simulations to be performed at NLO+PS, and in case multi-jet observables are employed, by merging samples with different multiplicities. Results at such accuracy can be obtained either in dedicated implementations, such as that of POWHEG [61], or via general purpose NLO tools like MadGraph5_aMC@NLO employing available UFO models at NLO. A testing version of the full set of these UFO models has been made available only in June 2015 [113]. For this reason, it was not used as part of the studies of this Forum on initial Run-2 benchmark models. Nevertheless, we encourage further study of these UFO models by the ATLAS and CMS collaborations.

A study using POWHEG [61,114] has shown that the NLO corrections result in a substantial reduction in the dependence on the choice of the renormalization and factorization scales and hence a reduced theoretical uncertainty on the signal prediction. For the central choice of renormalization and factorization scales, the NLO corrections also provide a minor enhancement in the cross section due to the jet veto that has been so far employed in Run-1 analyses.

For the scalar and pseudoscalar models, the lowest order process already involves a one-loop amplitude in QCD. Because of the complexity of performing NLO calculations for this class of processes and in particular the absence of general methods for computing two-loop virtual contributions, only LO predictions are currently available. These can be interfaced to shower programs exactly as usual tree-level Born computations, i.e. by considering one parton multiplicity at a time or by merging different parton multiplicities via CKKW or MLM schemes to generate inclusive samples with jet rates at LO accuracy. For spin-0 mediators in the mono-jet final state, the top-quark loop is the most important consideration. The matrix element implementation with exact top-loop dependence of the s-channel spin-0 mediated DM production is available in MCFM [41,114][13] at fixed order and in POWHEG [43] and MadGraph5_aMC@NLO [113] for event generation at LO+PS level. The POWHEG and MCFM implementations include the finite top quark mass dependence for DM pair production and one extra parton at LO. The same processes are available in MadGraph5_aMC@NLO v2.3 and could be made available in the future in codes like Sherpa+OpenLoops/GoSam, including up to two extra partons in the final state. Samples can be merged employing CKKW, K_T-MLM procedures.

Most of the results that have been presented in this document for these processes have been obtained with POWHEG interfaced to Pythia 8, matching the state of the art calculation as of Spring 2015. For future reference, we document the specific settings needed to run the POWHEG generation for the dark matter models so they can serve as nominal benchmarks for the early Run-2

[13] Only the scalar mediator is available in the public release.

ATLAS and CMS DM analyses. POWHEG parameter cards for all models can be found on the Forum Git repository [115–118].

POWHEG *configuration for s-channel DM models.* The latest POWHEG release is available for download using the instructions at http://powhegbox.mib.infn.it/. The Forum recommends using at least version 3059.

- POWHEG can generate either unweighted (uniformly–weighted) or weighted events. The relevant keywords in the input card are `bornsuppfact` and `bornktmin`.

  1. unweighted events:
     `bornsuppfact`: negative or absent
     `bornktmin` PT
     This runs the program in the most straightforward way, but it is likely not the more convenient choice, as will be explained below. POWHEG will generate unweighted events using a sharp lower cut (with value PT) on the leading-jet p_{T}. Since this is a generation cut, the user must check that the choice of `bornktmin` does not change the cross section for signal events passing analysis selections. It is a good practice to use 10–20% smaller $\not{E}_T$ value in the input card than the final analysis selection, and check that the final result is independent, by exploring an even smaller value of `bornktmin`. The drawback of using this mode is that it is difficult to populate well, and in a single run, both the low-p_{T} region as well as the high-p_{T} tail.
  2. weighted events:
     `bornsuppfact` PTS
     `bornktmin` PT
     POWHEG will now produce weighted events, thereby allowing to generate a single sample that provides sufficient statistics in all signal regions. Events are still generated with a sharp lower cut set by `bornktmin`, but the `bornsuppfact` parameter is used to set the event suppression factor according to

$$F(k_{\mathrm{T}}) = \frac{k_{\mathrm{T}}^2}{k_{\mathrm{T}}^2 + \texttt{bornsuppfact}^2} \,. \tag{44}$$

     In this way, the events at, for instance, low $\not{E}_T$, are suppressed but receive higher weight, which ensures at the same time higher statistics at high $\not{E}_T$. We recommend to set `bornsuppfact` to 1000.
     The `bornktmin` parameter can be used in conjunction with `bornsuppfact` to suppress the low $\not{E}_T$ region even further. It is recommended to set `bornktmin` to one-half the value of the lowest $\not{E}_T$ selection. For instance, for the event selection used in the CMS/ATLAS monojet analyses, assuming the lowest $\not{E}_T$ region being defined above 300 GeV, the proposed value for `bornktmin` is 150. However, this parameter should be set keeping in mind the event selection of all the analyses that will use these signal samples, and hence a threshold lower than 150 may be required.

- The POWHEG monojet implementations can generate events using two expressions for the mediator propagators. The default setup (i.e if the keyword `runningwidth` is absent, commented out or set to 0) is such that a normal Breit–Wigner function is used for the propagator: in this case, the expression

$$Q^2 - M^2 + i M \Gamma$$

  is used for the propagator's denominator, where Q is the virtuality of the mediator, and M and Γ are its mass and width, respectively. This is the more straightforward, simple and transparent option, and it was used for the Forum studies. It should be the method of choice, unless one approaches regions of parameter space where Γ/M starts to approach order 1 values. In those cases, a more accurate modeling (or at least a check of the validity of the fixed width approach) can be achieved by using a running width: by setting the `runningwidth` token to 1, POWHEG uses as the denominator of the mediator propagator the expression

$$Q^2 - M^2 + i Q^2 \frac{\Gamma}{M},$$

  which is known to give a more realistic description. See Ref. [96] for a discussion.
- Set the parameters defining the bounds on the invariant mass of the dark matter pair, `mass_low` and `mass_high`, to −1. In this way, POWHEG will assign values internally.
- The minimal values for `ncall1`, `itmx1`, `ncall2`, `itmx2` are 250 000, 5, 1 000 000, 5 for the vector model, respectively.
- The minimal values for `ncall1`, `itmx1`, `ncall2`, `itmx2` are 100 000, 5, 100 000, 5 for the scalar top-loop model, respectively.
- When NLO corrections are included (as for instance in the vector model), negative-weighted events could occur and should be kept in the event sample, hence `withnegweights` should be set to 1. If needed, their fraction can be decreased by setting `foldsci` and `foldy` to larger values (2 for instance). `foldphi` can be kept to 1.
- One should use the automatic calculation of systematic uncertainties associated with the choice of hard scale and PDFs as described in Section 6.
- `idDM` is the integer that identifies the DM particle in the Monte Carlo event record. This should be chosen so that other tools can process the POWHEG output properly.

POWHEG in itself is not an event generator and must be interfaced with a tool that provides parton showering, hadronization, *etc.* For some time, a PYTHIA 8 [119] interface has existed for POWHEG. The PYTHIA 8 runtime configuration is the following:

```
POWHEG:veto = 1
POWHEG:pTdef = 1
POWHEG:emitted = 0
POWHEG:pTemt = 0
POWHEG:pThard = 0
POWHEG:vetoCount = 100
SpaceShower:pTmaxMatch = 2
TimeShower:pTmaxMatch = 2
```

As always, it is recommended to use the latest PYTHIA 8 release, available at http://home.thep.lu.se/torbjorn/Pythia.html. At the time of this report, the latest version is `8.209`.

4.1.2. Merging samples with different parton multiplicities

For the models discussed in the previous section, it is important to calculate the hard process as accurately as possible in QCD. For many other signal models, the $\not{E}_T$ signature depends more upon the production and decay of the mediator. In some cases, observables built in terms of the jets present in the final state are considered, relying on the assumption that inclusive samples accurate in higher jet multiplicities are available. In these cases, one can employ LO+PS simulations where different parton multiplicities are merged and then matched to parton shower, using schemes such as CKKW or MLM merging.

Here, we consider the example of an EFT model produced in association with up to 2 additional QCD partons. A Monte Carlo sample based on this method could be used in alternative to a NLO+PS sample for describing shapes and jet distributions (but not for the overall normalization which would still be at LO). The methodology described here could also be used for the t-channel model discussed in Section 2.3.

For the calculation of tree-level merged samples for DM signals, tools that can read UFO files and implement multi-parton merging should be employed, such that MadGraph5_aMC@NLO (+Pythia 8 or HERWIG++) and Sherpa [120]. In this report we have mostly employed MadGraph5_aMC@NLO.
MadGraph5_aMC@NLO provides a flexible and easy-to-use framework for implementing new models via the FeynRules package. MadGraph5_aMC@NLO can perform both LO and NLO calculations in QCD, matched/merged to parton showers [83]. For NLO ones, dedicated UFO model implementations at NLO should be used. Several UFO models at NLO are publicly available that although not developed specifically for DM, are suitable to make mode independent simulations at NLO accuracy, including multiparton merging via the FxFx technique [121]. A dedicated DM UFO implementation has been developed and it has been released as a testing version [113].

Merging events generated via matrix elements with different number of partons in the final state can be achieved by a judicious procedure that avoids double counting of the partons from matrix elements and parton showering. Several merging techniques are available. Based on some comparative studies [122], there is some advantage to using the CKKW-L merging scheme [123] implemented in Pythia 8. Alternatively, one can use the k_T-MLM scheme also available in Pythia 8.

Generation of the LHE file. The example presented here is a D5 EFT model, and includes tree-level diagrams with $\chi\bar{\chi}$+0,1,2 partons. We stress that MadGraph5_aMC@NLO, like POWHEG, is not in itself and event generator, but must be interfaced with an event generator through an LHE file. The production of the LHE file proceeds through setting the process parameters and the run parameters.

The process parameters are:

```
import model MODELNAME
generate p p > chi chi~ [QCD] @0
add process p p > chi chi~ j [QCD] @1
add process p p > chi chi~ j j [QCD] @2
```

The runtime parameters are more numerous, and define the collider properties, PDF sets, etc. The specific parameters needed for matching are, for the example of CKKW-L matching:

```
ickkw = 0
ktdurham = matching scale
dparameter = 0.4
dokt = T
ptj=20
drjj=0
mmjj=0
ptj1min=0
```

For different kinds of matching, a different choice of `ickkw` and related parameters would be made.

Implementation of the CKKW-L merging. To illustrate the settings related to merging different multiplicities, the EFT D5 samples were generated with MadGraph5_aMC@NLO version 2.2.2 and showered in Pythia 8.201, using the Madgraph parameters in the previous section (Section 4.1.2).

The Pythia 8 parameters for the CKKW-L k_T-merging scheme are:

```
Merging:ktType       = 1
Merging:TMS         = matching scale
1000022:all = chi chi~ 2 0 0 30.0 0.0 0.0 0.0 0.0 0.0
1000022:isVisible = false
Merging:doKTMerging    = on
Merging:Process      = pp>{chi,1000022}{chi~,
                         -1000022}
Merging:nJetMax      = 2
```

The matching scales should be the same for the generation and parton showering. In the model implementation, the particle data group ID 1000022 is used for weakly interacting dark matter candidates. Since this is a Majorana particle by default (with no corresponding anti-particle), and the model produces a DM Dirac fermion, the particle properties are changed accordingly. Also, the DM mass is set to 30 GeV. The `Merging:Process` command specifies the lowest parton emission process generated in MadGraph5_aMC@NLO and `Merging:nJetMax` = 2 gives the maximum number of additional parton emissions with respect to the lowest parton emission process.

In general, it is desired to take the hard parton emissions from the matrix element generation in MadGraph5_aMC@NLO and allow Pythia 8 to take care of soft emissions only. The transition between these two regimes is defined by the matching scale and its optimal value can be determined by studying the cross-section as a function of the number of jets (differential jet rates). The differential rates $\frac{dN_{i\to j}}{d\log_{10}(k_{\text{cut}})}$ give the number of events which pass from i jets to j jets as the k_T value increases beyond k_{cut}. An optimal matching scale should lead to smooth differential jet rates.

Two examples of differential jet rates, using matching scale 30 GeV and 80 GeV, from the EFT D5 sample generated as described in the previous section are given in Figs. 62 and 63, respectively. Although a kink is visible around the matching scale value in both cases, the 80 GeV scale leads to smoother distributions. In order to find the optimal matching scale, additional samples with matching scale 50, 70, and 90 GeV are generated as well and a detailed comparison of the differential jet rates close to the transition region is shown in Fig. 64. The largest differences among the samples are visible for the $1 \to 2$ jets transition where the 30 GeV and 50 GeV scale lead to a drop of the rates around the matching scale values. On the contrary, there is a hint of an increased rate around the matching scale value in the sample generated with the 90 GeV scale. Therefore, we recommend to use 80 GeV as the baseline matching scale.

The prescription for the event generation given in Section 4.1.2 starts with the emission of 0 partons and ends with maxim 2 partons in addition. Producing the samples separately allows to investigate the relative composition of the individual samples in various parts of the phase space. Fig. 65 shows the $\not{E}_T$ distribution of the EFT D5 sample with the matching scale at 80 GeV. The plot reveals that the 0-parton sample gives the dominant contribution in the region below the matching scale value that rapidly decreases at higher $\not{E}_T$. Assuming the lowest analysis $\not{E}_T$ cut in early Run-2 mono-jet analyses at 300 GeV, the generation of the 0-parton emission sample can be safely omitted as it only gives $< 1\%$ contribution at $\not{E}_T > 300$ GeV. For the 1- and 2-parton emission samples, one can use a generator cut on the leading parton p_{T}, `ptj1min`, in order to avoid generating low $\not{E}_T$ events that are irrelevant for the analysis.

In order to describe the signal kinematics correctly and save time during MC production, the parton emissions will only be

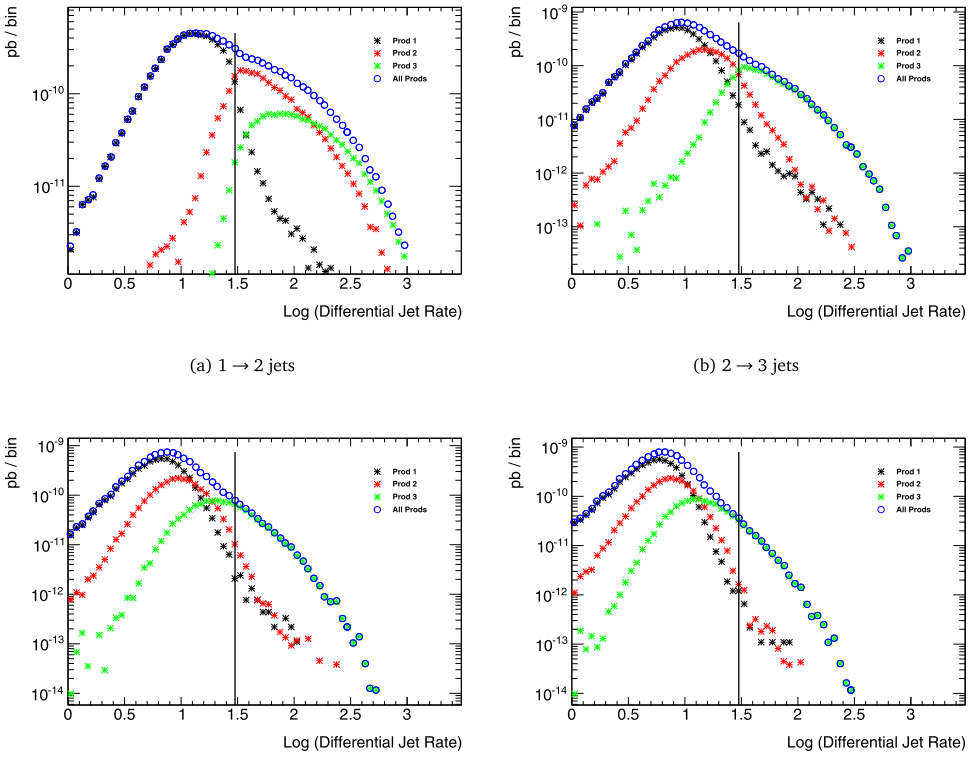

(a) $1 \to 2$ jets

(b) $2 \to 3$ jets

(c) $3 \to 4$ jets

(d) $4 \to 5$ jets

Fig. 62. Distributions of differential jet rates $\frac{dN_{i\to j}}{d\log_{10}(k_{\text{cut}})}$ for EFT D5 sample with CKKW-L matching scale at 30 GeV. The 0-, 1- and 2-parton emission samples are generated separately and indicated in the plots as Prod 1, Prod 2 and Prod 3, respectively. A vertical line is drawn at the matching scale.

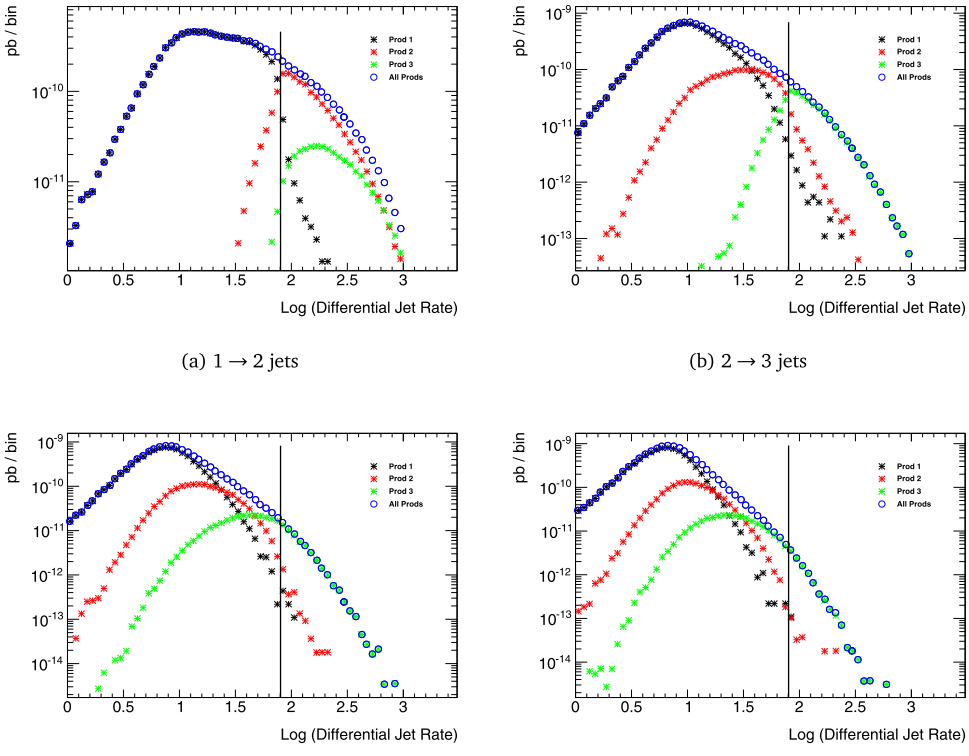

(a) $1 \to 2$ jets

(b) $2 \to 3$ jets

(c) $3 \to 4$ jets

(d) $4 \to 5$ jets

Fig. 63. Distributions of differential jet rates $\frac{dN_{i\to j}}{d\log_{10}(k_{\text{cut}})}$ for EFT D5 sample with CKKW-L matching scale at 80 GeV. The 0-, 1- and 2-parton emission samples are generated separately and indicated in the plots as Prod 1, Prod 2 and Prod 3, respectively. A vertical line is drawn at the matching scale.

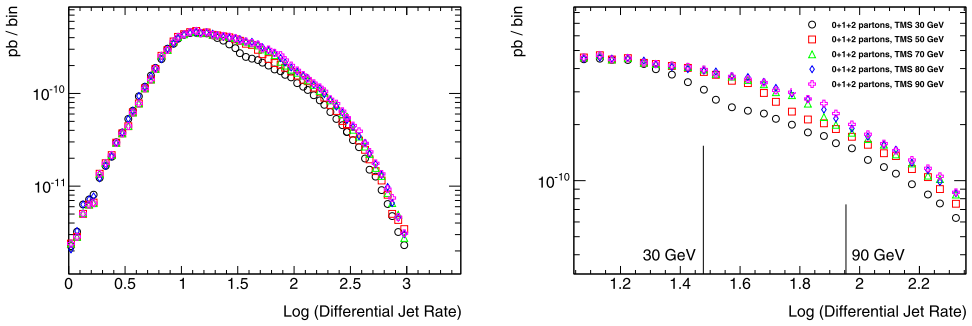

(a) $1 \rightarrow 2$ jets

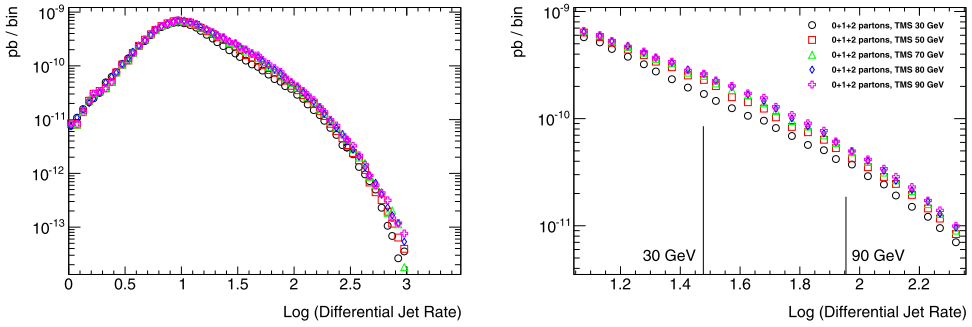

(b) $2 \rightarrow 3$ jets

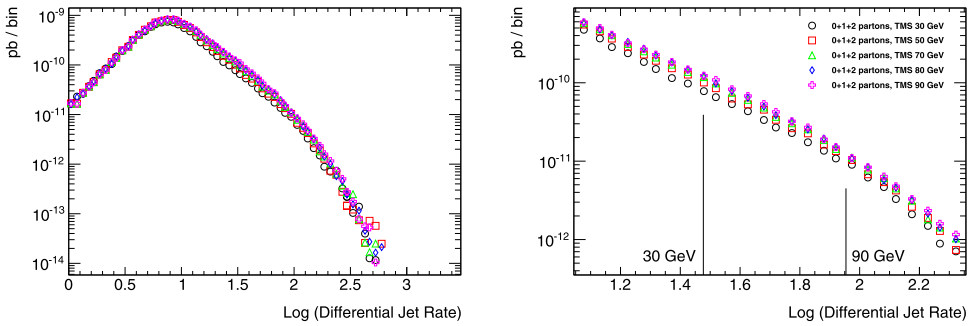

(c) $3 \rightarrow 4$ jets

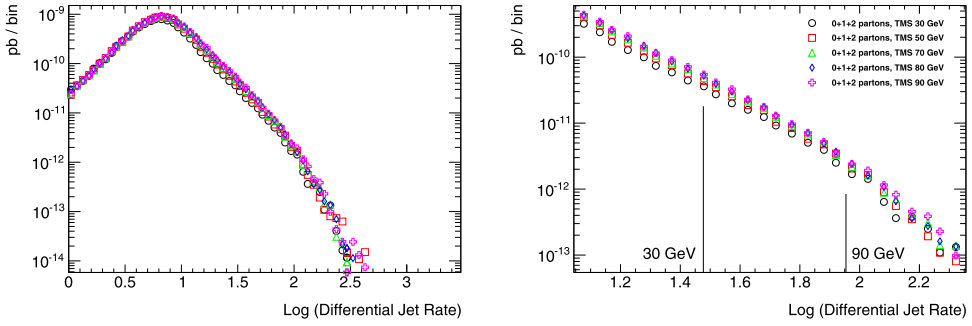

(d) $4 \rightarrow 5$ jets

Fig. 64. Distributions of differential jet rates $\frac{dN_{i\rightarrow j}}{d\log_{10}(k_{\text{cut}})}$ for EFT D5 sample with CKKW-L matching scale at 30, 50, 70, 80 and 90 GeV. A zoom of the region around the matching scale values is shown on right.

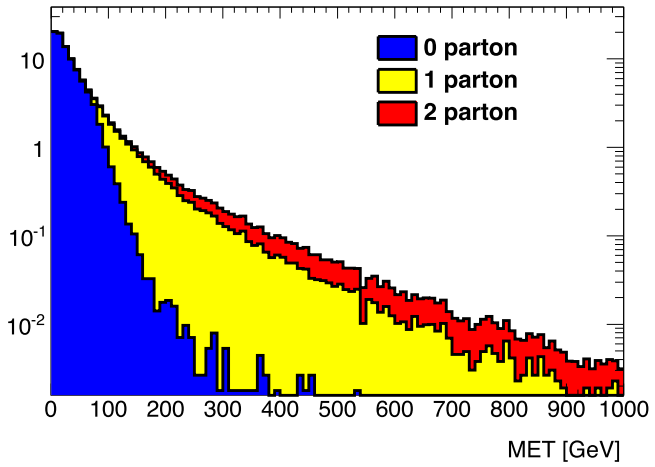

Fig. 65. Missing transverse momentum distributions for EFT D5 sample with CKKW-L matching scale at 80 GeV. Individual contributions from the 0-, 1- and 2-parton emission samples are shown.

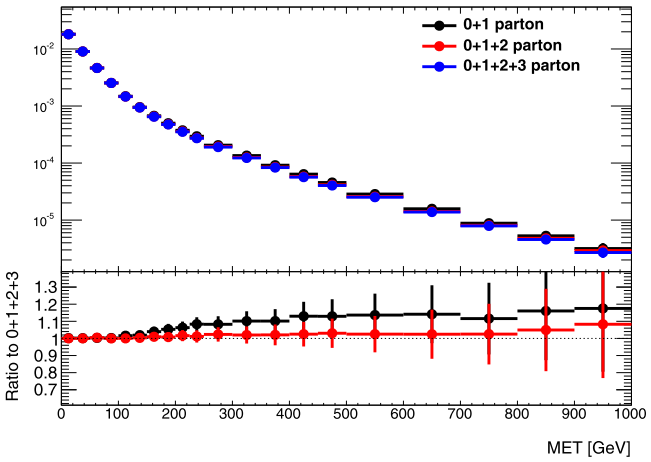

(a) No jet multiplicity cut

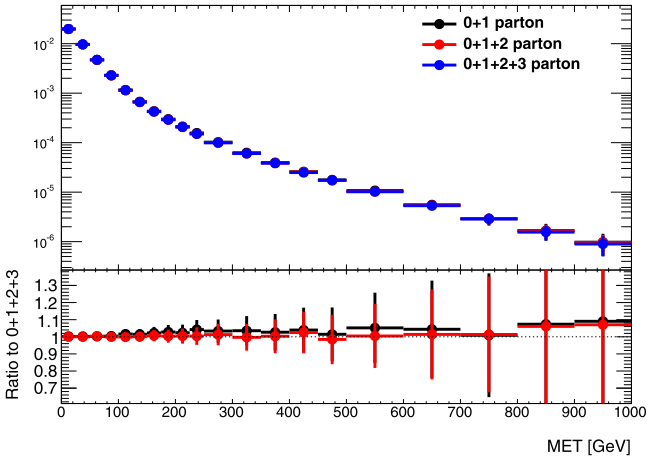

(b) $N_{\text{jet}} \leqslant 3$

Fig. 66. Missing transverse momentum distributions for EFT D5 sample with CKKW-L matching scale at 80 GeV produced with maximum 1 (black), 2 (red) and 3 (blue) partons emitted at the generator level. The ratios are shown with respect to the latter sample. (For interpretation of the references to color in this figure legend, the reader is referred to the web version of this article.)

generated up to a certain multiplicity. The higher multiplicity samples usually have small enough cross sections and the corresponding parts of the phase space can be sufficiently approximated by parton showering in Pythia 8. A dedicated study comparing samples generated with up to 1-, 2-, or 3-parton multiplicities was performed, using again the settings for the CKKW-L k_T-merging with the 80 GeV matching scale and the `Merging:nJetMax` parameter adjusted accordingly. Fig. 66 shows the $\not{E}_T$ distribution of the samples at $\not{E}_T > 250$ GeV.

With an event selection requiring $\not{E}_T$ and the leading jet p_{T} being larger than 250 GeV, the sample generated with up to 1 parton has 10.3% larger yield compared to the sample with up to 3 partons, while the yield of the sample with up to 2 partons is only 2.3% larger. If an additional cut is applied allowing for up to 3 jets with $p_{\text{T}} > 30$ GeV, the agreement improves to 3.2% larger for up to 1 parton and 0.7% larger for up to 2 partons, compared with up to 3 partons.

A similar comparison is shown in Fig. 67 for the jet multiplicity in the events with the leading jet $p_{\text{T}} > 250$ GeV, where an agreement at the level of $\sim$ 3% between the samples with up to 2 and 3 parton emissions is observed for number of jets up to 7. This justifies it is sufficient to produce samples with up to 2 parton emissions only at the generator level and ignore generating higher parton emissions.

4.1.3. Implementation of t-channel models for the jet+$\not{E}_T$ final state

The simulations for t-channel models are available via LO UFO implementations, where events are generated at LO+PS accuracy. The UFO file and parameter cards for the t-channel models with couplings to light quarks only [78] can be found on the Forum Git repository [124]. The model files from Ref. [46] can also be found on the repository [125]. The latter is the implementation that has been used for the studies in this report: in the monojet case there are only cross section differences between this model and the model in [124].

Multi-parton simulation and merging are necessary and require particular care for this model: this has not been a topic of detailed studies within the Forum, and we suggest to follow the procedure outlined in Ref. [78].

4.1.4. Implementation of s-channel and t-channel models with EW bosons in the final state

Currently, simulations for most of these models are available via LO UFO implementations, allowing event generation at the LO+PS accuracy. We note, however, that inclusion of NLO corrections would be possible. In MadGraph5_aMC@NLO, for example, this amounts to simply upgrading the currently employed UFO models to NLO, where the calculations exist for this class of processes. However, this was not available within the timescale of the Forum towards simulation of early Run-2 benchmarks. As a consequence, in this work we have used LO UFO implementations within MadGraph5_aMC@NLO 2.2.3 interfaced to Pythia 8 for the parton shower. The corresponding parameter cards used for the Run-2 benchmark models can be found on the Forum Git repository [126]. This is the implementation that will be used for early Run-2 LHC Dark Matter searches.

None of these models requires merging samples with different parton multiplicities since the visible signal comes from the production of a heavy SM boson whose transverse momentum distribution is sufficiently well described at LO+PS level. As a result, no special runtime configuration is needed for Pythia 8.

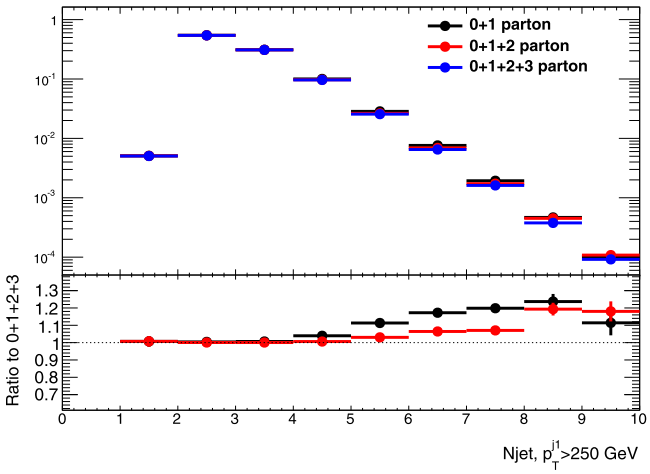

Fig. 67. Multiplicity of jets with $p_T > 30$ GeV and $|\eta| < 2.8$ for EFT D5 sample with CKKW-L matching scale at 80 GeV produced with maximum 1 (black), 2 (red) and 3 (blue) partons emitted at the generator level. The ratios are shown with respect to the latter sample. The leading jet p_T is required to be larger than 250 GeV. (For interpretation of the references to color in this figure legend, the reader is referred to the web version of this article.)

4.1.5. Implementation of s-channel and t-channel models with heavy flavor quark signatures

Dedicated implementations for DM signals in this final state are available at LO+PS accuracy. However, the state of the art of the simulations for $t\bar{t}$ and $b\bar{b}$ with a generic scalar and vector mediator is NLO+PS accuracy. For example, simulations for $t\bar{t}$ + scalar can be obtained via POWHEG and SHERPA starting from the SM implementations. In MADGRAPH5_AMC@NLO, all final relevant final states, spin-0 (scalar and pseudo scalar) and spin-1, (vector and axial) are available at NLO+PS via the dedicated NLO UFO for DM has been released in June 2015 [113]).

Within the scope of the Forum, simulations for the $t\bar{t}$ and $b\bar{b}$ signatures of the scalar mediator model have been generated starting from a leading order UFO with MADGRAPH5_AMC@NLO 2.2.2, using PYTHIA 8 for the parton shower. The UFO file and parameter cards that will be used as benchmarks for early Run-2 searches in these final states can be found on the Forum Git repository [127]. Multi-parton merging has been used for the $b\bar{b}$ case but it has not been studied in detail within this Forum. The b-flavored DM model of Section 2.3.2 is simulated at LO+PS using MADGRAPH5_AMC@NLO v2.2.3 and PYTHIA 8 for the parton shower. The corresponding UFO and parameter files can be found on the Forum Git repository [128].

Quark flavor scheme and masses. In the case of $b\bar{b}$ final state an additional care should be taken when choosing the flavor scheme generation and whether quarks should be treated as massive or massless.

The production of DM+$b\bar{b}$, dark matter in association with b jets via a decay of a (pseudo) scalar boson, is dominated in simplified mediator models by the gluon–gluon initiated production, similar to the production of Z+$b\bar{b}$ at the LHC. The Z+$b\bar{b}$ process has been studied in detail in the Z(ll)+b-jets final state, which can be used to validate both the modeling of DM+bb and, its main background, Z($\nu\nu$)+$b\bar{b}$. In this context, the p_T of the Z boson is related to the observed MET, whereas the b-jet kinematics determines the ratio of mono-b/di-b signatures in the detector.

For basic kinematic criteria applied to Z+$b\bar{b}$ production, this process leads in $\sim$ 90% of the events to a signature with only 1 b-jet in the acceptance ('Z+1b-jet production') and only in $\sim$ 10% of the events to a signature with 2 b-jets in the detector ('Z+2b-jets production'). The production cross section of the Z+$b\bar{b}$ process can be calculated in the 'five-flavor scheme', where b quarks are assumed massless, and the 'four-flavor scheme', where massive b quarks are used [129–131]. Data slightly favor the cross-section predictions in the five-flavor scheme [132] for the 1 b-jet signature. In this document we have preferred the 5-flavor scheme due to its simplicity and cross section agreement within the SM. The PDF used to calculate these cross section is NNPDF3.0 (lhaid 263000).

On the other hand, both data [132–134] and theoretical studies [135,136] suggest that the best modeling of an inclusive Z+$b\bar{b}$ sample especially for what concerns b-quark observables, is achieved at NLO+PS using a 4-flavor scheme and a massive treatment of the b-quarks. In Fig. 68 we show that, at LO, as expected, no appreciable difference is visible in the kinematics between either flavor scheme used for DM+$b\bar{b}$. In our generation we have used NNPDF3.0 set (lhaid 263400).

4.2. Implementation of specific models for $V + \not{E}_T$ analyses

4.2.1. Model implementation for mono-Higgs models

Currently, simulations for most of these models are available via LO UFO implementations, allowing event generation at the LO+PS accuracy. We note, however, that the inclusion of NLO corrections would be possible but not available in time for the conclusion of these studies. In MADGRAPH5_AMC@NLO, for example, this amounts to simply upgrading the currently employed UFO models to NLO. Simulation of loop-induced associated production of DM and Higgs is also possible with the exact top-quark mass dependence. In MADGRAPH5_AMC@NLO, for example, this can be obtained from the NLO UFO SM and 2HDM implementations.

In this work all three Higgs+$\not{E}_T$ models have been generated at leading order with MADGRAPH5_AMC@NLO 2.2.2, using PYTHIA 8 for the parton shower. No merging procedure has been employed. The LO UFO implementations of the scalar and vector models that will be used as early Run-2 benchmarks can be found on the Forum Git repository [137], while the 2HDM model can be found at this link [138].

As a final technical remark, we suggest always to let the shower program handle the h decay (and therefore to generate a stable h at the matrix element level). In so doing a much faster generation is achieved and the h branching ratios are more accurately accounted for by the shower program.

MADGRAPH5_AMC@NLO *details for scalar mediator Higgs+MET model.* The case of the associated production of a Higgs and scalar mediator via a top-quark loop can be either considered exactly or via an effective Lagrangian where the top-quark is integrated out. While this latter model has been shown not to be reliable [108,139,140], for simplicity we have chosen to perform the study in this tree-level effective formulation. A full study of the process including finite top-quark mass and parton shower effects is possible yet left for future work.

MADGRAPH5_AMC@NLO *details for 2HDM Higgs+MET model.* While a 2HDM UFO implementation at NLO accuracy to be used with MADGRAPH5_AMC@NLO has been made available at the end of the work of the Forum [113], in this work we have only considered LO simulations.

The two couplings that can be changed in the implemented model follow the nomenclature below:

- Tb - $\tan\beta$
- gz - g_z, gauge coupling of Z' to quarks

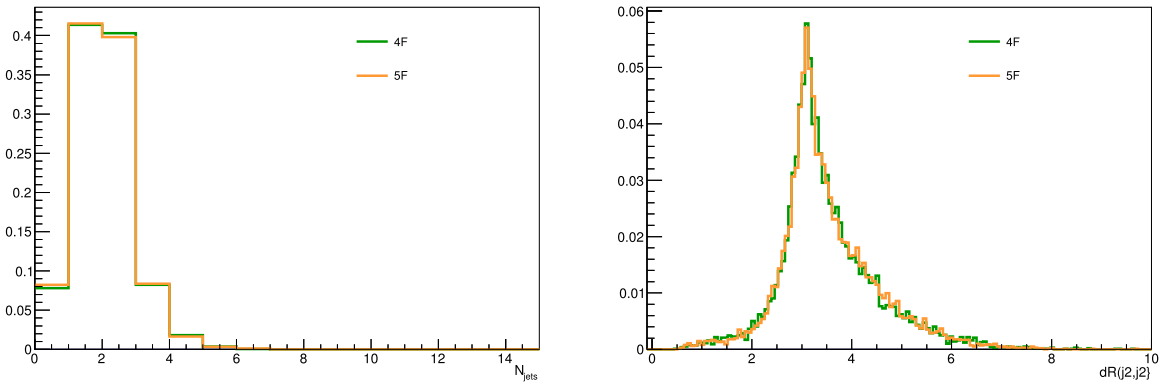

Fig. 68. Comparison of the jet multiplicity (left) and angular correction $\Delta R(j_1, j_2)$ (right) for the DM+$b\bar{b}$ scalar model generated in the 4-flavor and 5-scheme. The samples are generated for $m_\chi = 1$ GeV and $m_\phi = 10$ GeV.

The other couplings are not changed, including gx (the $A\bar{\chi}\chi$ coupling) which has little impact on the signal. $\sin\alpha$ is fixed internally such that $\cos(\beta - \alpha) = 0$. The width of the Z' and A can be computed automatically within MadGraph5_aMC@NLO. The couplings here do not affect the signal kinematics, so they can be fixed to default values and then the signal rates can be scaled appropriately.

The nomenclature for the masses in the implemented model is:

- `MZp` - PDG ID 32 - Z'
- `MA0` - PDG ID 28 - A
- `MX` - PDG ID 1000022 - dark matter particle

The other masses are unchanged and do not affect the result. Both $Z' \to hZ(\bar{\nu}\nu)$ and $Z' \to hA(\bar{\chi}\chi)$ contribute to the final state, scaling different with model parameters. We recommend to generate them separately, and then add the two signal processes together weighted by cross sections.

4.2.2. Implementation of EFT models for EW boson signatures

The state of the art for these models is LO+PS. NLO+PS can be achieved as well, but the corresponding implementation is not yet available. In our simulations we have implemented the models in the corresponding UFO files and generated events at LO via MadGraph5_aMC@NLO 2.2.2, using Pythia 8 for the parton shower. UFO files and parameter cards that will be used as early Run-2 benchmarks can be found on the Forum Git repository: [137] for operators with Higgs+MET final states and [141] for $W/Z/\gamma$ final states. These models do not require merging.

5. Presentation of EFT results

Most of this report has focused on simplified models of dark matter. In this Chapter, we wish to emphasize the applicability of Effective Field Theories (EFTs) in the interpretation of DM searches at the LHC. Given our current lack of knowledge about the nature of a DM particle and its interactions, it appears mandatory to provide the necessary information for a model independent interpretation of the collider bounds. This approach should be complemented with an interpretation within a choice of simplified models. We note that, even though EFT benchmarks are only valid in given conditions, the results provided by the current list of simplified models cannot always characterize the breadth of SM-DM interactions. In at least one case, composite WIMPs [142–144], the contact interaction framework is the correct one to constrain new confinement scales.

Ideally, experimental constraints should be shown as bounds of allowed signal events in the kinematic regions considered for the search, as detailed in Appendix B. A problematic situation is the attempt to derive a limit on nucleon–dark matter scattering cross sections from EFT results based on collider data.[14] Experiments that directly probe the nucleon–dark matter scattering cross section are testing the regime of small momentum transfers, where the EFT approximation typically holds. Collider experiments, though, are sensitive to large momentum transfers: We first illustrate the complications that can arise with EFTs at colliders by considering an effective interaction

$$\mathscr{L}_{\rm int} = \frac{(\bar{q}\gamma_\mu q)(\bar{\chi}\gamma^\mu\chi)}{M_*^2} = (\bar{q}\gamma_\mu q)(\bar{\chi}\gamma^\mu\chi)\frac{g}{\Lambda^2}$$

that couples quarks and DM χ fields.[15] The strength of this interaction is parameterized by $\frac{1}{M_*^2} = \frac{g}{\Lambda^2}$. A monojet signature can be generated from this operator by applying perturbation theory in the QCD coupling. An experimental search will place a limit on M_*. For a fixed M_*, a small value of g will correspond to a small value of Λ. The EFT approximation breaks down if $Q > \Lambda$, where Q is a typical hard scale of the process. The limit on small g can only be reliable if the kinematic region $Q > \Lambda$ is removed from the event generation. However, if a fraction of events is removed from the prediction, the corresponding value of g must increase to match the experimental limit on M_*. On the other hand, if, for the same value of M_*, a large Λ is assumed so that the full set of events fulfill the EFT validity condition, a larger value of g is required. For large enough g, computations based on perturbation theory become unreliable.

In the first part of this Chapter, we summarize two methods that have been advocated to truncate events that do not fulfill the condition necessary for the use of an EFT. These methods are described in detail in Refs. [7,28,80,97,145,146]. We then propose a recommendation for the presentation of EFT results for early Run-2 LHC searches.

5.1. Procedures for the truncation of EFT benchmark models

5.1.1. EFT truncation using the momentum transfer and information on UV completion

In the approach described in Ref. [145], the EFT prediction is modified to incorporate the effect of a propagator for a relatively

[14] Comparisons between constraints from different experiments meant to highlight their complementarity should be expressed as a function of the model parameters rather than on derived observables; however this is a point that should be developed further after the conclusion of the work of this Forum.

[15] The *exact* operator chosen is not important: as detailed in the following, statements concerning the applicability of an EFT can also be made without a specific relation to simplified models.

light mediator. For a tree-level interaction between DM and the SM via some mediator with mass $M_{\rm med}$, the EFT approximation corresponds to expanding the propagator for the mediator in powers of $Q_{\rm tr}^2/M_{\rm med}^2$, truncating at lowest order, and combining the remaining parameters into a single parameter M_* (connected to the scale of the interaction Λ in the literature). For an example scenario with a Z'-type mediator (leading to some combination of operators D5 to D8 in the notation of [23] for the EFT limit), this corresponds to setting

$$\frac{g_\chi g_{\rm q}}{Q_{\rm tr}^2 - M_{\rm med}^2} = -\frac{g_\chi g_{\rm q}}{M_{\rm med}^2}\left(1 + \frac{Q_{\rm tr}^2}{M_{\rm med}^2} + \mathcal{O}\left(\frac{Q_{\rm tr}^4}{M_{\rm med}^4}\right)\right) \simeq -\frac{1}{M_*^2}, \tag{45}$$

where $Q_{\rm tr}$ is the momentum carried by the mediator, and g_χ, $g_{\rm q}$ are the DM-mediator and quark-mediator couplings respectively.[16] A minimal condition that must be satisfied for this approximation to be valid is that $Q_{\rm tr}^2 < M_{\rm med}^2 = g_\chi g_{\rm q} M_*^2$. This requirement avoids the regions: $Q_{\rm tr}^2 \sim M_{\rm med}^2$, in which case the EFT misses a resonant enhancement, and it is conservative to ignore this enhancement; and $Q_{\rm tr}^2 \gg M_{\rm med}^2$, in which case the signal cross section should fall according to a power of $Q_{\rm tr}^{-1}$ instead of $M_{\rm med}^{-1}$. The latter is the problematic kinematic region.

The condition $Q_{\rm tr}^2 < M_{\rm med}^2 = g_\chi g_{\rm q} M_*^2$ was applied to restrict the kinematics of the signal and remove events for which the high-mediator-mass approximation made in the EFT would not be reliable. This leads to a smaller effective cross-section, after imposing the event selection of the analysis. This truncated signal was then used to derive a new, more conservative limit on M_* as a function of $(m_\chi, g_\chi g_{\rm q})$.

For the example D5-like operator, where the cross section σ scales as M_*^{-4}, there is a simple rule for converting a rescaled cross section into a rescaled constraint on M_*. if the original limit is based on a simple cut-and-count procedure. Defining $\sigma_{\rm EFT}^{\rm cut}$ as the cross section truncated such that all events pass the condition $\sqrt{g_\chi g_{\rm q}} M_*^{\rm rescaled} > Q_{\rm tr}$, we have

$$M_*^{\rm rescaled} = \left(\frac{\sigma_{\rm EFT}}{\sigma_{\rm EFT}^{\rm cut}(M_*^{\rm rescaled})}\right)^{1/4} M_*^{\rm original}, \tag{46}$$

which can be solved for $M_*^{\rm rescaled}$ via either iteration or a scan. Similar relations exist for a given UV completion of each operator.

This procedure has been proposed in Ref. [145] and its application to ATLAS results can be found in Ref. [7] for a range of operators. We reiterate: knowledge of the UV completion for a given EFT operator was necessary for this procedure; this introduces a model-dependence that was not present in the non-truncated EFT results.

Currently, simplified models (including the full effect of the mediator propagator) are available for comparison with the data, and since knowledge of the simplified models is needed for the truncation procedure, there is no reason to apply this prescription. Instead, the simplified model limit for large M_* can be presented for interpretation in terms of EFT operators.

5.1.2. EFT truncation using the center of mass energy

The procedure presented in the previous section was predicated on some knowledge of the simplified model. This led to the identification of the mass of the DM pair as the relevant kinematic quantity to use in a truncation procedure. In general, if no assumption is made about the underlying dynamics, it is more conservative to place a limit on the total center of mass energy $E_{\rm cm}$ of the DM production process. Furthermore, the direct connection between the mass scale of the EFT validity, $M_{\rm cut}$, and the mass scale that normalizes the EFT operator, M_*, is unknown. For such cases, Refs.[97,146] proposed a procedure to extract model independent and consistent bounds within the EFT that can be applied to any effective Lagrangian describing the interactions between the DM and the SM. This procedure provides conservative limits that can be directly reinterpreted in any completion of the EFT. The condition ensuring that the EFT approximation is appropriate is:

$$E_{\rm cm} < M_{\rm cut}\,. \tag{47}$$

The relationship between $M_{\rm cut}$ and M_* can be parameterized by an *effective coupling strength* g_*, such that $M_{\rm cut} = g_* M_*$. A scan over values of g_* provides an indication of the sensitivity of the prediction to the truncation procedure. In the Z'-type model considered above, g_* is equal to $\sqrt{g_\chi g_{\rm q}}$. The resulting plots are shown in [146] for a particular effective operator.

The advantage of this procedure is that the obtained bounds can be directly and easily recast in any completion of the EFT, by computing the parameters M_*, $M_{\rm cut}$ in the full model as functions of the parameters of the complete theory. On the other hand, the resulting limits will be weaker than those obtained using $Q_{\rm tr}$ and a specific UV completion.

5.1.3. Truncation at the generator level

The conditions on the momentum transfer can also be applied directly at the generator level, by discarding events that are invalid and calculating the limits from this truncated shape. This provides the necessary rescaling of the cross section while keeping the information on the change in the kinematic distributions due to the removal of the invalid events. This procedure is more general with respect to rescaling the limit in the two sections above, and it should be followed if a search is not simply a counting experiment and exploits the shapes of kinematic distributions.

5.1.4. Sample results of EFT truncation procedures

An example of the application of the two procedures to the limit on M_* from Ref. [14] as a function of the product of the couplings is shown in Fig. 69. Only the region between the dashed and the solid line is excluded. It can be seen that the procedure from [146] outlined in Section 5.1.2, shown in blue, is more conservative than the procedure from Refs. [7,145], described in Section 5.1.1.

5.1.5. Comments on unitarity considerations

A further consideration applicable to EFT operators at hadron colliders is the potential violation of unitarity. An analysis of the operator $\frac{\bar{q}\gamma_\mu q \bar{\chi}\gamma^\mu \chi}{M_*^2}$ provides the limit:

$$M_* > \beta(s)\sqrt{s}\sqrt{\frac{\sqrt{3}}{4\pi}}, \tag{48}$$

where $\sqrt{s}$ is (maximally) the collider energy and $\beta(s)$ is the DM velocity [24]. Constraints for other operators have also been derived [147]. This constraint on M_* still is open to interpretation, since the relation to $M_{\rm cut}$ is not resolved, except for a specific simplified model. Derived limits on M_* should be compared to this unitarity bound to check for consistency.

5.2. Recommendation for presentation of EFT results

In this report, we make two recommendations for the presentation of collider results in terms of Effective Field Theories for the upcoming Run-2 searches. A full discussion of the presentation of

[16] Here, we ignore potential complications from the mediator width when the couplings are large.

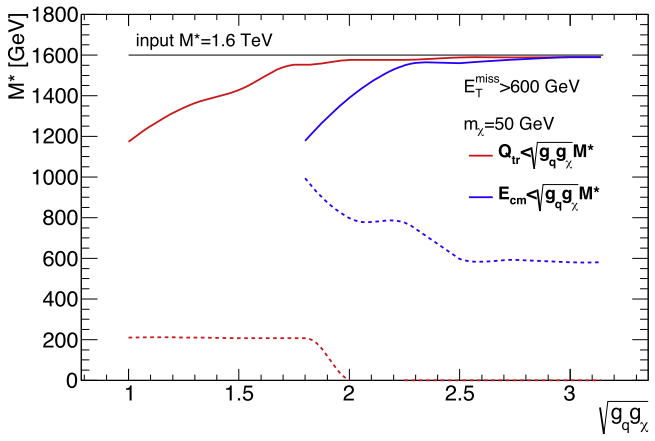

Fig. 69. 95% CL lower limits on the scale of the interaction of the D5 operator at 14 TeV, after the two truncation procedures. The procedure from [146] outlined in Section 5.1.2 is shown in blue, while the procedure from Refs. [7,145], described in Section 5.1.1 is shown in red. Only the region between the dashed and the solid lines is excluded. Even though the intersection between the two lines is not shown in this plot, it should be noted that no limit can be set anymore for sufficiently low couplings, whatever truncation method is used.

collider results in relation to other experiments is left to work beyond this Forum, where ATLAS, CMS, the theory community and the Direct and Indirect Detection communities are to be involved.

We divide the EFT operators in two categories: those that can be mapped to one or more UV-complete simplified models, such as those commonly used in LHC searches so far and detailed in [23], and those for which no UV completion is available to LHC experiments, such as those outlined in Section 3.2.

5.2.1. EFT benchmarks with corresponding simplified models

If a simplified model can be mapped to a given EFT, then the model's high-mediator-mass limit will converge to the EFT. A study of 14 TeV benchmarks for narrow resonances with $g_q = 0.25$ and $g_\chi = 1$ (see Section 2.1.1) shows that a mediator with a mass of at least 10 TeV fully reproduces the kinematics of a contact interaction and has no remaining dependence on the presence of a resonance. A comparison of the main kinematic variables for the *s*-channel vector mediator model with a width of 0.1 M_{med} is shown in Fig. 70.[17]

As already observed in Section 2.1.1, varying the DM mass changes the kinematics, both in the simplified model and in the EFT case. This can be seen in Fig. 71.

Based on these studies, the Forum recommends experimental collaborations to add one grid scan point at very high mediator mass (10 TeV) to the scan, for each of the DM masses for the *s*-channel simplified models described in Section 2. This will allow to reproduce the results of an equivalent contact interaction as a simple extension of the existing parameter scan.

It should be checked that the high-mass mediator case for the simplified model is correctly implemented

5.2.2. EFT benchmarks with no corresponding simplified models

Whenever a UV completion is not available, an EFT still captures a range of possible theories beyond the simplified models that we already consider. However, in the case of the dimension-7 operators detailed in Section 3.2 we can only roughly control how well the EFT approximation holds, as described in Section 3.2.4. Despite the fact that a propagator was introduced to motivate the truncation procedure for *s*-channel models, the prescription from Section 5.2.1 depends upon the simplified model to derive the energy scaling that is used for the comparison with the momentum transfer. The simple fact remains that the effective coupling of the operator – g/Λ^n – should not allow momentum flow $Q > \Lambda$ or $g > 4\pi$. Given our ignorance of the actual kinematics, the truncation procedure recommended for this purpose is the one described in Section 5.1.2, as it is independent from any UV completion details.

Because there is no UV completion, the parameter M_{cut} can be treated more freely than an explicit function of g and Λ. It makes sense to choose M_{cut} such that we identify the transition region where the EFT stops being a good description of UV complete theories. This can be done using the ratio R, which is defined as the fraction of events for which $\hat{s} > M_{cut}^2$. For large values of M_{cut}, no events are thrown away in the truncation procedure, and $R = 1$. As M_{cut} becomes smaller, eventually all events are thrown away in the truncation procedure, i.e. $R = 0$, and the EFT gives no exclusion limits for the chosen acceptance.

We propose a rough scan over M_{cut}, such that we find the values of M_{cut} for which R ranges from 0.1 to 1. The analysis can then perform a scan over several values of M_{cut}, and show the truncated limit for each one of them.

6. Evaluation of signal theoretical uncertainties

A comprehensive and careful assessment of signal theoretical uncertainties plays in general a more important role for the background estimations (especially when their evaluation is non-entirely data-driven) than it does for signal simulations. Nevertheless, also for signal samples theoretical uncertainties are relevant, and may become even dominant in certain regions of phase space.

The uncertainties on the factorization and renormalization scales are assessed by the experimental collaborations by varying the original scales of the process by factors of 0.5 and 2. The evaluation of the uncertainty on the choice of PDF follows the PDF4LHC recommendation [148] of considering the envelope of different PDF error sets, in order to account for the uncertainty on the various PDFs as well as the uncertainty on the choice of the central value PDF. The Forum has not discussed the uncertainties related to the merging of different samples, nor the uncertainty due to the choice of the modeling of the parton shower. This Chapter provides technical details on how scale and PDF uncertainties can be assessed for events generated with POWHEG and MadGraph5_aMC@NLO.

6.1. POWHEG

When using POWHEG [69–71], it is possible to study scale and PDF errors for the dark matter signals. A fast reweighting machinery is available in POWHEG-BOX that allows one to add, after each event, new weights according to different scale or PDF choices, without the need to regenerate all the events from scratch.

To enable this possibility, the variable `storeinfo_rwgt` should be set to 1 in the POWHEG input file when the events are generated for the first time.[18] After each event, a line starting with

```
#rwgt
```

[17] The use of a fixed width rather than the minimal width is exclusive of these plots.

[18] Notice that even if the variable is not present, by default it is set to 1.

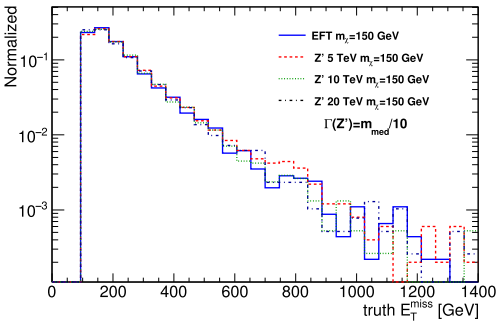

(a) $\not{E}_T$

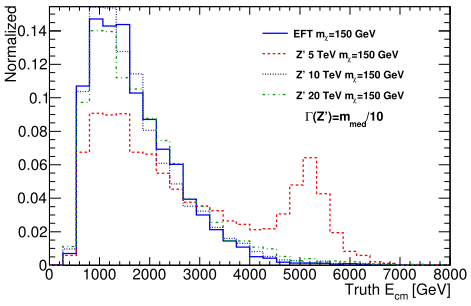

(b) Center of mass energy E_{cm}

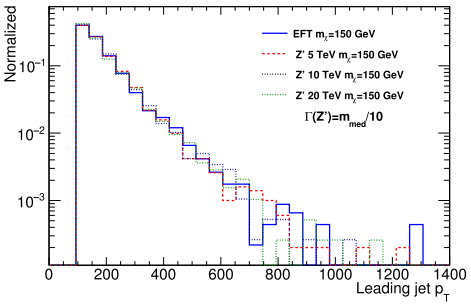

(c) Mediator transverse momentum

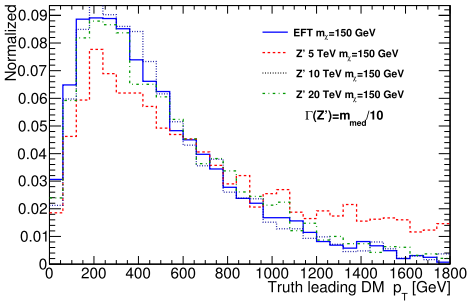

(d) Leading DM transverse momentum

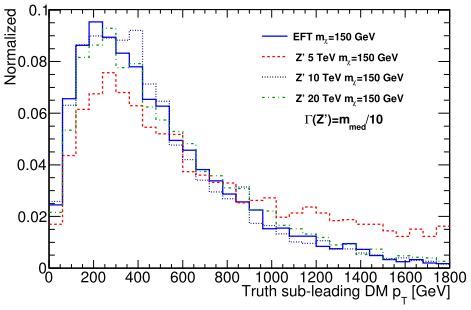

(e) DM transverse momentum (sub-leading)

Fig. 70. Comparison of the kinematic distributions at 14 TeV between a narrow *s*-channel mediator and the corresponding D5 contact operator, at generator level for a jet+$\not{E}_T$ signature.

is appended, containing the necessary information to generate extra weights. In order to obtain new weights, corresponding to different PDFs or scale choice, after an event file has been generated, a line

```
compute_rwgt 1
```

should be added in the input file along with the desired change in parameters. For instance, `renscfact` and `facscfact` allow one to study scale variations on the renormalization and factorization scales around a central value. By running the program again, a new event file will be generated, named `<OriginalName>-rwgt.lhe`, with one more line at the end of each event of the form

```
#new weight,renfact,facfact,pdf1,pdf2
```

followed by five numbers and a character string. The first of these numbers is the weight of that event with the new parameters chosen. By running in sequence the program in the reweighting mode, several weights can be added on the same file. Two remarks are in order.

- The file with new weights is always named `<OriginalName>-rwgt.lhe` hence care has to be taken to save it as `<OriginalName>.lhe` before each iteration of the reweighting procedure.
- Due to the complexity of the environment where the program is likely to be run, it is strongly suggested as a self-consistency check that the first reweighting is done keeping the initial parameters. If the new weights are not exactly the same as the original ones, then some inconsistency must have happened, or some file was probably corrupted.

It is possible to also have weights written in the version 3 Les Houches format. To do so, in the original run, at least the token

```
lhrwgt_id 'ID'
```

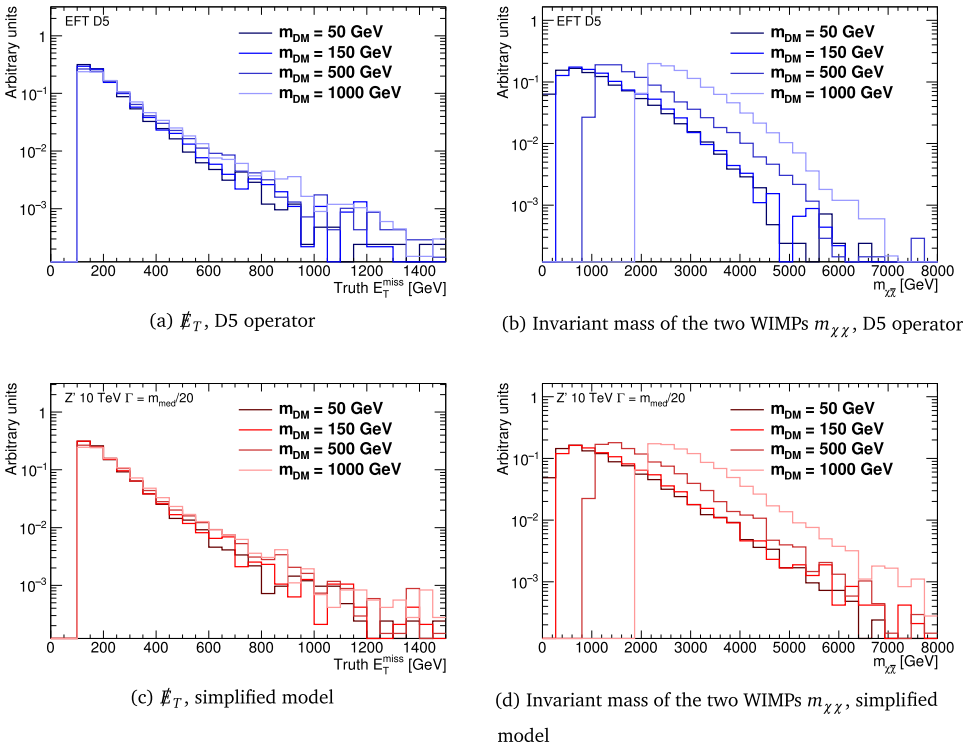

(a) $\not{E}_T$, D5 operator

(b) Invariant mass of the two WIMPs $m_{\chi\chi}$, D5 operator

(c) $\not{E}_T$, simplified model

(d) Invariant mass of the two WIMPs $m_{\chi\chi}$, simplified model

Fig. 71. Comparison of the kinematic distributions for a narrow *s*-channel mediator, at generator level for a jet+$\not{E}_T$ signature, for varying DM masses.

must be present. The reweighting procedure is the same as described above, but now each new run can be tagged by using a different value for the `lhrwgt_id` keyword. After each event, the following lines will appear:

```
<rwgt>
<wgt id='ID'>
<wgt id='ID1'>
</rwgt>
```

A more detailed explanation of what went into the computation of every single weight can be included in the `<header>` section of the event file by adding/changing the line

`lhrwgt_descr 'some info'`

in the input card, before each "reweighting" run is performed. Other useful keywords to group together different weights are `lhrwgt_group_name` and `lhrwgt_group_combine`.

More detailed information can be obtained by inspecting the document in `/Docs/V2-paper.pdf` under the common POWHEG-BOX-V2 directory.

6.2. *The SysCalc package in* MadGraph5_aMC@NLO

SysCalc is a post-processing package for parton-level events as obtained from leading-order calculations in MadGraph5_aMC@NLO. It can associate to each event a series of weights corresponding to the evaluation of a certain class of theoretical uncertainties. The event files in input and output are compliant with the Les Houches v3 format. For NLO calculations, PDF and scale uncertainties are instead evaluated automatically by setting corresponding instructions in the `run_card.dat` and no post-processing is needed (or possible).

The requirements of the package as inputs are :

- A systematics file (which can be generated by MadGraph 5 v. 1.6.0 or later) [75,149].
- The Pythia-PGS package (v. 2.2.0 or later) [150]. This is needed only in the case of matching scales variations.
- The availability of LHAPDF5 [151].
- A configuration file (i.e. a text file) specifying the parameters to be varied.

SysCalc supports all leading order computations generated in MadGraph5_aMC@NLO including fixed-order computation and matched–merged computation performed in the MLM scheme [152]. MadGraph5_aMC@NLO stores additional information inside the event in order to have access to all the information required to compute the convolution of the PDFs with the matrix element for the various supported systematics.

An example configuration file is as follows:

```
  # Central scale factors
scalefact:
0.5 1 2
# Scale correlation
# Special value -1: all combination (N**2)
# Special value -2: only correlated variation
# Otherwise list of index N*fac_index + ren_index
#   index starts at 0
scalecorrelation:
-1
# $\alpha_s$ emission scale factors
alpsfact:
0.5 1 2
# matching scales
matchscale:
30 60 120
# PDF sets and number of members (optional)
PDF:
CT10.LHgrid 53
MSTW2008nlo68cl.LHgrid
```

Without matching/merging, SysCalc is able to compute the variation of renormalization and factorization scale (parameter `scalefact`) and the change of PDFs. The variation of the scales

can be done in a correlated and/or uncorrelated way, basically following the value of the `scalecorrelation` parameter which can take the following values:

- -1 : to account for all N^2 combinations.
- -2 : to account only for the correlated variations.
- A set of positive values corresponding to the following entries (assuming *0.5, 1, 2* for the `scalefact` entry):

0: $\mu_F = \mu_F^{\rm orig}/2,\ \mu_R = \mu_R^{\rm orig}/2$
1: $\mu_F = \mu_F^{\rm orig}/2,\ \mu_R = \mu_R^{\rm orig}$
2: $\mu_F = \mu_F^{\rm orig}/2,\ \mu_R = \mu_R^{\rm orig} * 2$
3: $\mu_F = \mu_F^{\rm orig},\ \ \mu_R = \mu_R^{\rm orig}/2$
4: $\mu_F = \mu_F^{\rm orig},\ \ \mu_R = \mu_R^{\rm orig}$
5: $\mu_F = \mu_F^{\rm orig},\ \ \mu_R = \mu_R^{\rm orig} * 2$
6: $\mu_F = \mu_F^{\rm orig} * 2,\ \mu_R = \mu_R^{\rm orig}/2$
7: $\mu_F = \mu_F^{\rm orig} * 2,\ \mu_R = \mu_R^{\rm orig}$
8: $\mu_F = \mu_F^{\rm orig} * 2,\ \mu_R = \mu_R^{\rm orig} * 2$

Without correlation, the weight associated to the renormalization scale is the following:

$$\mathscr{W}_{\rm new}^{\mu_R} = \frac{\alpha_S^N(\Delta * \mu_R)}{\alpha_S^N(\mu_R)} * \mathscr{W}_{\rm orig}, \tag{49}$$

where Δ is the scale variation considered, $\mathscr{W}_{\rm orig}$ and $\mathscr{W}_{\rm new}$ are respectively the original/new weights associated to the event. N is the power in the strong coupling for the associated event (interference is not taken account on an event by event basis). The weight associated to the scaling of the factorization scale is:

$$\mathscr{W}_{\rm new}^{\mu_F} = \frac{f_{1,\rm orig}(x_1, \Delta * \mu_F) * f_{2,\rm orig}(x_2, \Delta * \mu_F)}{f_{1,\rm orig}(x_1, \mu_F) * f_{2,\rm orig}(x_2, \mu_F)} * \mathscr{W}_{\rm orig}, \tag{50}$$

where $f_{\rm i,orig}$ are the probabilities from the original PDF set associated to the incoming partons, which hold a proton momentum fraction x_1 and x_2 for the first and second beam respectively.

The variations for the PDF are given by the corresponding weights associated to the new PDF sets:

$$\mathscr{W}_{\rm new}^{\rm PDF} = \frac{f_{1,\rm new}(x_1, \mu_F) * f_{2,\rm new}(x_2, \mu_F)}{f_{1,\rm orig}(x_1, \mu_F) * f_{2,\rm orig}(x_2, \mu_F)} * \mathscr{W}_{\rm orig}, \tag{51}$$

where $f_{\rm i,new}$ is the new PDF probability associated to parton i.

In presence of matching, MadGraph5_aMC@NLO associates one history of radiation (initial and/or final state radiation) obtained by a k_T clustering algorithm, and calculates α_s at each vertex of the history to a scale given by the aforementioned clustering algorithm. Furthermore, MadGraph5_aMC@NLO reweights the PDF in a fashion similar to what a parton shower would do. SysCalc can perform the associated re-weighting (parameter `alpsfact`) by dividing and multiplying by the associated factor.

For each step in the history of the radiation (associated to a scale $\mu_i = k_{T,i}$), this corresponds to the following expression for a Final State Radiation (FSR):

$$\mathscr{W}_{\rm new}^{\rm FSR} = \frac{\alpha_s(\Delta * \mu_i)}{\alpha_s(\mu_i)} * \mathscr{W}_{\rm orig}, \tag{52}$$

and to the following expression for Initial State Radiation (ISR), associated to a scale μ_i and fraction of energy x_i:

$$\mathscr{W}_{\rm new}^{\rm ISR} = \frac{\alpha_s(\Delta * \mu_i)}{\alpha_s(\mu_i)} \frac{\frac{f_a(x_i, \Delta * \mu_i)}{f_b(x_i, \Delta * \mu_{i+1})}}{\frac{f_a(x_i, \mu_i)}{f_b(x_i, \mu_{i+1})}} * \mathscr{W}_{\rm orig}, \tag{53}$$

where μ_{i+1} is the scale of the next step in the (initial state) history of radiation.

SysCalc can include the weight associated to different merging scales in the MLM matching/merging mechanism (for output of the `pythia6` package or `pythia-pgs` package).

In that case, the parton shower does not veto any event according to the MLM algorithm, although in the output file the scale of the first emission is retained. Having this information, SysCalc can test each value of the specified matching scales under the `matchscale` parameter block. SysCalc will then test for each of the values specified in the parameter `matchscale` if the event passes the MLM criteria or not. If it does not, then a zero weight is associated to the event, while if it does, then a weight 1 is kept. As a reminder, those weights are the equivalent of having a (approximate) Sudakov form-factor and removing at the same time the double counting between the events belonging to different multiplicities.

Finally, we give an example of the SysCalc output which follows the LHEF v3 format. The following block appears in the header of the output file:

```
<header>
 <initrwgt>
  <weightgroup type="Central scale variation" combine="envelope">
    <weight id="1"> mur=0.5 muf=0.5 </weight>
    <weight id="2"> mur=1 muf=0.5 </weight>
    <weight id="3"> mur=2 muf=0.5 </weight>
    <weight id="4"> mur=0.5 muf=1 </weight>
    <weight id="5"> mur=1 muf=1 </weight>
    <weight id="6"> mur=2 muf=1 </weight>
    <weight id="7"> mur=0.5 muf=2 </weight>
    <weight id="8"> mur=1 muf=2 </weight>
    <weight id="9"> mur=2 muf=2 </weight>
  </weightgroup>
  <weightgroup type="Emission scale variation" combine=
  "envelope">
    <weight id="10"> alpsfact=0.5</weight>
    <weight id="11"> alpsfact=1</weight>
    <weight id="12"> alpsfact=2</weight>
  </weightgroup>
  <weightgroup type="CT10nlo.LHgrid" combine="hessian">
    <weight id="13">Member 0</weight>
    <weight id="14">Member 1</weight>
    <weight id="15">Member 2</weight>
    <weight id="16">Member 3</weight>
    ...
    <weight id="65">Member 52</weight>
  </weightgroup>
 </initrwgt>
</header>
```

For each event, the weights are then written as follows:

```
<rwgt>
 <wgt id="1">83214.7</wgt>
 <wgt id="2">61460</wgt>
 <wgt id="3">47241.9</wgt>
 <wgt id="4">101374</wgt>
 ...
 <wgt id="64">34893.5</wgt>
 <wgt id="65">41277</wgt>
</rwgt>
```

7. Conclusions

The ATLAS/CMS Dark Matter Forum concluded its work in June 2015. Its mandate was focused on identifying a prioritized, compact set of simplified model benchmarks to be used for the design of the early Run-2 LHC searches for $\not{E}_T$ +X final states. Its participants included many of the experimenters from both collaborations that are involved in these searches, as well as many of the theorists working actively on these models. This report has documented this basis set of models, as well as studies of the kinematically-distinct regions of the parameter space of the models, to aid the design of the searches. Table 9 summarizes the state of the art of the calculations, event generators, and tools that are available to the two LHC collaborations to simulate

Table 9
Summary table for available benchmark models considered within the works of this Forum. The results in this document have been obtained with the implementations in bold.

Benchmark models for ATLAS and CMS Run-2 DM searches			
Vector/axial vector mediator, *s*-channel (Section 2.1)			
Signature	State of the art calculation and tools	Implementation	References
jet + $\not{E}_T$	**NLO + PS (POWHEG, SVN r3059)**	[115,116]	[43,61,69–71]
	NLO+PS (*DMsimp* UFO + MadGraph5_aMC@NLO v2.3.0)	[113]	[75–77]
	NLO (MCFM v7.0)	Upon request	[41,114]
$W/Z/\gamma$ + $\not{E}_T$	**LO + PS (UFO + MadGraph5_aMC@NLO v2.2.3)**	[126]	[75–77]
	NLO+PS (*DMsimp* UFO + MadGraph5_aMC@NLO v2.3.0)	[113]	[75–77]
Scalar/pseudoscalar mediator, *s*-channel (Section 2.2)			
Signature	State of the art calculation and tools	Implementation	References
jet + $\not{E}_T$	**LO + PS, top loop (POWHEG, r3059)**	[117,118]	[43,61,69–71]
	LO+PS, top loop (*DMsimp* UFO + MadGraph5_aMC@NLO v.2.3.0)	[113]	[75–77,153]
	LO, top loop (MCFM v7.0)	Upon request	[41,114]
$W/Z/\gamma$ + $\not{E}_T$	**LO + PS (UFO + MadGraph5_aMC@NLO v2.2.3)**		[75–77]
$t\bar{t}, b\bar{b}$+ $\not{E}_T$	**LO + PS (UFO + MadGraph5_aMC@NLO v2.2.3)**	[127]	[75–77]
	NLO+PS (*DMsimp* UFO + MadGraph5_aMC@NLO v2.3.0)	[113]	[75–77]
Scalar mediator, *t*-channel (Section 2.3)			
Signature	State of the art calculation and tools	Implementation	References
jet(s) + $\not{E}_T$ (2-quark gens.)	LO+PS (UFO + MadGraph5_aMC@NLO v2.2.3)	[124]	[75–78]
jet(s) + $\not{E}_T$ (3-quark gens.)	**LO + PS (UFO + MadGraph5_aMC@NLO v2.2.3)**	[125]	[46,75–77]
$W/Z/\gamma$ + $\not{E}_T$	**LO + PS (UFO + MadGraph5_aMC@NLO v2.2.3)**	TBC	[46,75–77]
b + $\not{E}_T$	**LO + PS (UFO + MadGraph5_aMC@NLO v2.2.3)**	[128]	[75–77,87,88]
Specific simplified models with EW bosons (Section 3.1)			
Signature and model	State of the art calculation and tools	Implementation	References
Higgs + $\not{E}_T$, vector med.	**LO + PS (UFO + MadGraph5_aMC@NLO v2.2.3)**	[137]	[48,75–77,97]
Higgs + $\not{E}_T$, scalar med.	**LO + PS (UFO + MadGraph5_aMC@NLO v2.2.3)**	[137]	[48,75–77,97]
Higgs + $\not{E}_T$, 2HDM	**LO + PS (UFO + MadGraph5_aMC@NLO v2.2.3)**	[138]	[75–77,97]
Contact interaction operators with EW bosons (Section 3.1)			
Signature and model	State of the art calculation and tools	Implementation	References
$W/Z/\gamma$ + $\not{E}_T$, dim-7	**LO + PS (UFO + MadGraph5_aMC@NLO v2.2.3)**	[141]	[45,75–77,97–99]
Higgs + $\not{E}_T$, dim-4/dim-5	**LO + PS (UFO + MadGraph5_aMC@NLO v2.2.3)**	[154]	[47,48,75–77,97]
Higgs + $\not{E}_T$, dim-8	**LO + PS (UFO + MadGraph5_aMC@NLO v2.2.3)**	[137]	[47,48,75–77,97]

these models at the start of Run-2. It also describes some that are known to be under development as the report was finalized.

This document primarily presents studies related to simplified models. The presentation of results for EFT benchmark models is also discussed. The studies contained in this report are meant to highlight the use of EFTs as a benchmark that is complementary to simplified models, and to demonstrate how that collider results could be presented a function of the fraction of events that are valid within the contact interaction approximation.

A number of points remain to be developed beyond the scope of this Forum, in order to fully benefit from LHC searches in the global quest for Dark Matter. First and foremost, to accommodate the urgent need of a basis set of simplified models, this work has made many grounding assumptions, as stated in the introduction. Departures from these assumptions have not been fully explored. As a consequence, the list of models and implementations employed by the ATLAS and CMS collaborations for early LHC Run-2 searches is not meant to exhaust the range of possibilities for mediating processes, let alone cover all plausible models of collider dark matter production. Rather, it is hoped that others will continue the systematic exploration of the most generic possibilities for collider dark matter production, building upon the framework used in this report just as this report has relied heavily on the work of many others. This also applies to models that exist in literature but do not have an implementation yet: we hope that this work will further encourage the theory and generator community to improve the implementation of new models as well as the precision of the calculations of existing ones. The role of constraints on the mediator particles from direct past and present collider searches should also be developed further.

Furthermore, we see the need for broader discussion on the comparison of experimental results amongst collider and non-collider searches for particle dark matter. This point will have to be addressed before the presentation of Run-2 results: The uncertainties in the comparisons between experiments should be discussed and conveyed, so that the different results can be placed in their correct context, and so we can collectively build a fair and comprehensive picture of our understanding of particle dark matter.

Acknowledgments

The authors would like to thank Daniel Whiteson for helping in the review of this document. This research was supported by the Munich Institute for Astro- and Particle Physics (MIAPP) of the DFG cluster of excellence "Origin and Structure of the Universe". The authors would like to express a special thanks to the Mainz Institute for Theoretical Physics (MITP) for its hospitality and support. P. Pani wishes to thank the support of the Computing Infrastructure of Nikhef. In addition we thank CERN and acknowledge the support of: DOE and NSF (USA), including grant DE-SC0011726 for the preparation of this manuscript; SER, SNSF and Cantons of Bern and Geneva, Switzerland; MINECO, Spain; European Union, where the preparation of this manuscript is part of a project that has received funding from the European Research Council under the European Union's Horizon 2020 research and innovation program (grant agreement 679305); IN2P3-CNRS, CEA-DSM/IRFU, France; NSERC,

NRC, and CFI, Canada; INFN, Italy; FNRS and FWO, Belgium; STFC, United Kingdom; ARC, Australia; GRICES and FCT, Portugal; SRC, Sweden; BMBF, DFG, HGF, MPG and AvH Foundation, Germany; Austrian Academy of Sciences, Austria; MOE and UM, Malaysia; National Research Foundation and Ministry of Education, Science and Technology, Korea; MEXT and JSPS, Japan; FOM and NWO, Netherlands; CNPq and FAPESP, Brazil; Atomic Energy Commission, Pakistan; DNRF, DNSRC and Lundbeck Foundation, Denmark; Thailand Center of Excellence in Physics, Institute for the Promotion of Teaching Science and Technology, Special Task Force for Activating Research and National Science and Technology Development Agency, Thailand; MOST, Taiwan.

Appendix A. Additional models for dark matter searches

A.1. Models with a single top−quark + $\not{E}_T$

Many different theories predict final states with a single top and associated missing transverse momentum (monotop), some of them including dark matter candidates. A simplified model encompassing the processes leading to this phenomenology is described in Refs. [155–157], and is adopted as one of the benchmarks for Run 2 LHC searches.

The simplified model is constructed by imposing that the model Lagrangian respects the electroweak $SU(2)_L \times U(1)_Y$ gauge symmetry and by requiring minimality in terms of new states to supplement to the Standard Model fields. As a result, two monotop production mechanisms are possible. In the first case, the monotop system is constituted by an invisible (or long-lived with respect to detector distances) fermion χ and a top quark. It is produced as shown in the diagram of A.72(a) where a colored resonance φ lying in the triplet representation of $SU(3)_C$ decays into a top quark and a χ particle. In the second production mode, the monotop state is made of a top quark and a vector state V connected to a hidden sector so that it could decay invisibly into, e.g., a pair of dark matter particles as studied in [157]. The production proceeds via flavor-changing neutral interactions of the top quark with a quark of the first or second generation and the invisible V boson (see the diagrams of A.72(b) and (c)).

Resonant production. In this case, a colored 2/3-charged scalar (φ) is produced and decays into a top quark and a spin-1/2 invisible particle, χ. The dynamics of the new sector is described by the following Lagrangian:

$$\mathscr{L} = \left[\varphi \bar{d}^c \left[a^q_{SR} + b^q_{SR}\gamma_5\right] d + \varphi \bar{u}\left[a^{1/2}_{SR} + b^{1/2}_{SR}\gamma_5\right]\chi + \text{h.c.}\right], \qquad \text{(A.1)}$$

where u (d) stands for any up-type (down-type) quark, the notation SR refers to the monotop production mechanism via a scalar resonance and all flavor and color indices are understood for clarity.

In the notation of [156], the couplings of the new colored fields to down-type quarks are embedded into the 3×3 antisymmetric matrices a^q_{SR} (scalar couplings) and b^q_{SR} (pseudoscalar couplings) while those to the new fermion χ and one single up-type quark are given by the three-component vectors $a^{1/2}_{SR}$ and $b^{1/2}_{SR}$ in flavor space.

Under the form of Eq. (A.1), the Lagrangian is the one introduced in the original monotop search proposal [155]. It has been used by the CMS collaboration for Run I analyses after neglecting all pseudoscalar components of the couplings and adding the vector resonance case for which minimality requirements are difficult to accommodate [18]. In contrast, the study of Ref. [157] has imposed electroweak gauge invariance and required minimality. This enforces all new couplings to be right-handed so that

$$a^{1/2}_{SR} = b^{1/2}_{SR} = \frac{1}{2}y^*_s \qquad \text{and} \qquad a^q_{SR} = b^q_{SR} = \frac{1}{2}\lambda_s\ , \qquad \text{(A.2)}$$

where the objects y_s and λ_s are a tridimensional vector and a 3×3 matrix in flavor space respectively. This class of scenarios is the one that has been adopted by the ATLAS collaboration for its Run I monotop searches [12] and will be considered by both collaborations for Run II analyses.

The resulting model can be likened to the MSSM with an R-parity violating of a top squark to the Standard Model down-type quarks and an R-parity conserving interaction of a top quark and a top-squark to a neutralino.

Non-resonant production. For non-resonant monotop production, the monotop state is produced via flavor-changing neutral interactions of the top quark, a lighter up-type quark and a new invisible vector particle V. This is the only case considered, as having a new scalar would involve in particular a mixing with the SM Higgs boson and therefore a larger number of free parameters. The Lagrangian describing the dynamics of this non-resonant monotop production case is:

$$\mathscr{L} = \left[V_\mu \bar{u}\gamma^\mu\left[a^1_{FC} + b^1_{FC}\gamma_5\right]u + \text{h.c.}\right]\ , \qquad \text{(A.3)}$$

where the flavor and color indices are again understood for clarity. The strength of the interactions among these two states and a pair of up-type quarks is modeled via two 3×3 matrices in flavor space a^1_{FC} for the vector couplings and b^1_{FC} for the axial vector couplings, the FC subscript referring to the flavor-changing neutral monotop production mode and the (1) superscript to the vectorial nature of the invisible particle.

As for the resonant case, the Lagrangian of Eq. (A.3) is the one that has been used by CMS after reintroducing the scalar option for the invisible state and neglecting all pseudoscalar interactions [18]. As already mentioned, a simplified setup motivated by gauge invariance and minimality has been preferred so that, as shown in Ref. [157], we impose all interactions to involve right-handed quarks only,[19]

$$a^1_{FC} = b^1_{FC} = \frac{1}{2}a_R \qquad \text{(A.4)}$$

where a_R denotes a 3×3 matrix in flavor space. This implies the vector field to be an $SU(2)_L$ singlet.

Model parameters and assumptions. The models considered as benchmarks for the first LHC searches contain further assumptions in terms of the flavor structure of the model with respect to the Lagrangians of the previous subsection. In order to have an observable monotop signature at the LHC, the Lagrangians introduced above must include not too small couplings of the new particles to first and second generation quarks. For simplicity, we assumed that only channels enhanced by parton density effects will be considered, so that we fix

$$\begin{aligned} (a_R)_{13} = (a_R)_{31} = a\ , \\ (\lambda_s)_{12} = -(\lambda_s)_{21} = \lambda \qquad \text{and} \qquad (y_s)_3 = y\ , \end{aligned} \qquad \text{(A.5)}$$

all other elements of the matrices and vectors above being set to zero.

Implementation. In order to allow one for the Monte Carlo simulation of events relevant for the monotop production cases

[19] Ref. [158], which became public only after the conclusion of this Forum, introduces both left- and right-handed couplings.

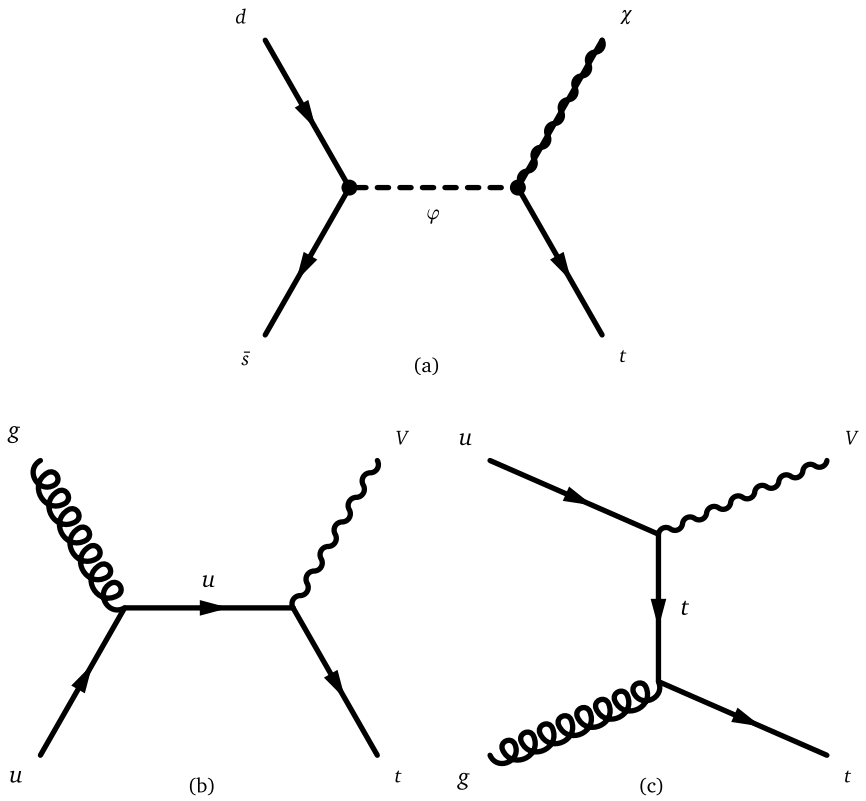

Fig. A.72. Feynman diagrams of leading order processes leading to monotop events: production of a colored scalar resonance φ decaying into a top quark and a spin-1/2 fermion χ (a), $s-$ (b) and t-channel (c) non resonant production of a top quark in association with a spin-1 boson V decaying invisibly.

described above, we consider the Lagrangian

$$\mathscr{L} = \left[aV_\mu \bar{u}\gamma^\mu P_R t + \lambda\varphi\bar{d}^c P_R s + y\varphi\bar{\chi}P_R t + \text{h.c.}\ , \right] \tag{A.6}$$

where P_R stands for the right-handed chirality projector and the new physics couplings are defined by the three parameters a, λ and y. We additionally include a coupling of the invisible vector boson V to a dark sector (represented by a fermion ψ) whose strength can be controlled through a parameter g_{DM},

$$\mathscr{L} = g_{DM} V_\mu \bar{\psi}\gamma^\mu\psi\ . \tag{A.7}$$

This ensures the option to make the V-boson effectively invisible by tuning g_{DM} respectively to a. We implement the entire model in the FeynRules package [76] so that the model can be exported to a UFO library [77] to be linked to MadGraph5_aMC@NLO [75] for event generation, following the approach outlined in [159].

A.2. Parameter scan

Under all the assumptions of the previous sections, the parameter space of the resonant model is defined by four quantities, namely the mass of the new scalar field φ, the mass of the invisible fermion χ and the strengths of the interactions of the scalar resonance with the monotop system y and with down-type quarks λ. One of both coupling parameters could however be traded with the width of the resonance.

The parameter space of the non-resonant model is defined by two parameters, namely the mass of the invisible state V and its flavor-changing neutral coupling to the up-type quarks a_R.

In the case of the non-resonant model, the invisible vector is connected to a hidden sector that could be, in its simplest form, parameterized by a new fermion [157]. This has effects on the width of the invisible V state.

A consensus between the ATLAS and CMS collaborations has been reached in the case of non-resonant monotop production. The results have been described above. In contrast, discussions in the context of resonant monotop production are still on-going. The related parameter space contains four parameters and must thus be further simplified for practical purposes. Several options are possible and a choice necessitates additional studies that will be achieved in a near future.

It has been verified that the kinematics do not depend on the width of the invisible state in the case where this width is at most 10% of the V-mass. This is illustrated in Fig. A.73, where we show the transverse-momentum spectra of the V-boson when it decays into a top-up final state and for different V-boson masses. The results are independent of the visible or invisible decay modes as we are only concerned with the kinematic properties of the invisible state.

A.3. Single top model implementation

Card files for MadGraph5_aMC@NLO are provided on the Forum Git repository [160] and correspond to the Lagrangian that has been implemented in FeynRules. Each coupling constant of the model can be set via the block `COUPX` of the parameter card. Its entries 1, 2 and 3 respectively correspond to the monotop-relevant parameters a, λ and y, while the width (and in particular the invisible partial width) of the V-boson can be tuned *via* the g_{DM} parameter to given in the entry 10 of the `COUPX` block.

The masses of the particles are set in the `MASS` block of the parameter card, the PDG codes of the new states being 32 (the vector state V), 1000006 (the φ colored resonance), 1000022 (the invisible fermion χ) and 1000023 (the fermion ψ connecting the V state to the dark sector). The width of the new vector has to be computed from all open tree-level decays (after fixing g_{DM} to a large value and setting the relevant entry to `Auto` in the `DECAY`

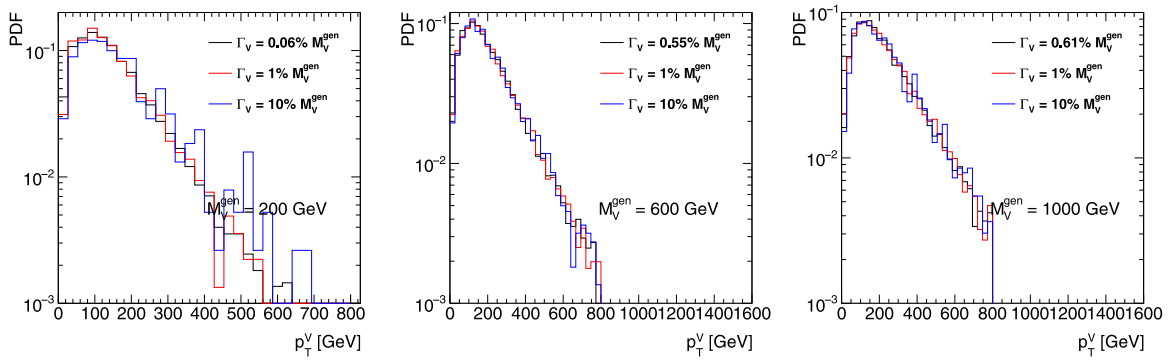

Fig. A.73. Distributions of the transverse momentum of the V boson in the case of the process $pp \to tV \to t(t\bar{u} + \text{c.c.})$. We have imposed that the V-boson is produced on-shell and have chosen its mass to be $m_V = 200$, 600 and 1000 GeV (left, central and right panels). We have considered three possible cases for the total width of the V-boson, which has been fixed to 0.61%, 0.1% and 10% of the mass.

block of the parameter card), while the way to calculate the width of the resonance ϕ is under discussion by both the ATLAS and CMS collaborations. The *chi* and *psi* fermions are taken stable so that their width vanishes.

A.4. Further W+$\not{E}_T$ models with possible cross-section enhancements

As pointed out in Ref. [67], the mono-W signature can probe the iso-spin violating interactions of dark matter with quarks. The relevant operator after the electroweak symmetry breaking is

$$\frac{1}{\Lambda^2}\overline{\chi}\gamma_\mu\chi\left(\overline{u}_L\gamma^\mu u_L + \xi\bar{d}_L\gamma^\mu d_L\right). \tag{A.8}$$

Here, we only keep the left-handed quarks because the right-handed quarks do not radiate a W-gauge boson from the weak interaction. As the LHC constrains the cutoff to higher values, it is also important to know the corresponding operators before the electroweak symmetry. At the dimension-six level, the following operator

$$\frac{c_6}{\Lambda^2}\overline{\chi}\gamma_\mu\chi\,\overline{Q}_L\gamma^\mu Q_L \tag{A.9}$$

conserves iso-spin and provides us $\xi = 1$ [67]. At the dimension-eight level, new operators appear to induce iso-spin violation and can be

$$\frac{c_8^d}{\Lambda^4}\overline{\chi}\gamma_\mu\chi\,(H\overline{Q}_L)\gamma^\mu(Q_L H^\dagger) + \frac{c_8^u}{\Lambda^4}\overline{\chi}\gamma_\mu\chi\,(\tilde{H}\overline{Q}_L)\gamma^\mu(Q_L\tilde{H}^\dagger). \tag{A.10}$$

After inputting the vacuum expectation value of the Higgs field, we have

$$\xi = \frac{c_6 + c_8^d\, v_{\rm EW}^2/2\Lambda^2}{c_6 + c_8^u\, v_{\rm EW}^2/2\Lambda^2}. \tag{A.11}$$

For a nonzero c_6 and $v_{\rm EW} \ll \Lambda$, the iso-spin violation effects are suppressed. On the other hand, the values of c_6, c_8^d and c_8^u depend on the UV-models.

There is one possible UV-model to obtain a zero value for c_6 and non-zero values for c_8^d and c_8^u. One can have the dark matter and the SM Higgs field charged under a new $U(1)'$ symmetry. There is a small mass mixing between SM Z-boson and the new Z' with a mixing angle of $\mathcal{O}(v_{\rm EW}^2/M_{Z'}^2)$. After integrating out Z', one has different effective dark matter couplings to u_L and d_L fields, which are proportional to their couplings to the Z boson. For this model, we have $c_6 = 0$ and

$$\xi = \frac{-\frac{1}{2} + \frac{1}{3}\sin^2\theta_W}{\frac{1}{2} - \frac{2}{3}\sin^2\theta_W} \approx -2.7 \tag{A.12}$$

and order of unity.

A.5. Simplified model corresponding to dimension-5 EFT operator

As an example of a simplified model corresponding to the dimension-5 EFT operator described in Section 3.2, we consider a Higgs portal with a scalar mediator. Models of this kind are among the most concise versions of simplified models that produce couplings of Dark Matter to pairs of gauge-bosons. Scalar fields may couple directly to pairs of electroweak gauge bosons, but must carry part of the electroweak vacuum expectation value. One may thus consider a simple model where Dark Matter couples to a scalar singlet mediator, which mixes with the fields in the Higgs sector.

$$L \subset \frac{1}{2}m_s S^2 + \lambda S^2|H|^2 + \lambda' S|H|^2 + yS\chi\overline{\chi} \tag{A.13}$$

where H is a field in the Higgs sector that contains part of the electroweak vacuum expectation value, S is a heavy scalar singlet and χ is a Dark Matter field. There is then an s-channel diagram where DM pairs couple to the singlet field S, which then mixes with a Higgs-sector field, and couples to W and Z bosons. This diagram contains 2 insertions of EW symmetry breaking fields, corresponding in form to the effective dimension-5 operator in Section 3.2.1.

A.6. Inert two-Higgs Doublet Model (IDM)

For most of the simplified models included in this report, the mass of the mediator and couplings/width are non-trivial parameters of the model. In these scenarios, we remain agnostic about the theory behind the dark matter sector and try to parameterize it in simple terms.

We have not addressed how to extend the simplified models to realistic and viable models which are consistent with the symmetries of the Standard Model. Simplified models often violate gauge invariance which is a crucial principle for building a consistent BSM model which incorporates SM together with new physics. For example, with a new heavy gauge vector boson mediating DM interactions, one needs not just the dark matter and its mediator, but also a mechanism which provides mass to this mediator in a gauge invariant way.

Considering both the simplified model and other elements necessary for a consistent theory is a next logical step. The authors of [161] term these Minimal Consistent Dark Matter (MCDM) models. MCDM models are at the same time still toy models that can be easily incorporated into a bigger BSM model and explored via complementary constraints from collider and direct/indirect DM search experiments as well as relic density constraints.

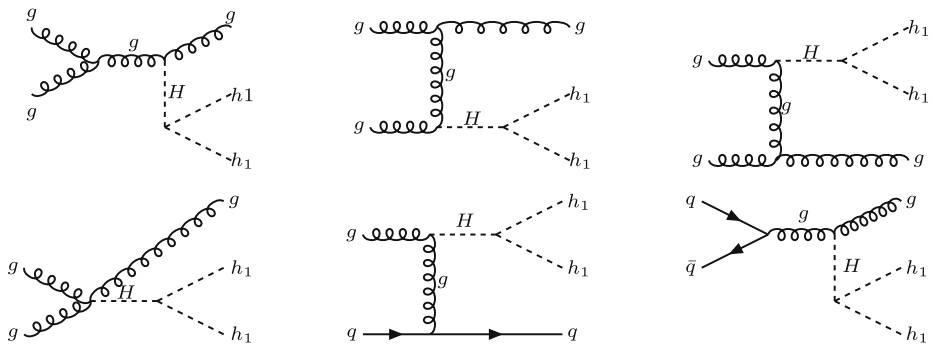

Fig. A.74. Feynman diagrams for $gg \to h_1 h_1 + g$ process contributing to mono-jet signature.
Source: Adapted from [161].

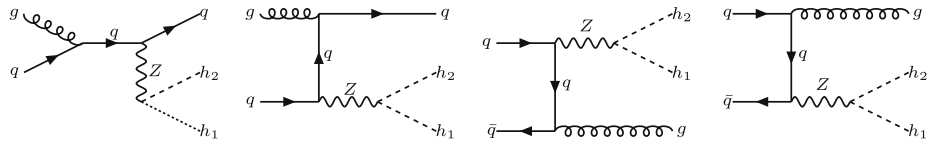

Fig. A.75. Feynman diagrams for $q\bar{q} \to h_1 h_2 + g$ ($gq \to h_1 h_2 + q$) process contributing to mono-jet signature.
Source: Adapted from [161].

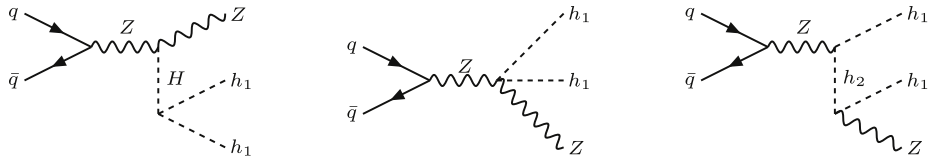

Fig. A.76. Feynman diagrams for $q\bar{q} \to h_1 h_1 + Z$ process contributing to mono-Z signature.
Source: Adapted from [161].

The idea of an inert Two-Higgs Doublet Model (IDM) was introduced more than 30 years ago in Ref [162]. The IDM was first proposed as a Dark Matter model in Ref. [163] and its phenomenology further studied in Refs. [14,161,164–173]. It is an extension of the SM with a second scalar doublet ϕ_2 with no direct coupling to fermions. This doublet has a discrete Z_2 symmetry, under which ϕ_2 is odd and all the other fields are even. The Lagrangian of the odd sector is,

$$\mathscr{L} = \frac{1}{2}(D_\mu \phi_2)^2 - V(\phi_1, \phi_2) \tag{A.14}$$

with the potential V containing mass terms and $\phi_1 - \phi_2$ interactions:

$$\begin{aligned} V = & -m_1^2(\phi_1^\dagger \phi_1) - m_2^2(\phi_2^\dagger \phi_2) + \lambda_1(\phi_1^\dagger \phi_1)^2 + \lambda_2(\phi_2^\dagger \phi_2)^2 \\ & + \lambda_3(\phi_2^\dagger \phi_2)(\phi_1^\dagger \phi_1) + \lambda_4(\phi_2^\dagger \phi_1)(\phi_1^\dagger \phi_2) \\ & + \frac{\lambda_5}{2}\left[(\phi_1^\dagger \phi_2)^2 + (\phi_2^\dagger \phi_1)^2\right], \end{aligned} \tag{A.15}$$

where ϕ_1 and ϕ_2 are SM and inert Higgs doublets respectively carrying the same hypercharge. These doublets can be parameterized as

$$\phi_1 = \frac{1}{\sqrt{2}}\begin{pmatrix} 0 \\ v + H \end{pmatrix} \qquad \phi_2 = \frac{1}{\sqrt{2}}\begin{pmatrix} \sqrt{2}h^+ \\ h_1 + ih_2 \end{pmatrix} \tag{A.16}$$

In addition to the SM, the IDM introduces four more degrees of freedom coming from the inert doublet in the form of a Z_2-odd charged scalar $h^\pm$ and two neutral Z_2-odd scalars h_1 and h_2. The lightest neutral scalar, h_1 is identified as the dark matter candidate. Aspects of the IDM collider phenomenology have been studied in [161,163,173–184]. Its LHC signatures include dileptons [179,184], trileptons [180] and multileptons [181] along with missing transverse energy, modifications of the Higgs branching ratios [173,182,183], as well as $\not{E}_T$ + jet, Z, and Higgs and $\not{E}_T$ + VBF signals (see Figs. A.74–A.79).

Based on the various LHC search channels, DM phenomenology issues and theoretical considerations, numerous works have proposed benchmark scenarios for the IDM, see e.g. [173,181] while a FeynRules implementation (including MadGraph, CalcHEP and micrOMEGAs model files) was provided in [181]. An updated analysis of the parameter space has recently been performed in Ref. [161].

The authors suggested to study mono-X signatures that are relevant to model-independent collider DM searches, and evaluated their rates presented below. They have implemented and cross-checked the IDM model into CalcHEP and micrOMEGAs, with an implementation publicly available on the HEPMDB database, including loop-induced *HHG* and $\gamma\gamma H$ models. They propose an additional set of benchmark points, mostly inspired by mono-*X* and VBF searches (Table A.10). Though the overall parameter space of IDM is 5-dimensional, once all relevant constraints are applied the parameter space relevant to a specific LHC signature typically reduces to 1–2 dimensional. In the mono-jet case, one can use two separate simplified models, a $gg \to h_1 h_1 + g$ process (via Higgs mediator) and a $qq \to h_1 h_2 + g (gq \to h_1 h_2 + q)$ process (through a Z-boson mediator) to capture the physics relevant to the search. The cross sections for the various mono-*X* and VBF signatures produced by this model are displayed in Fig. A.80.

Appendix B. Presentation of experimental results for reinterpretation

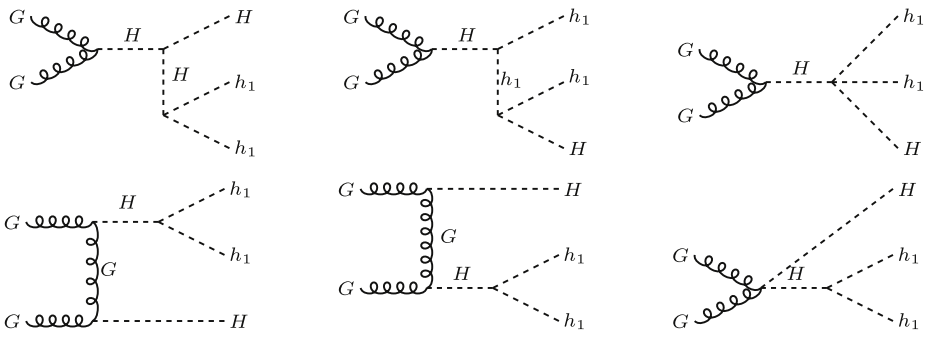

Fig. A.77. Feynman diagrams for $gg \to h_1 h_1 + H$ process contributing to mono-Higgs signature.
Source: Adapted from [161].

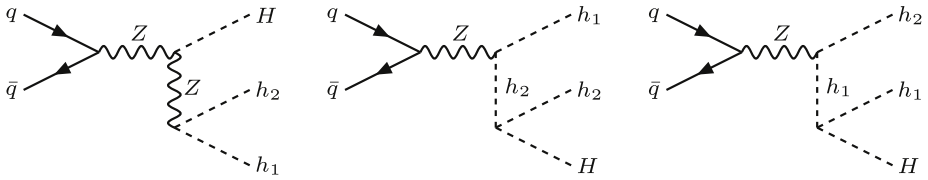

Fig. A.78. Feynman diagrams for $q\bar{q} \to h_1 h_2 + H$ process contributing to mono-Higgs signature.
Source: Adapted from [161].

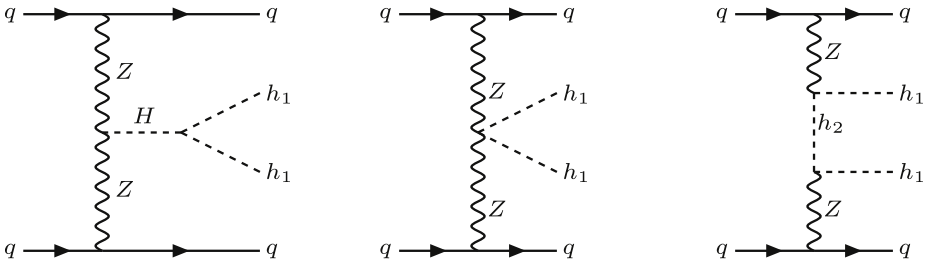

Fig. A.79. Diagrams for $qq \to qqh_1h_1$ DM production in vector boson fusion process.
Source: Adapted from [161].

Table A.10
Five benchmarks for IDM in $(M_{h_1}, M_{h_2}, M_{h_\pm}, \lambda_2, \lambda_{345})$ parameter space. We also present the corresponding relic density (Ωh^2), the spin-independent cross section for DM scattering on the proton (σ_{SI}), and the LHC cross section at 13 TeV for mono-jet process $pp \to h_1, h_1 + jet$ for $p_T^{jet} > 100$ GeV cut (σ_{LHC}).

BM	1	2	3	4	5
M_{h_1} (GeV)	48	53	70	82	120
M_{h_2} (GeV)	55	189	77	89	140
$M_{h_\pm}$ (GeV)	130	182	200	150	200
λ_2	0.8	1.0	1.1	0.9	1.0
λ_{345}	-0.010	-0.024	$+0.022$	-0.090	-0.100
Ωh^2	3.4×10^{-2}	8.1×10^{-2}	9.63×10^{-2}	1.5×10^{-2}	2.1×10^{-3}
σ_{SI} (pb)	2.3×10^{-10}	7.9×10^{-10}	5.1×10^{-10}	4.5×10^{-10}	2.6×10^{-9}
σ_{LHC} (fb)	1.7×10^{2}	7.7×10^{2}	4.3×10^{-2}	1.2×10^{-1}	2.3×10^{-2}

When collider searches present results with the recommended benchmarks, we suggest the following:

- Provide limits in collider language, on fundamental parameters of the interaction: the couplings and masses of particles in simplified model.
- Translate limits to non-collider language, for a range of assumptions, in order to convey a rough idea of the range of possibilities. The details of this point are left for work beyond the scope of this Forum.
- Provide all necessary material for theorists to reinterpret simplified model results as building blocks for more complete models (e.g. signal cutflows, acceptances, etc.). This point is detailed further in this appendix.
- Provide model-independent results in terms of limits on cross-section times efficiency times acceptance of new phenomena for all cases, but especially when EFTs are employed as benchmarks. This recommendation has been issued before: see Ref. [185] for detailed suggestions.

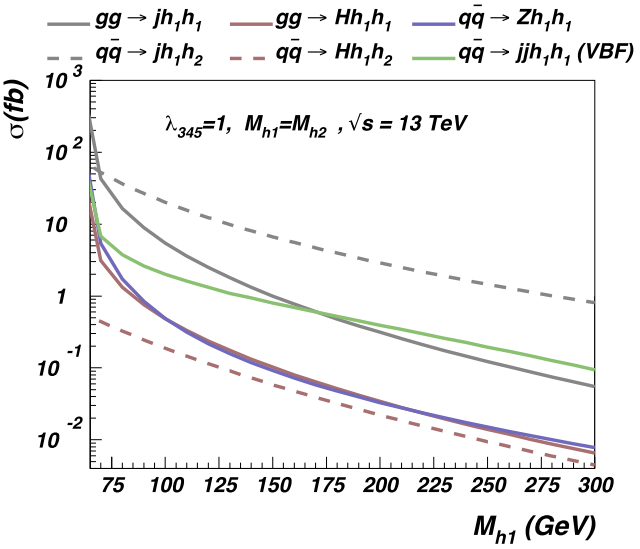

Fig. A.80. LHC cross section at 13 TeV for various signatures, from [161].

- Provide easily usable and clearly labeled results in a digitized format, e.g. [186] entries, ROOT histograms and macros or tables available on analysis public pages.

This appendix describes further considerations for reinterpretation and reimplementation of the analyses, as well as for the use of simplified model results directly given by the collaborations.

B.1. Reinterpretation of analyses

In the case of reinterpretation for models different than those provided by the experimental collaborations, the information needed primarily includes expected and observed exclusion lines along with their $\pm 1\sigma$ uncertainty, expected and observed upper limits in case of simplified models, efficiency maps and kinematic distributions as reported in the analysis. If the kinematics of the new model to be tested in the reinterpretation is similar to that of the original model provided by the collaboration, it will be straight-forward to rescale the results provided to match the new model cross-section using this information.

B.2. Reimplementation of analyses

One of the important developments in recent years is an active development of software codes [84,85,187–190] necessary for recasting analyses. The aim of these codes is to provide a public library of LHC analyses that have been reimplemented and validated, often by the collaborations themselves. Such libraries can then be used to analyze validity of a BSM scenario in a systematic and effective manner. The availability of public libraries further facilitates a unified framework and can lead to an organized and central structure to preserve LHC information long term. The reimplementation of an analysis consists of several stages. Typically, the analysis note is used as a basis for the implementation of the preselection and event selection cuts in the user analysis code within the recasting frameworks. Signal events are generated, and passed through a parameterized detector simulation using software such as Delphes or PGS [103,191]. The reconstructed objects are then analyzed using the code written in the previous step, and the results in terms of number of events are passed through a statistical analysis framework to compare with the backgrounds provided by the collaborations.

In order to be able to effectively use such codes, it is important to get a complete set of information from the collaborations.

For what concerns the generation of the models, it is desirable to have the following items as used by the collaborations:

- Monte Carlo generators: Monte Carlo generators along with the exact versions used to produce the event files should be listed.
- Production cross sections: The order of production cross sections (e.g. LO,NLO,NLL) as well as the codes which were used to compute them should be provided. Tables of reference cross sections for several values of particle masses are useful as well.
- Process Generation: Details of the generated process, detailing number of additional partons generated.
- LHE files: selected LHE files (detailing at least a few events if not the entire file) corresponding to the benchmarks listed in the analysis could also be made available in order to cross check process generation. Experimental collaborations may generate events on-the-fly without saving the intermediate LHE file; we advocate that the cross-check of process generation is straight-forward if this information is present, so we encourage the generation of a few selected benchmark points allowing for a LHE file to be saved. Special attention should be paid to list the parameters which change the production cross section or kinematics of the process e.g. mixing angles.
- Process cards: Process cards including PDF choices, details of matching algorithms and scales and details of process generation. If process cards are not available, the above items should be clearly identified.
- Model files: For models which are not already implemented in MadGraph5_aMC@NLO, the availability of the corresponding model files in the UFO format [77] is highly desired. This format details the exact notation used in the model and hence sets up a complete framework. In case MadGraph5_aMC@NLO is not used, enough information should be provided in order to clearly identify the underlying model used for interpretations and reproduce the generation.

The ATLAS/CMS Dark Matter Forum provides most of the information needed within its Git repository [59].

Efficiency maps and relevant kinematic distributions as reported in the analysis should be provided, in a digitized format with clearly specified units. If selection criteria cannot be easily simulated through parameterized detector simulation, the collaborations should provide the efficiency of such cuts. Overall reconstruction and identification efficiencies of physics objects are given as an input to the detector simulation software. It is thus very useful to get parameterized efficiencies for reconstructed objects (as a function of the rapidity η and/or transverse momentum p_T), along with the working points at which they were evaluated (e.g. loose, tight selection). Object definitions should be clearly identifiable. Digitized kinematic distributions are often necessary for the validation of the analysis so that the results from the collaboration are obtained, and so are tables containing the events passing each of the cuts.

The availability of digitized data and backgrounds is one of the primary requirements for fast and efficient recasting. Platforms such as HepData [186] can be used as a centralized repository; alternatively, analysis public pages and tables can be used for dissemination of results. Both data and Standard Model backgrounds should be provided in the form of binned histogram that can be interpolated if needed.

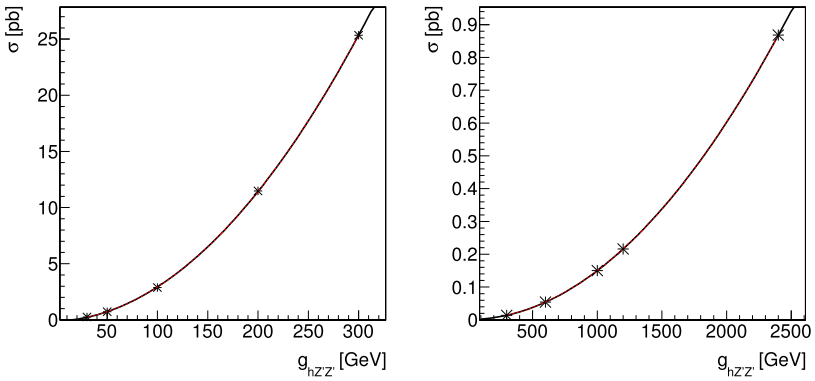

Fig. C.81. Cross section of the $pp \to H\chi\bar{\chi}$ process as a function of $g_{hZ'Z'}$ for $m_{Z'} = 100$ GeV (left) and $m_{Z'} = 1$ TeV (right). The fit functions are shown in the text.

A detailed description of the likelihood used in order to derive the limits from the comparison of data to signal plus background should be given. This can be inferred from the analysis documentation itself, however direct availability of the limit setting code as a workspace in RooStats or HistFitter [192] is highly desirable.

Finally, the collaborations can also provide an analysis code directly implemented in one of the public recasting codes detailed above. Such codes can be published via INSPIRE [193] in order to track versioning and citations.

B.3. Simplified model interpretations

Dark Matter searches at the LHC will include simplified model interpretations in their search results. These interpretations are simple and can be used for a survey of viability of parameter space. Codes such as [194–196] can make use of the simplified model results given in the form of 95% Confidence Level (CLs) upper limit or efficiency maps in order to test Beyond the Standard Model parameter space. As mentioned above, it will thus be extremely useful if the results are given in a digitized form that is easily usable by the theory community.

The parameter space of these models should be clearly specified. For example, for a simplified model containing dark matter mass m_χ, mediator mass M_{med} and couplings g_χ, g_q it will be very useful to have upper limits on the product of couplings $\sqrt{g_\chi g_q}$ or cross section times branching ratio as a function of m_χ, M_{med}. Limits on visible cross sections of the simplified models considered for interpretations should be made available.

The usage of simplified model results relies on interpolating between upper limit values. In order to facilitate the interpolation, regions where large variation of upper limits is observed should contain denser grid, if a uniform grid over the entire plane is not possible. For simplified model involving more than three parameters (two masses and product of couplings), slices of upper limits in the additional dimensions will be necessary for reinterpretation.

As already mentioned in the introduction to this Chapter, acceptance and efficiency maps for all the signal regions involved in the analysis should be made available. These results are not only useful for model testing using simplified models but also to validate implementation of the analysis. Information about the most sensitive signal regions as a function of new particle masses is also useful in order to determine the validity of approximate limit setting procedures commonly used by theorists.

Appendix C. Additional details and studies within the forum

Further information for baryonic Z' model

Cross-section scaling

The dependence of the cross section of the $pp \to H\chi\bar{\chi} + X$ process on $g_{hZ'Z'}$ is shown in Fig. C.81. The curves have been fit to second-order polynomials, where y is the cross-section and x is the coupling $g_{hZ'Z'}$.

For $m_{med} = 100$ GeV, the fit function is

$$y = -0.12 - 3.4 \times 10^{-3}x + 2.7 \times 10^{-4}x^2. \quad \text{(C.1)}$$

For $M_{\text{med}} = 1$ TeV, the fit function is:

$$y = 0.0012 - 2.4 \times 10^{-7}x + 1.5 \times 10^{-7}x^2. \quad \text{(C.2)}$$

References

[1] A. Birkedal, K. Matchev, M. Perelstein, Dark matter at colliders: A Model independent approach, Phys. Rev. D 70 (2004) 077701, http://dx.doi.org/10.1103/PhysRevD.70.077701, arXiv:hep-ph/0403004.

[2] J.L. Feng, S. Su, F. Takayama, Lower limit on dark matter production at the large hadron collider, Phys. Rev. Lett. 96 (2006) 151802, http://dx.doi.org/10.1103/PhysRevLett.96.151802, arXiv:hep-ph/0503117.

[3] F.J. Petriello, S. Quackenbush, K.M. Zurek, The Invisible Z' at the CERN LHC, Phys. Rev. D 77 (2008) 115020, http://dx.doi.org/10.1103/PhysRevD.77.115020, arXiv:0803.4005.

[4] M. Beltran, D. Hooper, E.W. Kolb, Z.A. Krusberg, T.M. Tait, Maverick dark matter at colliders, J. High Energy Phys. 1009 (2010) 037, http://dx.doi.org/10.1007/JHEP09(2010)037, arXiv:1002.4137.

[5] Y. Bai, P.J. Fox, R. Harnik, The Tevatron at the frontier of dark matter direct detection, J. High Energy Phys. 1012 (2010) 048, http://dx.doi.org/10.1007/JHEP12(2010)048, arXiv:1005.3797.

[6] T. Aaltonen, et al., A search for dark matter in events with one jet and missing transverse energy in $p\bar{p}$ collisions at $\sqrt{s}$ 1.96 TeV, Phys. Rev. Lett. 108 (2012) 211804, http://dx.doi.org/10.1103/PhysRevLett.108.211804, arXiv:1203.0742.

[7] G. Aad, et al., Search for new phenomena in final states with an energetic jet and large missing transverse momentum in pp collisions at $\sqrt{s} = 8$ TeV with the ATLAS detector, Eur. Phys. J. C 75 (7) (2015) 299, http://dx.doi.org/10.1140/epjc/s10052-015-3639-7, arXiv:1502.01518, Erratum; Eur. Phys. J. C 75 (9) (2015) 408.

[8] ATLAS Collaboration, Search for new phenomena in events with a photon and missing transverse momentum in pp collisions at $\sqrt{s} = 8$ TeV with the ATLAS detector, Phys. Rev. D 91 (2015) 012008.

[9] ATLAS Collaboration, Search for new particles in events with one lepton and missing transverse momentum in pp collisions at $\sqrt{s}$ = 8 TeV with the ATLAS detector, J. High Energy Phys. 1409 (2014) 037, http://dx.doi.org/10.1007/JHEP09(2014)037, arXiv:1407.7494.

[10] ATLAS Collaboration, Search for dark matter in events with a Z boson and missing transverse momentum in pp collisions at $\sqrt{s}$=8 TeV with the ATLAS detector, Phys. Rev. D 90 (2014) 012004, http://dx.doi.org/10.1103/PhysRevD.90.012004, arXiv:1404.0051.

[11] ATLAS Collaboration, Search for dark matter in events with a hadronically decaying W or Z boson and missing transverse momentum in pp collisions at $\sqrt{s} = 8$ TeV with the ATLAS detector, Phys. Rev. Lett. 112 (2014) 041802, http://dx.doi.org/10.1103/PhysRevLett.112.041802, arXiv:1309.4017.

[12] ATLAS Collaboration, Search for invisible particles produced in association with single-top-quarks in proton–proton collisions at $\sqrt{s}$ = 8 TeV with the ATLAS detector, Eur. Phys. J. C 75 (2015) 79, http://dx.doi.org/10.1140/epjc/s10052-014-3233-4, arXiv:1410.5404.

[13] ATLAS Collaboration, Search for dark matter in events with heavy quarks and missing transverse momentum in *pp* collisions with the ATLAS detector, Eur. Phys. J. C 75 (2015) 92, http://dx.doi.org/10.1140/epjc/s10052-015-3306-z, arXiv:1410.4031.

[14] ATLAS Collaboration, Sensitivity to WIMP dark matter in the final states containing jets and missing transverse momentum with the ATLAS detector at 14 TeV LHC, Tech. Rep. ATL-PHYS-PUB-2014-007, CERN, Geneva (2014). URL http://cds.cern.ch/record/1708859.

[15] CMS Collaboration, Search for dark matter extra dimensions and unparticles in monojet events in proton−proton collisions at $\sqrt{s}$ = 8 TeV, Eur. Phys. J. C 75 (2015) 235, http://dx.doi.org/10.1140/epjc/s10052-015-3451-4, arXiv:1408.3583.

[16] CMS Collaboration, Search for new phenomena in monophoton final states in proton–proton collisions at $\sqrt{s} = 8$ TeV, Phys. Lett. B 755 (2016) 102–124.

[17] CMS Collaboration, Search for physics beyond the standard model in final states with a lepton and missing transverse energy in proton–proton collisions at $\sqrt{s}$ TeV, Phys. Rev. D 91 (2015) 092005, http://dx.doi.org/10.1103/PhysRevD.91.092005, arXiv:1408.2745.

[18] CMS Collaboration, Search for monotop signatures in proton-proton collisions at $\sqrt{s}$ = 8 TeV, Phys. Rev. Lett. 114 (2015) 101801, http://dx.doi.org/10.1103/PhysRevLett.114.101801, arXiv:1410.1149.

[19] CMS Collaboration, Search for the production of dark matter in association with top-quark pairs in the single-lepton final state in proton-proton collisions at $\sqrt{s}$ = 8 TeV, J. High Energy Phys. 06 (2015) 121, http://dx.doi.org/10.1007/JHEP06(2015)121, arXiv:1504.03198.

[20] CMS Collaboration, Search for the production of dark matter in association with top quark pairs in the di-lepton final state in *pp* collisions at $\sqrt{s} = 8$ TeVCMS-PAS-B2G-13-004. URL http://cds.cern.ch/record/1697173.

[21] CMS Collaboration, Search for dark matter direct production using razor variables in events with two or more jets in *pp* collisions at 8 TeVCMS-PAS-EXO-14-004. URL http://cds.cern.ch/record/2002861.

[22] J. Goodman, M. Ibe, A. Rajaraman, W. Shepherd, T.M. Tait, et al., Constraints on light Majorana dark matter from colliders, Phys. Lett. B 695 (2011) 185–188, http://dx.doi.org/10.1016/j.physletb.2010.11.009, arXiv:1005.1286.

[23] J. Goodman, M. Ibe, A. Rajaraman, W. Shepherd, T.M. Tait, et al., Constraints on dark matter from colliders, Phys. Rev. D 82 (2010) 116010, http://dx.doi.org/10.1103/PhysRevD.82.116010, arXiv:1008.1783.

[24] I.M. Shoemaker, L. Vecchi, Unitarity and monojet bounds on models for DAMA, CoGeNT, and CRESST-II, Phys. Rev. D 86 (2012) 015023, http://dx.doi.org/10.1103/PhysRevD.86.015023, arXiv:1112.5457.

[25] J. Kopp, Collider limits on dark matter arXiv:1105.3248.

[26] P.J. Fox, R. Harnik, J. Kopp, Y. Tsai, LEP Shines light on dark matter, Phys. Rev. D 84 (2011) 014028, http://dx.doi.org/10.1103/PhysRevD.84.014028, arXiv:1103.0240.

[27] P.J. Fox, R. Harnik, J. Kopp, Y. Tsai, Missing energy signatures of dark matter at the LHC, Phys. Rev. D 85 (2012) 056011, http://dx.doi.org/10.1103/PhysRevD.85.056011, arXiv:1109.4398.

[28] G. Busoni, A. De Simone, E. Morgante, A. Riotto, On the validity of the effective field theory for dark matter searches at the LHC, Phys. Lett. B 728 (2014) 412–421, http://dx.doi.org/10.1016/j.physletb.2013.11.069, arXiv:1307.2253.

[29] J. Alwall, P. Schuster, N. Toro, Simplified models for a first characterization of new physics at the LHC, Phys. Rev. D 79 (2009) 075020, http://dx.doi.org/10.1103/PhysRevD.79.075020, arXiv:0810.3921.

[30] J. Goodman, W. Shepherd, LHC bounds on UV-complete models of dark matter arXiv:1111.2359.

[31] D. Alves, et al., Simplified models for LHC new physics searches, J. Phys. G 39 (2012) 105005, http://dx.doi.org/10.1088/0954-3899/39/10/105005, arXiv:1105.2838.

[32] H. An, X. Ji, L.-T. Wang, Light dark matter and Z' dark force at colliders, J. High Energy Phys. 1207 (2012) 182, http://dx.doi.org/10.1007/JHEP07(2012)182, arXiv:1202.2894.

[33] H. An, R. Huo, L.-T. Wang, Searching for low mass dark portal at the LHC, Phys. Dark Univ. 2 (2013) 50–57, http://dx.doi.org/10.1016/j.dark.2013.03.002, arXiv:1212.2221.

[34] A. DiFranzo, K.I. Nagao, A. Rajaraman, T.M.P. Tait, Simplified models for dark matter interacting with quarks, J. High Energy Phys. 1311 (2013) 014, http://dx.doi.org/10.1007/JHEP11(2013)014,10.1007/JHEP01(2014)162, arXiv:1308.2679.

[35] O. Buchmueller, M.J. Dolan, C. McCabe, Beyond effective field theory for dark matter searches at the LHC, J. High Energy Phys. 1401 (2014) 025, http://dx.doi.org/10.1007/JHEP01(2014)025, arXiv:1308.6799.

[36] Y. Bai, J. Berger, Fermion Portal Dark matter, J. High Energy Phys. 1311 (2013) 171, http://dx.doi.org/10.1007/JHEP11(2013)171, arXiv:1308.0612.

[37] Y. Bai, J. Berger, Lepton Portal Dark matter, J. High Energy Phys. 1408 (2014) 153, http://dx.doi.org/10.1007/JHEP08(2014)153, arXiv:1402.6696.

[38] H. An, L.-T. Wang, H. Zhang, Dark matter with *t*-channel mediator: a simple step beyond contact interaction, Phys. Rev. D 89 (2014) 115014, http://dx.doi.org/10.1103/PhysRevD.89.115014, arXiv:1308.0592.

[39] J. Abdallah, et al., Simplified models for dark matter and missing energy searches at the LHC arXiv:1409.2893.

[40] S.A. Malik, et al., Interplay and characterization of dark matter searches at colliders and in direct detection experiments, Phys. Dark Univ. 9-10 (2015) 51–58, http://dx.doi.org/10.1016/j.dark.2015.03.003, arXiv:1409.4075.

[41] P. Harris, V.V. Khoze, M. Spannowsky, C. Williams, Constraining dark sectors at colliders: Beyond the effective theory approach, Phys. Rev. D 91 (2015) 055009, http://dx.doi.org/10.1103/PhysRevD.91.055009, arXiv:1411.0535.

[42] M.R. Buckley, D. Feld, D. Goncalves, Scalar simplified models for dark matter, Phys. Rev. D 91 (2015) 015017, http://dx.doi.org/10.1103/PhysRevD.91.015017, arXiv:1410.6497.

[43] U. Haisch, E. Re, Simplified dark matter top-quark interactions at the LHC, J. High Energy Phys. 1506 (2015) 078, http://dx.doi.org/10.1007/JHEP06(2015)078, arXiv:1503.00691.

[44] Y. Bai, T.M. Tait, Searches with mono-leptons, Phys. Lett. B 723 (2013) 384–387, http://dx.doi.org/10.1016/j.physletb.2013.05.057, arXiv:1208.4361.

[45] L.M. Carpenter, A. Nelson, C. Shimmin, T.M. Tait, D. Whiteson, Collider searches for dark matter in events with a Z boson and missing energy, Phys. Rev. D 87 (2013) 074005, http://dx.doi.org/10.1103/PhysRevD.87.074005, arXiv:1212.3352.

[46] N.F. Bell, J.B. Dent, A.J. Galea, T.D. Jacques, L.M. Krauss, et al., Searching for dark matter at the LHC with a mono-Z, Phys. Rev. D 86 (2012) 096011, http://dx.doi.org/10.1103/PhysRevD.86.096011, arXiv:1209.0231.

[47] A.A. Petrov, W. Shepherd, Searching for dark matter at LHC with mono-Higgs production, Phys. Lett. B 730 (2014) 178–183, http://dx.doi.org/10.1016/j.physletb.2014.01.051, arXiv:1311.1511.

[48] L. Carpenter, A. DiFranzo, M. Mulhearn, C. Shimmin, S. Tulin, et al., Mono-Higgs-boson: A new collider probe of dark matter, Phys. Rev. D 89 (2014) 075017, http://dx.doi.org/10.1103/PhysRevD.89.075017, arXiv:1312.2592.

[49] J. Abdallah, et al., Simplified models for dark matter searches at the LHC, Phys. Dark Univ. 9-10 (2015) 8–23, http://dx.doi.org/10.1016/j.dark.2015.08.001, arXiv:1506.03116.

[50] G. Busoni, et al., Recommendations on presenting LHC searches for missing transverse energy signals using simplified *s*-channel models of dark matter arXiv:1603.04156.

[51] A. Albert, et al., Recommendations of the LHC Dark Matter Working Group: Comparing LHC searches for heavy mediators of dark matter production in visible and invisible decay channels arXiv:1703.05703.

[52] T. Abe, et al., LHC Dark Matter Working Group: Next-generation spin-0 dark matter models arXiv:1810.09420.

[53] D. Bauer, J. Buckley, M. Cahill-Rowley, R. Cotta, A. Drlica-Wagner, et al., Dark matter in the coming decade: Complementary paths to discovery and beyond, Phys. Dark Univ. 7-8 (2013) 16–23, http://dx.doi.org/10.1016/j.dark.2015.04.001, arXiv:1305.1605.

[54] R.S. Chivukula, H. Georgi, Composite technicolor standard model, Phys. Lett. B 188 (1987) 99, http://dx.doi.org/10.1016/0370-2693(87)90713-1.

[55] L. Hall, L. Randall, Weak scale effective supersymmetry, Phys. Rev. Lett. 65 (1990) 2939–2942, http://dx.doi.org/10.1103/PhysRevLett.65.2939.

[56] A. Buras, P. Gambino, M. Gorbahn, S. Jager, L. Silvestrini, Universal unitarity triangle and physics beyond the Standard Model, Phys. Lett. B 500 (2001) 161–167, http://dx.doi.org/10.1016/S0370-2693(01)00061-2, arXiv:hep-ph/0007085.

[57] G. D'Ambrosio, G. Giudice, G. Isidori, A. Strumia, Minimal Flavor Violation: An effective field theory approach, Nuclear Phys. B 645 (2002) 155–187, http://dx.doi.org/10.1016/S0550-3213(02)00836-2, arXiv:hep-ph/0207036.

[58] P. Agrawal, M. Blanke, K. Gemmler, Flavored dark matter beyond Minimal Flavor Violation, J. High Energy Phys. 1410 (2014) 72, http://dx.doi.org/10.1007/JHEP10(2014)072, arXiv:1405.6709.

[59] Git repository for model, input and parameter cards for models considered in the ATLAS/CMS Dark Matter Forum studies, https://doi.org/10.5281/zenodo.3260943, [Online; accessed 28-June-2019] (2015).

[60] O. Buchmueller, M.J. Dolan, S.A. Malik, C. McCabe, Characterising dark matter searches at colliders and direct detection experiments: Vector mediators, J. High Energy Phys. 1501 (2015) 037, http://dx.doi.org/10.1007/JHEP01(2015)037, arXiv:1407.8257.

[61] U. Haisch, F. Kahlhoefer, E. Re, QCD Effects in mono-jet searches for dark matter, J. High Energy Phys. 1312 (2013) 007, http://dx.doi.org/10.1007/JHEP12(2013)007, arXiv:1310.4491.

[62] T. Sjöstrand, S. Mrenna, P.Z. Skands, A brief introduction to PYTHIA 8.1, Comput. Phys. Comm. 178 (2008) 852–867, http://dx.doi.org/10.1016/j.cpc.2008.01.036, arXiv:0710.3820.

[63] Y. Bai, J. Bourbeau, T. Lin, Dark matter searches with a mono-Z' jet, J. High Energy Phys. 06 (2015) 205, http://dx.doi.org/10.1007/JHEP06(2015)205, arXiv:1504.01395.

[64] M. Chala, F. Kahlhoefer, M. McCullough, G. Nardini, K. Schmidt-Hoberg, Constraining dark sectors with Monojets and Dijets, J. High Energy Phys. 07 (2015) 089, http://dx.doi.org/10.1007/JHEP07(2015)089, arXiv:1503.05916.

[65] N. Zhou, D. Berge, D. Whiteson, Mono-everything: combined limits on dark matter production at colliders from multiple final states, Phys. Rev. D 87 (2013) 095013, http://dx.doi.org/10.1103/PhysRevD.87.095013, arXiv:1302.3619.

[66] Y. Gershtein, F. Petriello, S. Quackenbush, K.M. Zurek, Discovering hidden sectors with mono-photon Z'o searches, Phys. Rev. D 78 (2008) 095002, http://dx.doi.org/10.1103/PhysRevD.78.095002, arXiv:0809.2849.

[67] N.F. Bell, Y. Cai, J.B. Dent, R.K. Leane, T.J. Weiler, Dark matter at the LHC: Effective field theories and gauge invariance, Phys. Rev. D 92 (5) (2015) 053008, http://dx.doi.org/10.1103/PhysRevD.92.053008, arXiv:1503.07874.

[68] K. Hamaguchi, S.P. Liew, T. Moroi, Y. Yamamoto, Isospin-violating dark matter with colored mediators, J. High Energy Phys. 1405 (2014) 086, http://dx.doi.org/10.1007/JHEP05(2014)086, arXiv:1403.0324.

[69] S. Alioli, P. Nason, C. Oleari, E. Re, A general framework for implementing NLO calculations in shower Monte Carlo programs: the POWHEG BOX, J. High Energy Phys. 1006 (2010) 043, http://dx.doi.org/10.1007/JHEP06(2010)043, arXiv:1002.2581.

[70] P. Nason, A new method for combining NLO QCD with shower Monte Carlo algorithms, J. High Energy Phys. 0411 (2004) 040, http://dx.doi.org/10.1088/1126-6708/2004/11/040, arXiv:hep-ph/0409146.

[71] S. Frixione, P. Nason, C. Oleari, Matching NLO QCD computations with parton shower simulations: the POWHEG method, J. High Energy Phys. 0711 (2007) 070, http://dx.doi.org/10.1088/1126-6708/2007/11/070, arXiv:0709.2092, * Temporary entry *.

[72] C. Arina, E. Del Nobile, P. Panci, Dark matter with pseudoscalar-mediated interactions explains the DAMA signal and the Galactic Center excess, Phys. Rev. Lett. 114 (2015) 011301, http://dx.doi.org/10.1103/PhysRevLett.114.011301, arXiv:1406.5542.

[73] U. Haisch, A. Hibbs, E. Re, Determining the structure of dark-matter couplings at the LHC, Phys. Rev. D 89 (2014) 034009, http://dx.doi.org/10.1103/PhysRevD.89.034009, arXiv:1311.7131.

[74] H.M. Lee, M. Park, V. Sanz, Interplay between Fermi gamma-ray lines and collider searches, J. High Energy Phys. 1303 (2013) 052, http://dx.doi.org/10.1007/JHEP03(2013)052, arXiv:1212.5647.

[75] J. Alwall, R. Frederix, S. Frixione, V. Hirschi, F. Maltoni, et al., The automated computation of tree-level and next-to-leading order differential cross sections, and their matching to parton shower simulations, J. High Energy Phys. 1407 (2014) 079, http://dx.doi.org/10.1007/JHEP07(2014)079, arXiv:1405.0301.

[76] A. Alloul, N.D. Christensen, C. Degrande, C. Duhr, B. Fuks, FeynRules 2.0 - a complete toolbox for tree-level phenomenology, Comput. Phys. Comm. 185 (2014) 2250–2300, arXiv:1310.1921.

[77] C. Degrande, C. Duhr, B. Fuks, D. Grellscheid, O. Mattelaer, et al., UFO - The Universal FeynRules Output, Comput. Phys. Comm. 183 (2012) 1201–1214, http://dx.doi.org/10.1016/j.cpc.2012.01.022, arXiv:1108.2040.

[78] M. Papucci, A. Vichi, K.M. Zurek, Monojet versus the rest of the world I: t-channel models, J. High Energy Phys. 1411 (2014) 024, http://dx.doi.org/10.1007/JHEP11(2014)024, arXiv:1402.2285.

[79] S. Chang, R. Edezhath, J. Hutchinson, M. Luty, Effective WIMPs, Phys. Rev. D 89 (2014) 015011, http://dx.doi.org/10.1103/PhysRevD.89.015011, arXiv:1307.8120.

[80] G. Busoni, A. De Simone, T. Jacques, E. Morgante, A. Riotto, On the validity of the effective field theory for dark matter searches at the LHC part III: analysis for the t-channel, J. Cosmol. Astropart. Phys. 1409 (2014) 022, http://dx.doi.org/10.1088/1475-7516/2014/09/022, arXiv:1405.3101.

[81] F. Maltoni, A. Martini, K. Mawatari, B. Oexl, Signals of a superlight gravitino at the LHC, J. High Energy Phys. 1504 (2015) 021, http://dx.doi.org/10.1007/JHEP04(2015)021, arXiv:1502.01637.

[82] P. de Aquino, F. Maltoni, K. Mawatari, B. Oexl, Light gravitino production in association with gluinos at the LHC, J. High Energy Phys. 1210 (2012) 008, http://dx.doi.org/10.1007/JHEP10(2012)008, arXiv:1206.7098.

[83] J. Alwall, S. de Visscher, F. Maltoni, QCD Radiation in the production of heavy colored particles at the LHC, J. High Energy Phys. 0902 (2009) 017, http://dx.doi.org/10.1088/1126-6708/2009/02/017, arXiv:0810.5350.

[84] E. Conte, B. Dumont, B. Fuks, C. Wymant, Designing and recasting LHC analyses with MadAnalysis 5, Eur. Phys. J. C 74 (2014) 3103, http://dx.doi.org/10.1140/epjc/s10052-014-3103-0, arXiv:1405.3982.

[85] B. Dumont, B. Fuks, S. Kraml, S. Bein, G. Chalons, et al., Toward a public analysis database for LHC new physics searches using MADANALYSIS 5, Eur. Phys. J. C 75 (2015) 56, http://dx.doi.org/10.1140/epjc/s10052-014-3242-3, arXiv:1407.3278.

[86] E. Conte, B. Fuks, G. Serret, MadAnalysis 5, a user-friendly framework for collider phenomenology, Comput. Phys. Comm. 184 (2013) 222–256, http://dx.doi.org/10.1016/j.cpc.2012.09.009, arXiv:1206.1599.

[87] T. Lin, E.W. Kolb, L.-T. Wang, Probing dark matter couplings to top and bottom quarks at the LHC, Phys. Rev. D 88 (2013) 063510, http://dx.doi.org/10.1103/PhysRevD.88.063510, arXiv:1303.6638.

[88] P. Agrawal, B. Batell, D. Hooper, T. Lin, Flavored dark matter and the Galactic Center gamma-ray excess, Phys. Rev. D 90 (2014) 063512, http://dx.doi.org/10.1103/PhysRevD.90.063512, arXiv:1404.1373.

[89] T. Daylan, D.P. Finkbeiner, D. Hooper, T. Linden, S.K.N. Portillo, N.L. Rodd, T.R. Slatyer, The characterization of the gamma-ray signal from the central Milky Way: A case for annihilating dark matter, Phys. Dark Univ. 12 (2016) 1–23, http://dx.doi.org/10.1016/j.dark.2015.12.005, arXiv:1402.6703.

[90] F. Calore, I. Cholis, C. Weniger, Background model systematics for the Fermi GeV excess, J. Cosmol. Astropart. Phys. 1503 (2015) 038, http://dx.doi.org/10.1088/1475-7516/2015/03/038, arXiv:1409.0042.

[91] A. Kumar, S. Tulin, Top-flavored dark matter and the forward-backward asymmetry, Phys. Rev. D 87 (9) (2013) 095006, http://dx.doi.org/10.1103/PhysRevD.87.095006, arXiv:1303.0332.

[92] B. Batell, T. Lin, L.-T. Wang, Flavored Dark Matter And R-parity violation, J. High Energy Phys. 1401 (2014) 075, http://dx.doi.org/10.1007/JHEP01(2014)075, arXiv:1309.4462.

[93] C. Kilic, M.D. Klimek, J.-H. Yu, Signatures of top flavored dark matter, Phys. Rev. D 91 (5) (2015) 054036, http://dx.doi.org/10.1103/PhysRevD.91.054036, arXiv:1501.02202.

[94] H.M. Lee, M. Park, V. Sanz, Gravity-mediated (or composite) Dark Matter, Eur. Phys. J. C 74 (2014) 2715, http://dx.doi.org/10.1140/epjc/s10052-014-2715-8, arXiv:1306.4107.

[95] H.M. Lee, M. Park, V. Sanz, Gravity-mediated (or composite) dark matter confronts astrophysical data, J. High Energy Phys. 1405 (2014) 063, http://dx.doi.org/10.1007/JHEP05(2014)063, arXiv:1401.5301.

[96] D.Y. Bardin, S.M. Bilenky, W. Beenakker, F.A. Berends, W.L. van Neerven, S.C. Van der Marck, G. Burgers, W.F.L. Hollik, T. Riemann, M. Sachwitz, Z Line shape, in: Workshop on Z Physics At LEP1 : General Meetings, Vol. 1 : StandArd Physics, 1989, p. 43, URL http://cds.cern.ch/record/199969.

[97] A. Berlin, T. Lin, L.-T. Wang, Mono-Higgs detection of dark matter at the LHC, J. High Energy Phys. 1406 (2014) 078, http://dx.doi.org/10.1007/JHEP06(2014)078, arXiv:1402.7074.

[98] R. Cotta, J. Hewett, M. Le, T. Rizzo, Bounds on dark matter interactions with electroweak gauge bosons, Phys. Rev. D 88 (2013) 116009, http://dx.doi.org/10.1103/PhysRevD.88.116009, arXiv:1210.0525.

[99] A. Crivellin, U. Haisch, A. Hibbs, LHC constraints on gauge boson couplings to dark matter, Phys. Rev. D 91 (2015) 074028, http://dx.doi.org/10.1103/PhysRevD.91.074028, arXiv:1501.00907.

[100] A. Nelson, L.M. Carpenter, R. Cotta, A. Johnstone, D. Whiteson, Confronting the Fermi Line with LHC data: an effective theory of dark matter interaction with photons, Phys. Rev. D 89 (2014) 056011, http://dx.doi.org/10.1103/PhysRevD.89.056011, arXiv:1307.5064.

[101] D. O'Connell, M.J. Ramsey-Musolf, M.B. Wise, Minimal extension of the Standard Model scalar sector, Phys. Rev. D 75 (2007) 037701, http://dx.doi.org/10.1103/PhysRevD.75.037701, arXiv:hep-ph/0611014.

[102] N. Craig, J. Galloway, S. Thomas, Searching for signs of the Second Higgs Doublet arXiv:1305.2424.

[103] J. de Favereau, et al., DELPHES 3, a modular framework for fast simulation of a generic collider experiment, J. High Energy Phys. 1402 (2014) 057, http://dx.doi.org/10.1007/JHEP02(2014)057, arXiv:1307.6346.

[104] A. Djouadi, A. Falkowski, Y. Mambrini, J. Quevillon, Direct detection of Higgs-Portal dark matter at the LHC, Eur. Phys. J. C 73 (2013) 2455, http://dx.doi.org/10.1140/epjc/s10052-013-2455-1, arXiv:1205.3169.

[105] N. Weiner, I. Yavin, How dark are Majorana WIMPs? signals from MiDM and Rayleigh dark matter, Phys. Rev. D 86 (2012) 075021, http://dx.doi.org/10.1103/PhysRevD.86.075021, arXiv:1206.2910.

[106] N. Weiner, I. Yavin, UV completions of magnetic inelastic and Rayleigh dark matter for the Fermi Line(s), Phys. Rev. D 87 (2013) 023523, http://dx.doi.org/10.1103/PhysRevD.87.023523, arXiv:1209.1093.

[107] J. Liu, B. Shuve, N. Weiner, I. Yavin, Looking for new charged states at the LHC: Signatures of magnetic and Rayleigh dark matter, J. High Energy Phys. 1307 (2013) 144, http://dx.doi.org/10.1007/JHEP07(2013)144, arXiv:1303.4404.

[108] U. Haisch, F. Kahlhoefer, J. Unwin, The impact of heavy-quark loops on LHC dark matter searches, J. High Energy Phys. 1307 (2013) 125, http://dx.doi.org/10.1007/JHEP07(2013)125, arXiv:1208.4605.

[109] M. Bahr, S. Gieseke, M. Gigg, D. Grellscheid, K. Hamilton, et al., Herwig++ physics and manual, Eur. Phys. J. C 58 (2008) 639–707, http://dx.doi.org/10.1140/epjc/s10052-008-0798-9, arXiv:0803.0883.

[110] G. Corcella, I. Knowles, G. Marchesini, S. Moretti, K. Odagiri, et al., HERWIG 6.5 release note arXiv:hep-ph/0210213.

[111] G. Corcella, et al., HERWIG 6: An event generator for hadron emission reactions with interfering gluons (including supersymmetric processes), J. High Energy Phys. 0101 (2001) 010, http://dx.doi.org/10.1088/1126-6708/2001/01/010, arXiv:hep-ph/0011363.

[112] G. Marchesini, B. Webber, G. Abbiendi, I. Knowles, M. Seymour, L. Stanco, HERWIG 5.1 - a monte carlo event generator for simulating hadron emission reactions with interfering gluons, Comput. Phys. Comm. 67 (3) (1992) 465–508, http://dx.doi.org/10.1016/0010-4655(92)90055-4, http://www.sciencedirect.com/science/article/pii/0010465592900554.

[113] M. Backovic, M. Krämer, F. Maltoni, A. Martini, K. Mawatari, M. Pellen, Higher-order QCD predictions for dark matter production at the LHC in simplified models with s-channel mediators, Eur. Phys. J. C 75 (10) (2015) 482, http://dx.doi.org/10.1140/epjc/s10052-015-3700-6, arXiv:1508.05327.

[114] P.J. Fox, C. Williams, Next-to-leading order predictions for dark matter production at hadron colliders, Phys. Rev. D 87 (2013) 054030, http://dx.doi.org/10.1103/PhysRevD.87.054030, arXiv:1211.6390.

[115] Git repository for POWHEG input card for model with *s*-channel exchange of axial vector mediator, https://github.com/LHC-DMWG/model-repository/tree/master/models/Monojet_DMA, [Online; accessed 08-May-2019] (2015). http://dx.doi.org/10.5281/zenodo.3260943.

[116] Git repository for POWHEG input card for model with *s*-channel exchange of vector mediator, https://github.com/LHC-DMWG/model-repository/tree/master/models/Monojet_DMV, [Online; accessed 08-May-2019] (2015). http://dx.doi.org/10.5281/zenodo.3260943.

[117] Git repository for POWHEG input card for model with *s*-channel exchange of scalar mediator, https://github.com/LHC-DMWG/model-repository/tree/master/models/Monojet_DMS_tLoop, [Online; accessed 08-May-2019] (2015). http://dx.doi.org/10.5281/zenodo.3260943.

[118] Git repository for POWHEG input card for model with *s*-channel exchange of pseudo-scalar mediator, coupling to the quarks through a top loop, https://github.com/LHC-DMWG/model-repository/tree/master/models/Monojet_DMP_tloop, [Online; accessed 08-May-2019] (2015). http://dx.doi.org/10.5281/zenodo.3260943.

[119] T. Sjöstrand, S. Ask, J.R. Christiansen, R. Corke, N. Desai, et al., An introduction to PYTHIA 8.2, Comput. Phys. Comm. 191 (2015) 159–177, http://dx.doi.org/10.1016/j.cpc.2015.01.024, arXiv:1410.3012.

[120] S. Hoeche, S. Kuttimalai, S. Schumann, F. Siegert, Beyond Standard Model calculations with Sherpa, Eur. Phys. J. C 75 (3) (2015) 135, http://dx.doi.org/10.1140/epjc/s10052-015-3338-4, arXiv:1412.6478.

[121] R. Frederix, S. Frixione, Merging meets matching in MC@NLO, J. High Energy Phys. 1212 (2012) 061, http://dx.doi.org/10.1007/JHEP12(2012)061, arXiv:1209.6215.

[122] J. Alwall, et al., Comparative study of various algorithms for the merging of parton showers and matrix elements in hadronic collisions, Eur. Phys. J. C 53 (2008) 473–500, http://dx.doi.org/10.1140/epjc/s10052-007-0490-5, arXiv:0706.2569.

[123] L. Lonnblad, S. Prestel, Matching tree-level matrix elements with interleaved showers, J. High Energy Phys. 1203 (2012) 019, http://dx.doi.org/10.1007/JHEP03(2012)019, arXiv:1109.4829.

[124] Git repository for Madgraph inputs with *t*-channel exchange of colored scalar mediator, couplings to light quarks only, https://github.com/LHC-DMWG/model-repository/tree/master/models/Monojet_tChannel/contributed_by_PapucciVichiZurek, [Online; accessed 08-May-2019] (2015). http://dx.doi.org/10.5281/zenodo.3260943.

[125] Git repository for Madgraph inputs with *t*-channel exchange of colored scalar mediator, couplings to all quark generations, https://github.com/LHC-DMWG/model-repository/tree/master/models/Monojet_tChannel/contributed_by_Amelia_Brennan, [Online; accessed 08-May-2019] (2015). http://dx.doi.org/10.5281/zenodo.3260943.

[126] Git repository for Madgraph input cards for model with *s*-channel exchange of vector mediator, for electroweak boson final states, https://github.com/LHC-DMWG/model-repository/tree/master/models/EW_DMV, [Online; accessed 08-May-2019] (2015). http://dx.doi.org/10.5281/zenodo.3260943.

[127] Git repository for Madgraph inputs for model with *s*-channel exchange of pseudo-scalar mediator, produced in association with top quarks, https://github.com/LHC-DMWG/model-repository/tree/master/models/HF_S+PS, [Online; accessed 08-May-2019] (2015). http://dx.doi.org/10.5281/zenodo.3260943.

[128] Git repository for Madgraph inputs for simplified model with a colored scalar mediator coupling to DM and b-quarks, https://github.com/LHC-DMWG/model-repository/tree/master/models/HF_S+PS, [Online; accessed 08-May-2019] (2015). http://dx.doi.org/10.5281/zenodo.3260943.

[129] J.M. Campbell, R.K. Ellis, F. Maltoni, S. Willenbrock, Associated production of a *Z* boson and a single heavy quark jet, Phys. Rev. D 69 (2004) 074021, http://dx.doi.org/10.1103/PhysRevD.69.074021, arXiv:hep-ph/0312024.

[130] F. Maltoni, T. McElmurry, S. Willenbrock, Inclusive production of a Higgs or *Z* boson in association with heavy quarks, Phys. Rev. D 72 (2005) 074024, http://dx.doi.org/10.1103/PhysRevD.72.074024, arXiv:hep-ph/0505014.

[131] J.M. Campbell, R.K. Ellis, F. Maltoni, S. Willenbrock, Production of a *Z* boson and two jets with one heavy-quark tag, Phys. Rev. D 73 (2006) 054007, http://dx.doi.org/10.1103/PhysRevD.77.019903, arXiv:hep-ph/0510362.

[132] CMS Collaboration, Measurement of the production cross sections for a Z boson and one or more *b* jets in *pp* collisions at $\sqrt{s} = 7$ TeV, J. High Energy Phys. 1406 (2014) 120, http://dx.doi.org/10.1007/JHEP06(2014)120, arXiv:1402.1521.

[133] CMS Collaboration, Measurement of the cross section and angular correlations for associated production of a *Z* boson with *b* hadrons in *pp* collisions at $\sqrt{s} = 7$ TeV, J. High Energy Phys. 1312 (2013) 039, http://dx.doi.org/10.1007/JHEP12(2013)039, arXiv:1310.1349.

[134] CMS Collaboration, Search for H/A decaying into Z+A/H, with Z to ll and A/H to fermion pair 2015.

[135] R. Frederix, S. Frixione, V. Hirschi, F. Maltoni, R. Pittau, et al., W and $Z/\gamma*$ boson production in association with a bottom-antibottom pair, J. High Energy Phys. 1109 (2011) 061, http://dx.doi.org/10.1007/JHEP09(2011)061, arXiv:1106.6019.

[136] M. Wiesemann, R. Frederix, S. Frixione, V. Hirschi, F. Maltoni, et al., Higgs production in association with bottom quarks, J. High Energy Phys. 1502 (2015) 132, http://dx.doi.org/10.1007/JHEP02(2015)132, arXiv:1409.5301.

[137] Git repository for Madgraph inputs for vector and scalar mediator models leading to a mono-Higgs signature, https://github.com/LHC-DMWG/model-repository/tree/master/models/EW_Higgs_all, [Online; accessed 08-May-2019] (2015) http://dx.doi.org/10.5281/zenodo.3260943.

[138] Git repository for Madgraph inputs for 2HDM model leading to a mono-Higgs signature, https://github.com/LHC-DMWG/model-repository/tree/master/models/EW_Higgs_2HDM, [Online; accessed 08-May-2019] (2015). http://dx.doi.org/10.5281/zenodo.3260943.

[139] B. Hespel, D. Lopez-Val, E. Vryonidou, Higgs pair production via gluon fusion in the Two-Higgs-Doublet Model, J. High Energy Phys. 1409 (2014) 124, http://dx.doi.org/10.1007/JHEP09(2014)124, arXiv:1407.0281.

[140] U. Baur, E.N. Glover, Higgs boson production at large transverse momentum in hadronic collisions, Nuclear Phys. B 339 (1990) 38–66, http://dx.doi.org/10.1016/0550-3213(90)90532-I.

[141] Git repository for Madgraph inputs for dimension-7 EFT models with direct DM-EW boson couplings, https://github.com/LHC-DMWG/model-repository/tree/master/models/EW_Fermion_D7/contributed_by_Renjie_Wang, [Online; accessed 08-May-2019] (2015). http://dx.doi.org/10.5281/zenodo.3260943.

[142] S. Nussinov, Technocosmology: could a technibaryon excess provide a 'natural' missing mass candidate?, Phys. Lett. B 165 (1985) 55, http://dx.doi.org/10.1016/0370-2693(85)90689-6.

[143] D.B. Kaplan, A single explanation for both the baryon and dark matter densities, Phys. Rev. Lett. 68 (1992) 741–743, http://dx.doi.org/10.1103/PhysRevLett.68.741.

[144] T. Banks, J.-F. Fortin, S. Thomas, Direct detection of dark matter electromagnetic dipole moments arXiv:1007.5515.

[145] G. Busoni, A. De Simone, J. Gramling, E. Morgante, A. Riotto, On the validity of the effective field theory for dark matter searches at the LHC, part II: Complete analysis for the *s*-channel, J. Cosmol. Astropart. Phys. 1406 (2014) 060, http://dx.doi.org/10.1088/1475-7516/2014/06/060, arXiv:1402.1275.

[146] D. Racco, A. Wulzer, F. Zwirner, Robust collider limits on heavy-mediator dark matter, J. High Energy Phys. 1505 (2015) 009, http://dx.doi.org/10.1007/JHEP05(2015)009, arXiv:1502.04701.

[147] M. Endo, Y. Yamamoto, Unitarity bounds on dark matter effective interactions at LHC, J. High Energy Phys. 1406 (2014) 126, http://dx.doi.org/10.1007/JHEP06(2014)126, arXiv:1403.6610.

[148] PDF4LHC: Recommendation for LHC cross section calculations, http://www.hep.ucl.ac.uk/pdf4lhc/, [Online; accessed 08-May-2019] 2015.

[149] J. Alwall, M. Herquet, F. Maltoni, O. Mattelaer, T. Stelzer, MadGraph 5 : Going beyond, J. High Energy Phys. 1106 (2011) 128, http://dx.doi.org/10.1007/JHEP06(2011)128, arXiv:1106.0522.

[150] T. Sjöstrand, S. Mrenna, P.Z. Skands, PYTHIA 6.4 physics and manual, J. High Energy Phys. 0605 (2006) 026, http://dx.doi.org/10.1088/1126-6708/2006/05/026, arXiv:hep-ph/0603175.

[151] M. Whalley, D. Bourilkov, R. Group, The Les Houches accord PDFs (LHAPDF) and LHAGLUE arXiv:hep-ph/0508110.

[152] M.L. Mangano, M. Moretti, F. Piccinini, M. Treccani, Matching matrix elements and shower evolution for top-quark production in hadronic collisions, J. High Energy Phys. 0701 (2007) 013, http://dx.doi.org/10.1088/1126-6708/2007/01/013, arXiv:hep-ph/0611129.

[153] V. Hirschi, R. Frederix, S. Frixione, M.V. Garzelli, F. Maltoni, et al., Automation of one-loop QCD corrections, J. High Energy Phys. 1105 (2011) 044, http://dx.doi.org/10.1007/JHEP05(2011)044, arXiv:1103.0621.

[154] Git repository for Madgraph inputs for mono-Higgs EFT models, dimension 4 and 5, https://github.com/LHC-DMWG/model-repository/tree/master/models/EW_Higgs_D4D5, [Online; accessed 08-May-2019] (2015). http://dx.doi.org/10.5281/zenodo.3260943.

[155] J. Andrea, B. Fuks, F. Maltoni, Monotops at the LHC, Phys. Rev. D 84 (2011) 074025, http://dx.doi.org/10.1103/PhysRevD.84.074025, arXiv:1106.6199.

[156] J.-L. Agram, J. Andrea, M. Buttignol, E. Conte, B. Fuks, Monotop phenomenology at the Large Hadron Collider, Phys. Rev. D 89 (2014) 014028, http://dx.doi.org/10.1103/PhysRevD.89.014028, arXiv:1311.6478.

[157] I. Boucheneb, G. Cacciapaglia, A. Deandrea, B. Fuks, Revisiting monotop production at the LHC, J. High Energy Phys. 1501 (2015) 017, http://dx.doi.org/10.1007/JHEP01(2015)017, arXiv:1407.7529.

[158] R. Allahverdi, M. Dalchenko, B. Dutta, A. Flórez, Y. Gao, T. Kamon, N. Kolev, R. Mueller, M. Segura, Distinguishing standard model extensions using monotop chirality at the LHC, J. High Energy Phys. 12 (2016) 046, http://dx.doi.org/10.1007/JHEP12(2016)046, arXiv:1507.02271.

[159] N.D. Christensen, P. de Aquino, C. Degrande, C. Duhr, B. Fuks, et al., A comprehensive approach to new physics simulations, Eur. Phys. J. C 71 (2011) 1541, http://dx.doi.org/10.1140/epjc/s10052-011-1541-5, arXiv:0906.2474.

[160] Git repository for Madgraph inputs for mono-top models, https://github.com/LHC-DMWG/model-repository/tree/master/models/HF_SingleTop, [Online; accessed 08-May-2019] (2015). http://dx.doi.org/10.5281/zenodo.3260943.

[161] A. Belyaev, G. Cacciapaglia, I.P. Ivanov, F. Rojas-Abatte, M. Thomas, Anatomy of the Inert Two Higgs Doublet Model in the light of the LHC and non-LHC Dark Matter Searches, Phys. Rev. D 97 (3) (2018) 035011, http://dx.doi.org/10.1103/PhysRevD.97.035011, arXiv:1612.00511.

[162] N.G. Deshpande, E. Ma, Pattern of symmetry breaking with two Higgs doublets, Phys. Rev. D 18 (1978) 2574, http://dx.doi.org/10.1103/PhysRevD.18.2574.

[163] R. Barbieri, L.J. Hall, V.S. Rychkov, Improved naturalness with a heavy Higgs: An alternative road to LHC physics, Phys. Rev. D 74 (2006) 015007, http://dx.doi.org/10.1103/PhysRevD.74.015007, arXiv:hep-ph/0603188.

[164] L. Lopez Honorez, E. Nezri, J.F. Oliver, M.H. Tytgat, The Inert Doublet Model: An archetype for dark matter, J. Cosmol. Astropart. Phys. 0702 (2007) 028, http://dx.doi.org/10.1088/1475-7516/2007/02/028, arXiv:hep-ph/0612275.

[165] T. Hambye, F.-S. Ling, L. Lopez Honorez, J. Rocher, Scalar Multiplet dark matter, J. High Energy Phys. 0907 (2009) 090, http://dx.doi.org/10.1007/JHEP05(2010)066, arXiv:0903.4010.

[166] L. Lopez Honorez, C.E. Yaguna, A new viable region of the Inert Doublet Model, J. Cosmol. Astropart. Phys. 1101 (2011) 002, http://dx.doi.org/10.1088/1475-7516/2011/01/002, arXiv:1011.1411.

[167] M. Gustafsson, E. Lundström, L. Bergström, J. Edsjö, Significant gamma lines from Inert Higgs Dark Matter, Phys. Rev. Lett. 99 (2007) 041301, http://dx.doi.org/10.1103/PhysRevLett.99.041301, arXiv:astro-ph/0703512.

[168] E.M. Dolle, S. Su, The Inert Dark Matter, Phys. Rev. D 80 (2009) 055012, http://dx.doi.org/10.1103/PhysRevD.80.055012, arXiv:0906.1609.

[169] P. Agrawal, E.M. Dolle, C.A. Krenke, Signals of Inert Doublet Dark Matter in neutrino telescopes, Phys. Rev. D 79 (2009) 015015, http://dx.doi.org/10.1103/PhysRevD.79.015015, arXiv:0811.1798.

[170] S. Andreas, M.H. Tytgat, Q. Swillens, Neutrinos from Inert Doublet Dark Matter, J. Cosmol. Astropart. Phys. 0904 (2009) 004, http://dx.doi.org/10.1088/1475-7516/2009/04/004, arXiv:0901.1750.

[171] E. Nezri, M.H. Tytgat, G. Vertongen, e^+ and anti-p from Inert Doublet model dark matter, J. Cosmol. Astropart. Phys. 0904 (2009) 014, http://dx.doi.org/10.1088/1475-7516/2009/04/014, arXiv:0901.2556.

[172] C. Garcia-Cely, A. Ibarra, Novel gamma-ray spectral features in the Inert Doublet Model, J. Cosmol. Astropart. Phys. 1309 (2013) 025, http://dx.doi.org/10.1088/1475-7516/2013/09/025, arXiv:1306.4681.

[173] A. Goudelis, B. Herrmann, O. Stål, Dark matter in the Inert Doublet Model after the discovery of a higgs-like boson at the LHC, J. High Energy Phys. 1309 (2013) 106, http://dx.doi.org/10.1007/JHEP09(2013)106, arXiv:1303.3010.

[174] C. Burgess, M. Pospelov, T. ter Veldhuis, The Minimal model of non-baryonic dark matter: A singlet scalar, Nuclear Phys. B 619 (2001) 709–728, http://dx.doi.org/10.1016/S0550-3213(01)00513-2, arXiv:hep-ph/0011335.

[175] S. Andreas, T. Hambye, M.H. Tytgat, WIMP dark matter, Higgs exchange and DAMA, J. Cosmol. Astropart. Phys. 0810 (2008) 034, http://dx.doi.org/10.1088/1475-7516/2008/10/034, arXiv:0808.0255.

[176] A. Arhrib, Y.-L.S. Tsai, Q. Yuan, T.-C. Yuan, An updated analysis of Inert Higgs Doublet Model in light of the recent results from LUX, PLANCK, AMS-02 and LHC, J. Cosmol. Astropart. Phys. 1406 (2014) 030, http://dx.doi.org/10.1088/1475-7516/2014/06/030, arXiv:1310.0358.

[177] E. Lundström, M. Gustafsson, J. Edsjö, The Inert Doublet Model and LEP II limits, Phys. Rev. D 79 (2009) 035013, http://dx.doi.org/10.1103/PhysRevD.79.035013, arXiv:0810.3924.

[178] Q.-H. Cao, E. Ma, G. Rajasekaran, Observing the Dark Scalar Doublet and its impact on the Standard-Model Higgs boson at colliders, Phys. Rev. D 76 (2007) 095011, http://dx.doi.org/10.1103/PhysRevD.76.095011, arXiv:0708.2939.

[179] E. Dolle, X. Miao, S. Su, B. Thomas, Dilepton signals in the Inert Doublet Model, Phys. Rev. D 81 (2010) 035003, http://dx.doi.org/10.1103/PhysRevD.81.035003, arXiv:0909.3094.

[180] X. Miao, S. Su, B. Thomas, Trilepton signals in the Inert Doublet Model, Phys. Rev. D 82 (2010) 035009, http://dx.doi.org/10.1103/PhysRevD.82.035009, arXiv:1005.0090.

[181] M. Gustafsson, S. Rydbeck, L. Lopez-Honorez, E. Lundstrom, Status of the Inert Doublet Model and the role of multileptons at the LHC, Phys. Rev. D 86 (2012) 075019, http://dx.doi.org/10.1103/PhysRevD.86.075019, arXiv:1206.6316.

[182] A. Arhrib, R. Benbrik, N. Gaur, $H \to \gamma\gamma$ in Inert Higgs Doublet Model, Phys. Rev. D 85 (2012) 095021, http://dx.doi.org/10.1103/PhysRevD.85.095021, arXiv:1201.2644.

[183] B. Swiezewska, M. Krawczyk, Diphoton rate in the inert doublet model with a 125 GeV Higgs boson, Phys. Rev. D 88 (3) (2013) 035019, http://dx.doi.org/10.1103/PhysRevD.88.035019, arXiv:1212.4100.

[184] G. Belanger, B. Dumont, A. Goudelis, B. Herrmann, S. Kraml, D. Sengupta, Dilepton constraints in the Inert Doublet Model from Run 1 of the LHC, Phys. Rev. D 91 (11) (2015) 115011, http://dx.doi.org/10.1103/PhysRevD.91.115011, arXiv:1503.07367.

[185] S. Kraml, B. Allanach, M. Mangano, H. Prosper, S. Sekmen, et al., Searches for new physics: Les Houches recommendations for the presentation of LHC results, Eur. Phys. J. C 72 (2012) 1976, http://dx.doi.org/10.1140/epjc/s10052-012-1976-3, arXiv:1203.2489.

[186] The Durham HepData project, http://hepdata.cedar.ac.uk/abouthepdata, [Online; accessed 08-May-2019] 2015.

[187] J.S. Kim, D. Schmeier, J. Tattersall, K. Rolbiecki, A framework to create customised LHC analyses within CheckMATE, Comput. Phys. Comm. 196 (2015) 535–562, http://dx.doi.org/10.1016/j.cpc.2015.06.002, arXiv:1503.01123.

[188] K. Cranmer, I. Yavin, RECAST: Extending the impact of existing analyses, J. High Energy Phys. 1104 (2011) 038, http://dx.doi.org/10.1007/JHEP04(2011)038, arXiv:1010.2506.

[189] Michele Papucci, Joshua T. Ruderman, Andreas Weiler, Natural susy endures, JHEP 09 (2012) 035, http://dx.doi.org/10.1007/JHEP09(2012)035, arXiv:1110.6926.

[190] D. Barducci, A. Belyaev, M. Buchkremer, G. Cacciapaglia, A. Deandrea, et al., Framework for model independent analyses of multiple extra quark scenarios, J. High Energy Phys. 1412 (2014) 080, http://dx.doi.org/10.1007/JHEP12(2014)080, arXiv:1405.0737.

[191] PGS: simulation of a generic high-energy physics collider detector, http://conway.physics.ucdavis.edu/research/software/pgs/pgs4-general.htm, [Online; accessed 09-May-2019] 2015.

[192] M. Baak, G. Besjes, D. Cãžte, A. Koutsman, J. Lorenz, et al., HistFitter software framework for statistical data analysis, Eur. Phys. J. C 75 (2015) 153, http://dx.doi.org/10.1140/epjc/s10052-015-3327-7, arXiv:1410.1280.

[193] INSPIRE: High-energy physics literature database, http://inspirehep.net, [Online; accessed 08-May-2019] 2015.

[194] S. Kraml, S. Kulkarni, U. Laa, A. Lessa, W. Magerl, D. Proschofsky, W. Waltenberger, SModelS: a tool for interpreting simplified-model results from the LHC and its application to supersymmetry, Eur. Phys. J. C 74 (2014) 2868, http://dx.doi.org/10.1140/epjc/s10052-014-2868-5, arXiv:1312.4175.

[195] S. Kraml, S. Kulkarni, U. Laa, A. Lessa, V. Magerl, et al., SModelS v1.0: a short user guide arXiv:1412.1745.

[196] M. Papucci, K. Sakurai, A. Weiler, L. Zeune, Fastlim: a fast LHC limit calculator, Eur. Phys. J. C 74 (2014) 3163, http://dx.doi.org/10.1140/epjc/s10052-014-3163-1, arXiv:1402.0492.